Mass-spectroscopy and modeling of capacitive coupled hydrogen plasmas

A thesis submitted for the degree of

PhilosophiæDoctor (PhD)

Cezar Gaman

School of Physical Sciences

Dublin City University

Research Supervisor: Dr. A.R. Ellingboe

External Examiner: Dr. U. Fanz

Internal Examiner: Dr. P. Swift

2011

I hereby certify that this material, which I now submit for assessment on the program of study leading to the award of PhD is entirely my own work, that I have exercised reasonable care to ensure that the work is original, and does not to the best of my knowledge breach any law of copyright, and has not been taken from the work of others save and to the extent that such work has been cited and acknowledged within the text of my work.

Signed:

(Candidate) ID No.: 54146275 Date: 18/06/2009

Abstract

This work presents the characterization of a radio-frequency, capacitively coupled, symmetric, hydrogen plasma. Both steady-state operation and the time-profile of the afterglow when RF power is terminated are investigated. Fluxes of the hydrogen ions, H^+, H_2^+, H_3^+, at the grounded electrode are measured with an energy-resolved mass spectrometer. Spatial profiles of the electron density are measured using a hairpin probe. Particle-in-cell simulations including a complex hydrogen chemistry are performed which enable direct comparison to the experiment.

In the steady-state operation, the electron density increases with both power and pressure, and the ion flux magnitudes and energy distributions are found to vary with power. The H_3^+ ion flux decreases with power and pressure, whereas the H^+ and H_2^+ ion fluxes increase with power and pressure, with approximately equal fluxes at the highest pressure/power combination of 30.0 Pa and 750V peak-to-peak. In conjunction with the PIC results, it is determined that the H_3^+ ion remains the dominant ion in the plasma for all investigated parameter space, and that the strong variation in ion flux magnitudes and energy-distributions are due to fast-ion induced chemistry occurring in the sheath at the grounded electrode. A simple theoretical model is developed in order to estimate the electron temperature at the sheath edge if the IEDFs and electron density are known.

Investigations of the afterglow include time-evolution of the H_3^+ ion energy distribution, spatio-temporal profiles of the electron density, and particle-in-cell simulations. The measured H_3^+ ion flux energy distribution persists substantially longer into the afterglow than is seen in the PIC simulations. This unusual result is explained in the hypothesis of super elastic collision of vibrationally excited hydrogen molecule with an electron resulting in energy transfer to the electron. The mechanics such super-elastic collisions are not included in the PIC simulation, and this is consistent with the discrepancy between the simulation and the experiment. Electron density measurements show a substantial increase in the density, as much as a factor of four, sharply rising immediately after the RF voltage is switched off. Small density rises, of order 10%, are seen in the simulation. An analysis showing the validity of the measurements, and two hypothesis to explain the density rise are presented. A method for determining the electron temperature time-profile in the afterglow is introduced.

Acknowledgements

I would like to show my gratitude to my supervisor Dr. A.R. Ellingboe whose encouragement, guidance and support from the initial to the final level enabled me to reach this point. His professional and human qualities and his valuable guidance has been an important factor in the development of this project. I owe my deepest gratitude to Dr. S.K. Karkari with whom I had the privilege of working during my PhD studentship. I would like to thank Prof. M.M. Turner for the fruitful discussions regarding the PIC simulation. I thank to my many of my colleagues to support me Channel, Felipe, Derek, David, Angus, Shane, Peter, Taghrid, Vladimir, Lutfi, Muhammad, Nishant, Mubarak and Gurusharan. It was a pleasure to work with Dave, Eamonn, Kevin, Neal and Fiachra. I am grateful to Tomasz and Beata for helping me in proofreading the manuscript. I am also grateful to the administrative and technical team in the School of Physical Sciences and NCPST, namely Samantha, Sarah, Sheila, Des, James, Connor and Pat.

I would also like to thank my family and friends for their continuous support. To my parents for understanding and supporting my decisions in life, to my close friends Mihaela and Catalin for being with us in the rainy days. I would like to show my gratitude to my wife Veronica for turning her life upside down in supporting me during the entire period. I could not have done this without her continuous support, encouragement and understanding. At last I would like to thank our daughter Ana Sophia for her smile making me smile.

Contents

List of Figures

1

Introduction

1.1 The basic concepts of plasma physics

Plasma is defined as a gaseous collection of neutral particles (atoms and molecules in the ground and/or excited states, photons) and charged particles (positive and/or negative ions, electrons) that exhibit collective behavior.

One important characteristics of plasma is its quasineutrality. This consists in the tendency of charged particles within plasma to maintain locally the plasma neutral from an electrostatic point of view. The quasineutrality can be expressed as: for a given volume, the number of negative charges equals the number of positive ones. Considering a a plasma consisting of singly charge ions and electrons, the quasineutrality condition can be written as:

$$n_e \approx n_i = n_0 \tag{1.1}$$

where n_e is the electron density, n_i the ion density and n_0 is called the plasma density.

When a punctiform electrostatic charge Q is brought into a plasma volume at thermodynamic equilibrium, it results in a perturbation to the local electric potential. Poisson's equation in spherical coordinates is expressed as:

$$\frac{1}{r^2}\frac{d}{dr}\left(r^2\frac{dV}{dr}\right) = \frac{e(n_e - n_i)}{\epsilon_0} \tag{1.2}$$

where $V(r)$ is the electric potential. The ions are assumed to be fixed in space and the electron movement in response to the potential follows Maxwell-Boltzmann distribution:

$$n_e(r) = n_0 e^{\frac{eV(r)}{kT_e}} \tag{1.3}$$

Expanding equation 1.3 in a Taylor series, where kT_e represents the kinetic energy ($kT_e < eV$), and neglecting the higher order terms yields:

$$n_e = n_0 \left[1 + \frac{eV}{kT_e}\right]. \tag{1.4}$$

The Poisson equation becomes:

$$\frac{d^2V}{dr^2} + \frac{2}{r}\frac{dV}{dr} = \frac{1}{\lambda_D^2}V \tag{1.5}$$

where

$$\lambda_D = \sqrt{\frac{\epsilon_0 kT_e}{e^2 n_0}} \tag{1.6}$$

has dimension of a length. By integrating equation 1.5 the shielding potential is obtained :

$$V_D(r) = V_0(r) exp\left(\frac{-r}{\lambda_D}\right) \tag{1.7}$$

where $V_0(r)$ is the potential created by the punctiform charge in vacuum. λ_D is called the Debye length and represents the natural length[1] of V_D.

In equation 1.6, it can be seen that λ_D depends only on the electrons temperature and not on the ion temperature. This is justified by the mobility difference between the two species. Because the electrons are more mobile, they react more quickly to any perturbation and by excess or deficiency a spatial charge is formed. This spatial charge shields the perturbation of the perturbative charge from the rest of the plasma. In addition, the definition of the Debye length shows that the shielding is more efficient for smaller values of the electron temperature and for higher values of plasma density.

In practice, based on equation 1.7, the Debye length defines the quasineutrality limit. Thus, if the characteristic length of a discharge is L, the plasma is quasineutral if the condition $\lambda_D << L$ is fulfilled.

---

[1] The length at which $\frac{V_0}{V_D} = e$

Another immediate result from the quasineutrality condition and equation 1.2 is that the electric field in the plasma is constant. By introducing the boundary conditions for the bulk plasma, the constant is shown to be zero.

Assuming that the ions are fixed and equally distributed in space, if an external electric field appears in the plasma, the electrons react by moving along the electric field lines. Due to this displacement, a restoration electric field appears. The electrons reverse their trajectory, but they pass the starting point because of the inertia. Thus, the electrons oscillate with a frequency depending on the restoration electric field. To determine this frequency, a uniform plasma is considered. From Poisson equation, the electric field at position x can be written as:

$$E_x = \frac{n_0 e}{\epsilon_0} x \tag{1.8}$$

where x is the displacement of the electrons. From equation 1.8, the equation of motion becomes:

$$\frac{d^2 x}{dt^2} + \frac{n_0 e^2}{\epsilon_0 m_e} x = 0 \tag{1.9}$$

Equation 1.9 is the equation of motion for a harmonic oscillator, with the oscillation frequency - called the plasma frequency - given by:

$$\omega_e = \sqrt{\frac{n_0 e^2}{\epsilon_0 m_e}} \tag{1.10}$$

In equation 1.10 it can be observed that the electron plasma frequency depends only on the plasma density. For laboratory plasmas, this frequency lies within the microwave range. The ions are too heavy to follow these oscillations, representing the center of mass of the electron-ion pair. One of the diagnostics used in this work is based on the resonance of the diagnostic system with the plasma frequency.

Consider a plasma in contact with a surface as the system presented in figure 1.1. Due to the mobility difference between electrons and ions, a positive spatial charge is created in front of the electrode. This spatial charge leads to a breaking of the plasma quasineutrality condition [1]. As a result, an electric field appears, a field which accelerates ions towards the electrodes and at the same time repels electrons from the walls. This boundary layer in which the quasineutrality condition fails is called the sheath. Thus ions will gain energy during their travel trough the sheath. In steady-state conditions, this energy gain depends on both the voltage sheath drop and the initial energy of the ions before entering the sheath.

The whole spectrum of ion energy is called the ions energy distribution function *(IEDF)* and represents an important parameter for many applications. The ion energy distribution function at the plasma boundary, contains information about the bulk plasma in addition to the sheath. One of the objectives of the present work is to study the IEDFs of a symmetric CCP discharge, as described in section 2.1.

Measurements of IEDFs are performed using electrostatic deflection analyzers [2, 3, 4, 5], retarding field analyzers [6, 7], and cylindrical mirror analyzers [8, 9]. Another method used in determining the IEDFs is the energy resolved mass-spectrometry [10], which can determine the energy spectra of different ion species. The last method is applied in the present work and is presented in section 2.2.

1.2 Symmetric Capacitive Coupled Plasmas

Capacitive coupled RF discharges are simple devices that are used in industry in fields like semiconductor and solar cell for coating/etching and in surface treatment for increasing the bio-compatibility of materials. They consist of two electrodes with a separation gap between them (Figure 1.1). The electrodes generally have circular shapes but this depends on the application requirements. One of the electrodes is most often connected to an RF power source, while the other one is grounded. One may find situations when both electrodes are connected to the RF power supply.

The capacitive coupled plasma (*CCP*) discharge can be broadly classified as symmetric, where the two electrodes have an equal area, and asymmetric, where the two electrodes have an unequal area. In many experimental systems, such as the GEC reference cell [11], the electrodes are of equal area; however, the plasma can extend beyond the area adjacent to the electrodes, and can thereby come in contact with the grounded chamber body. In this case, the resultant system can be substantially asymmetric and the degree of asymmetry is dependent on the

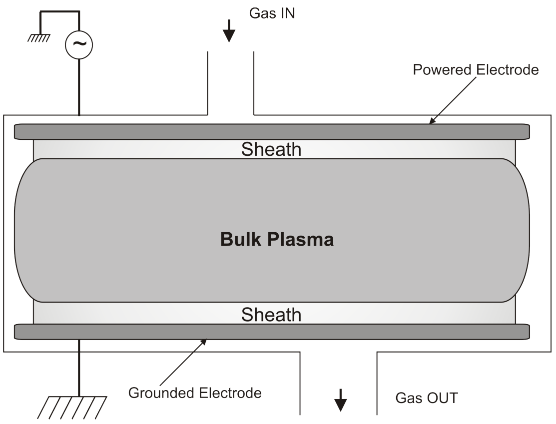

Figure 1.1: Schematic diagram of a symmetric radio frequency parallel plate capacitive coupled discharge

plasma itself. Hence, discharges with a controlled plasma volume are preferred in experiments where the plasma parameters are to be determined. The symmetry of the system eliminates the imbalance of the sheaths formed in front of the electrodes. As a result, the unknown factors are reduced.

In semiconductor manufacturing plasmas [12], the etching of dielectric materials is one example where the CCP discharges are preferred (commercial systems from Lam Research - Exelan, Tokyo Electron - SCCM, and Applied Materials - MxP and Producer - are all CCP systems, and comprise over 95% of the market). The etching usually takes place in parallel plate geometry, where the wafer to be etched is placed on one of the electrodes. When RF power is applied to one electrode, the gas within the volume between the electrodes becomes partially ionized forming a plasma. The electrons whithin the plasma are further chemically activating the gas. The flux of chemically excited gas in combination with the flux of ions striking the surface of the wafer affects the etching process. H_2 is utilized in selective etching and surface passivation [13], playing an important role in both processes.

1.3 CCP RF sheaths

Consider a system with two circular parallel plate electrodes with the diameter (D) and the separation distance (L). For $D \gg L$ the system can be approximated as an one dimensional system. This simplification can be done because the system presents a cylindrical configuration and is symmetric on the θ axis. The resolved dimension is defined with $x = 0$ at the lower side of the upper electrode (in Figure 1.1) and positive values of x towards the lower electrode. In addition, for simplification it is assumed that the plasma is formed only in the volume between electrodes by applying an RF voltage on the upper electrode in respect to the bottom one which is grounded ($V = 0$). In the middle of the discharge volume, plasma is neutral from an electrical point of view, while close to the electrodes the electrons oscillate periodically, generating positive space charge sheaths. Presuming furthermore, that the ions are fixed in space, this will lead to the approximation of constant ion density. This assumption is justified by the difference in ion/electron mobility. The electric field is zero in the bulk plasma, and therefore the electrons oscillate around a position of equilibrium. If the electrons reach one of the electrodes during the oscillation course, they will be collected leaving a positive charged space in the front of the electrode. The thickness of the spatial charge equals the amplitude of the oscillation. The time averaged potential of both powered and grounded electrodes is zero while the plasma potential is always positive. This model is also valid when the electrode material is coated with a dielectric. In this situation, the electrons become attached to the surface. Hence, in both sheaths there is an electric field which is directed towards the electrodes. This is a very important characteristic of CCP discharges for applications. In real plasma devices, ions are mobile, presenting a relatively small flow into the sheaths. In the case of collisionless discharges, the ions gain energy in the order of the sheath potential i.e. a few hundred electron volts. Noting the sheath width s, outside the sheath ($x \geq s$), the quasineutrality condition requires that $n_i \simeq n_e$. Inside the sheath, there is an imbalance of charges. From Poisson's equation 1.2, the potential in the sheath must be negative in order to repel electrons and this means that $V(x)$ must have a negative curvature. Writing the continuity equation assuming collisionless sheaths, and taking into account the plasma quasineutrality identity 1.1, results in:

$$n_i(x)v_i(x) = n_e(s)v_e(s) \equiv n_s v_s \tag{1.11}$$

Also the energy conservation can be written as:

$$\frac{1}{2}Mv_i^2(x) + eV(x) = \frac{1}{2}Mv_s^2 \tag{1.12}$$

where $0 \leq x \leq s$.

The equation for the ion density profile is found by substituting equation (1.11) into (1.12):

$$\frac{n_i(x)}{n_s} = \frac{1}{(1 - \frac{2eV(x)}{Mv_s^2})^{\frac{1}{2}}} \tag{1.13}$$

The electron density profile is found by expanding equation (1.3) in Taylor series, and neglecting the higher order terms, shows that:

$$\frac{n_e}{n_s} = 1 + \frac{eV}{kT_e} \tag{1.14}$$

By using the condition that, within the sheath, ion density is greater than the electron density, it is obtained:

$$\frac{eV}{Mv_s^2} < \frac{eV}{kT_e} \tag{1.15}$$

which can be rewritten in a more convenient form:

$$v_s > \sqrt{\frac{kT_e}{M}} \tag{1.16}$$

which is known as the Bohm criterion. This states that the ions arrive the sheath edge with a minimum speed, called the Bohm speed (v_B), speed which depends on the electron temperature and ion mass.

The question that now arises is how is it possible for ions to have such a directed speed, much greater than their thermal speed. The explanation for this is a weak electric field which extends into the plasma, weak enough to preserve the plasma quasineutrality. The spatial extent of the electric field into the plasma bulk is known in literature as the presheath.

In section 3.5, I will use these results as a hypothesis in a model for determining the electron temperature at the sheath edge. The above model assumes that the plasma is quasineutral. Including the existence of the presheath electric field, the potential at the sheath edge (for $x = s$) needs to be different from the plasma potential. In this case, the electron density at the sheath edge can be written as:

$$n_s = n_{e0} e^{\frac{e(V_p - V_s)}{kT_e}} \tag{1.17}$$

equation (1.17) can be used to estimate the sheath edge position in respect to the electrodes, assuming that the plasma potential and electron temperature are known. Based on these observations, more complex models for the RF CCP sheaths were developed by Godyak [14] and Lieberman [15].

Returning to the assumption that ions are fixed in space and therefore their density is constant in time, one can write the equation for the temporal evolution of the upper sheath width as:

$$s_U(t) = \bar{s} - \tilde{s_U} \sin \omega t \tag{1.18}$$

where $s_U(t)$ is the sheath width as a function of time, $\bar{s}$ is the time averaged sheath width and $\tilde{s_U}$ is the sheath oscillation amplitude.

From Poisson equation (1.2) and equation (1.18), the electric field across the entire discharge (in Figure 1.1 the vertical dimension) is determined:

$$E(x,t) = \begin{cases} \frac{en_i}{\epsilon_0}[x - s_U(t)], & 0 < x < s_U(t) \\ 0, & s_U(t) < x < s_B(t) \\ \frac{en_i}{\epsilon_0}[x - s_B(t)], & L - s_B(t) < x < L \end{cases} \tag{1.19}$$

The electric field needs to satisfy the continuity condition for $x = s_U(t)$ and $x = s_B(t)$. Hence, we find that $E(s_U(t), t) = 0$ and, respectively, $E(s_B(t), t) = 0$ The displacement current for the upper sheath can be presented as:

$$j_U = \epsilon_0 \frac{\partial E}{\partial t} = -n_i e \frac{\partial s_U(t)}{\partial t} = -j_{0U} \cos \omega t \tag{1.20}$$

where $j_{0U} = n_i e \tilde{s_U} \omega$. Due to the continuity condition, it is necessary for the displacement current in the sheath to be equal to the conduction current in the bulk plasma $j_p = env_B$. The same condition needs to be fulfilled on the opposite

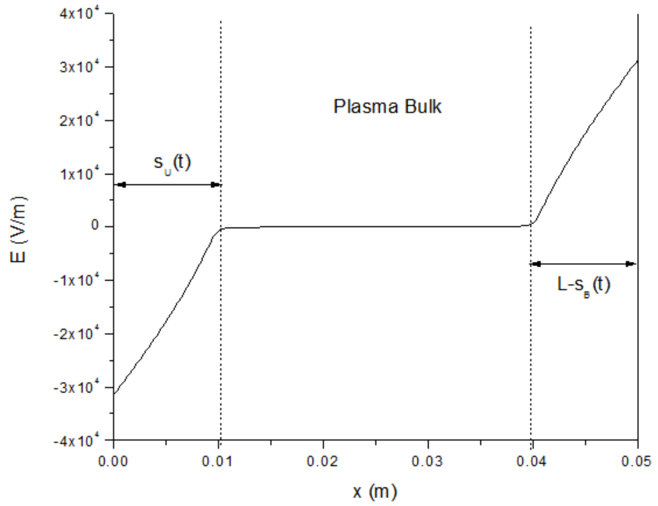

Figure 1.2: The electric field profile in a symmetric CCP discharge

side of the plasma bulk (the sheath at the lower electrode, see Figure 1.1) because of the symmetry of the system. The flux conservation leads to:

$$j_U + j_B = 0 \tag{1.21}$$

which implies that:

$$\frac{d(s_U + s_B)}{dt} = 0 \Rightarrow s_U + s_B = constant \tag{1.22}$$

From equations (1.18) and (1.22), the sheath thickness for the bottom electrode can be expressed as:

$$s_B(t) = \bar{s} + \tilde{s_B} \sin \omega t \tag{1.23}$$

The above theory is developed assuming a homogeneous ion density in the bulk plasma and electrodes sheaths. However, experiments have shown that it is not entirely true and this model is not sufficient in explaining the plasma boundary processes. More complex models are based on the same assumptions, but the electron and ion density are not considered to be uniform in either plasma or sheaths. The last condition is not essential for the plasma bulk where the quasineutrality is fulfilled, but it is crucial within the sheaths region. Lieberman [15] presents a model in which the variation of the ion density within the sheath leads to a Child law variation of the density and an increased sheath width compared to the homogeneous model.

1.4 IEDFs for hydrogen discharge

The ion energy distribution function is an important plasma parameter. It contains information about the ion energy when striking the substrate or the discharge walls. In addition, one can determine from this, the position where the ions are formed in the plasma and the collisionality of the discharge. Moreover, it is possible to determine the sheath thickness and also estimate the electron temperature at the sheath edge in particular situations, as will be shown in the next section. Knowing all of these plasma parameters helps to comprehend the phenomena involved, and they are important in plasma applications such as the semiconductor manufacturing industry or fusion plasma research.

Section two presents the CIRIS discharge where in the grounded electrode the Hiden EQP 2000 mass-resolved ion energy analyzer is mounted. In the literature, one can find numerous investigations of the IEDFs in the RF plasmas but most of them are focused on heavier atoms. Although hydrogen plasmas have been studied for many years [16, 17] and despite big interest in their application there are very few studies on this subject. A great majority of them are just theoretical ones. They are based on kinetic [18] or electric models [19, 20, 21, 22]. The kinetic models couple the two-term electron Boltzmann equation to the rate balance equation of different vibrationally and electronically excited states. The electric models combine a description of particle transport with the kinetic description of the production and destruction of particles. One immediate problem of these models is that the sheath potential is not accurately known. There are many different forms of the sheath potential used. Two of the most common ones are the Child-Langmuir potential [15] and the linear field [1].

Another problem encountered by these models is the chemical complexity of the hydrogen discharges. In these discharges, one can discover three positive ions, the hydrogen molecules and hydrogen atoms in different excited states, one species of negative ion, and electrons. Hence the chemical reactions which occur in such discharges are numerous and very difficult to model.

1.5 Hydrogen chemistry

The hydrogen molecule H_2 is the simplest known molecule. The hydrogen atom is one of the most studied atoms from the earliest stages of modern physics until today. In spite of this, the hydrogen plasma is not entirely understood and hydrogen plasma chemistry still presents open questions. Plasma contains electrically charged particles in addition to neutral atoms and molecules. The electrons gain energy and break up the molecules and ionize the gas. The electrons in plasma are frequently very hot, and the plasma is far from a thermodynamic equilibrium. All sorts of exotic reactions occur. A hydrogen plasma is typically composed of three types of positive ions (H^+, H_2^+, H_3^+), one type of negative ion (H^-), electrons, atoms, and the hydrogen molecule in a whole range of excited states. It is a challenge to keep track of all these species and predict the plasma composition. Apart from common processes such as electron atom excitation and ionization or ion atom collisions and charge transfer, a new set of chemical processes such as collisions between species of the atomic and molecular "soup" needs to be taken into consideration in case of molecular plasmas. The set of reactions that are considered important and taken into account in the simulation [23, 24] is presented in Appendix A.

In the plasma bulk, the electron collisions with the background gas produce mainly H_2^+ and electrons with low kinetic energy.

$$e + H_2 \rightarrow H_2^+ + 2e \tag{1.24}$$

The next important source of H_2^+ is:

$$H_2^+ + H_2 \rightarrow H_2^+ + H_2^+ + e \tag{1.25}$$

These ions are converted into H_3^+ through collisions with the background gas. The reaction is written [25] as:

$$H_2^+ + H_2 \rightarrow H_3^+ + H + \epsilon \tag{1.26}$$

where $\epsilon = 1.7$ eV is the resulting exothermic energy. The reaction (1.26) has a large cross-section [23, 26], which leads to an efficient conversion of the H_2^+ into H_3^+. H_3^+ ions are efficiently destroyed through collisions with the background gas at energies in excess of approximately 10 eV. Low energy H_3^+ ions only interact with the background gas through elastic collisions where the momentum-transfer cross-section dominates [27]. Therefore, in the plasma bulk, for low power density the dominant ion is H_3^+.

The H^+ ion is an ion species created mainly through secondary reactions:

$$\begin{cases} H_2^+ + H_2 \rightarrow H_2^+ + H^+ + H + e \\ H_3^+ + H_2 \rightarrow H^+ + H_2 + H_2 \\ H_3^+ + H_2 \rightarrow H_3^+ + H^+ + H + e \\ H + H_2 \rightarrow H + H^+ + H + e \\ H_2 + H_2 \rightarrow H^+ + H + e + H_2 \\ H_2 + H_2 \rightarrow H^+ + H^+ + e + e + H_2 \end{cases} \tag{1.27}$$

The direct formation of H^+ is reflected in the last two reactions from 1.27. They represent the energetic collision of background gas molecules. The cross-sections of these reactions are very small because the gas molecule has a low energy state. In this work a particle in cell *(PIC)* simulation of the experiment is presented. The simulation, which is described in section 2.4, takes into account 62 possible collision processes for all positive hydrogen ions, hydrogen molecules in different excitation states, hydrogen atoms and electrons.

1.6 Time resolved studies of afterglow discharges

Pulsed discharges are of great interest for many plasma processing applications [28, 29, 30], mainly because of their ability to control the plasma density, the mean ion energy, and the time-averaged electron temperature. In general these govern the fluxes bombarding a processing substrate. The reaction rates of complex molecular species [29] in the discharge depend on the electron energy distribution function. This function can be efficiently modified by operating the discharge in pulsed mode. In the literature, one can encounter different investigations of the plasma properties of afterglow discharge [28, 29, 30, 31]. However, their properties greatly vary with the plasma conditions used, and it is generally difficult to correlate the results from different sets of experiments. For instance, an anomalous density rise in the afterglow plasma with dust particles has been reported [28, 32]. The mechanism given to explain this results differs between the two papers, being explained in terms of associative detachment reaction involving O^- ions with the atomic oxygen. The detachment process resulted in a small fraction of energetic (fast) electrons in the plasma, which exceeded the ambipolar ion flux to the wall after a few tens of microseconds. These fast electrons charge the walls to a negative potential, almost equal to the energy of the fast electrons. As the electron temperature significantly decreases (0.1 eV) compared to the active phase, the low energy plasma electrons are better confined by the negative sheath potential at the walls created by the fast electrons in the discharge. An anomalously high sheath potential drop in the afterglow was experimentally observed as well [31]. The trapped fast electrons also caused the excitation of meta-stable atoms of the post-argon discharge [31]. In chapter four both the temporal evolution of the energy distribution function on ions reaching the grounded electrode, as well as the plasma electron density decay measured in the afterglow are shown. The experimental data is compared with results from PIC simulation.

1.7 Thesis structure

The aim of this work is the study of the symmetric RF CCP hydrogen discharge at 27.12 MHz. CCPs became a great interest for the scientific community because theirs widespread use in the industry and in research laboratories. While studies on this theme already exist, there are still open questions that need to be answered. This thesis is grouped in five chapters.

In this chapter, “Introduction”, presents the basic theories of CCPs regarding sheath dynamics and ion energy distribution functions. Also includes a brief review of the basic plasma parameters (section 1.1). The most of the fundamental theories mentioned in this thesis can be found in any introduction to plasma physics textbooks, as [1, 15, 33, 34]. Chapter one also briefly discusses the chemistry set of reactions which occur in the discharge.

In chapter two, “Experimental Setup”, the plasma source where most of the measurements take place is described. Moreover, two experimental diagnostic methods used such as measurements of ion energy distribution function with help of an energy resolved mass-spectrometer and measurements of plasma density by hairpin probe are reviewed. Whilst the aim of the thesis is not the hairpin study, a more detailed description of this method is provided. The reason for this is its novelty as a plasma diagnostic technique, hence the need for a better description and benchmarking against more well-known methods. At the end of the second chapter the results from the particle-in-cell simulation are presented. Although the author is not involved in code development, all results are original and solely based on author input. The simulation outcomes are used to validate and maximize the information obtained by experimental means.

Chapter three, “Characterization of steady-state hydrogen CCP discharge”, depicts the study of the continuous wave discharge. This chapter introduces the IEDFs as well as the chemical composition of the plasma being function of pressure and potential. The results from the experiment are compared with the simulation ones. Using the hairpin probe, the plasma density profile is determined and compared with the outcomes from the simulation. The chapter presents a small theory which relates the ion energy distribution function with the plasma density at the sheath edge and the electron temperature. This theory helps in evaluating the electron temperature (T_e) at the sheath edge when there are no direct means of measuring T_e.

Chapter four is entitled “Study of the afterglow phenomena in hydrogen CCP discharge”. Here, the measurements are focused only on a small temporal interval of the discharge pulse - the afterglow. The experimental results are compared with those from the simulation. The evolution of IEFDs and plasma density are determined in the afterglow. The results from the hairpin are surprising. Possible explanations and a discussion of the results follow. As in the continuous wave case, the temporal evolution of the electron temperature is determined.

In the last chapter the work is summarized and future work plans are discussed.

2

Experimental Setup

2.1 CIRIS - Capacitive Radiofrequency Ion Source

The great majority of measurements presented in this work are performed in a CCP RF discharge called CIRIS, which is a modified GEC cell [11]. Exceptions are the experiments presented in the subsection 2.3.4 where a benchmarck of the hairpin probe is presented. In this section the discharge chamber and the plasma diagnostics used are presented.

2.1.1 Vacuum chamber

The CIRIS chamber is shown in Figure 2.1. It consists of a cylindrical vacuum chamber with the ends fitted with reentrant elements to support the powered and grounded electrodes. The pumping system consists of two turbo-molecular pumps mounted on the bottom side of the chamber. Special attention was paid to the pumping speed and high compression ratio for the hydrogen because most of the experiments were performed using hydrogen as the background gas.

On the left hand side of the chamber (figure 2.1) there is a large diameter vacuum bellows, which is welded to the stainless steel tube and fitted with an annular flange. The powered electrode is fixed in position by insulated bolts which extend from the mounting flange to the powered electrode through an insulating

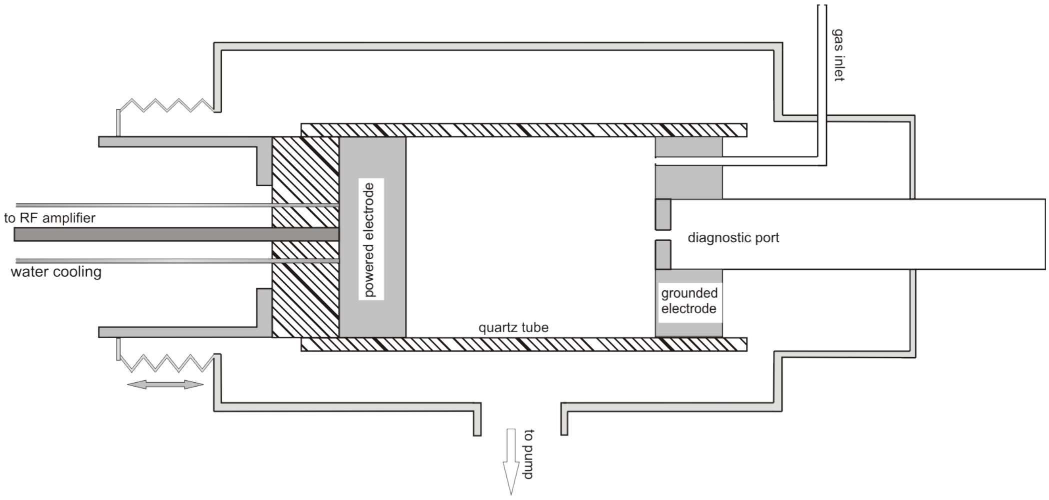

Figure 2.1: Cross-section diagram of CIRIS vacuum system

quartz disk. The diameter of both electrodes is 140 mm, and a thickness of approximately 50 mm. A water cooling is employed in the body of the powered electrode in order to prevent overheating. On the right hand side, a second re-entrant tube supports the grounded electrode. This tube is designed to allow the applied diagnostics to access the plasma. A form-fit quartz tube is concentric with the electrodes and functionally determines the radial boundary of the plasma volume (Figure 2.1).

Gas is introduced into the chamber through the grounded electrode. Small holes are drilled on the surface of this electrode, which are connected to the gas inlet. The gas exits the plasma volume through small gaps between the quartz cylinder and the electrodes, resulting in a substantial pressure difference. The area outside the quartz cylinder is connected to the vacuum pumping system via high conductance tubing. In this way, the pressure outside the quartz tube is much lower than it is inside. As a result, the plasma is formed between the electrodes when the RF voltage is applied. There is no plasma formation outside the quartz cylinder, thus resulting in a fully symmetric discharge.

2.1.2 Pressure measurement

The only port accessible to the diagnostics is the port from the center of the grounded electrode. The reason for this is the necessity of preserving the symmetry of the discharge. This makes it impossible to directly measure the pressure on the discharge chamber when a plasma diagnostic device is fitted on the diagnostic port. Before mounting any probes on the system, the pressure is calibrated using two identical pressure gauges. One is fitted on the inside of the discharge chamber through the diagnostic port, and the other one is fitted outside through an external flange. The relation between the pressure measured inside the discharge volume with that from outside is determined for a particular gas and a particular gas flow (Figure 2.2). Here, “the inside” refers to the volume delimited by the electrodes and the quartz tube, and the “outside” refers to the remaining volume of the vacuum chamber. For measuring the pressure gauges signals, a digital acquisition device DAQ with the capability of simultaneously acquiring two channels is used. Data is acquired by means of the Labview environment and then analyzed in order to determine the relationship between outside and inside pressures.

After the calibration, coefficients are determined and the plasma diagnostic device is mounted on the diagnostic port (Figure 2.1), it is possible to assess the pressure in the inside volume by measuring the pressure outside. For this, another Labview program is developed. In the program, a proportional-integral-derivative *(PID)* control function is used. The set-points are represented by the desired inside pressure values, and the measured values are those of the outside pressure. The control of these is done through the control of the gas flow delivered into the discharge volume. In Figure 2.2 the calibration curve for H_2 is presented where the gas flow is controlled using a mass flow controller with a maximum flow of 1.0 slm. The domain of interest for the inside pressure is delimited by the two horizontal blue lines, which correspond to 5.0 Pa and 30.0 Pa respectively. The relation between the two pressures is linear within this domain. The deviation from the linear fit increases for high flow values.

This method has some limitations. One of them is that the minimum pressure which can be measured depends on the initial background pressure. The pressure

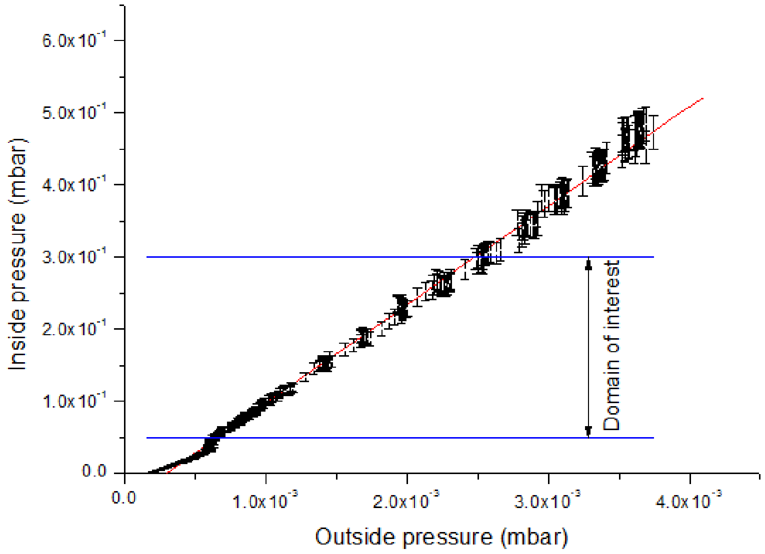

Figure 2.2: Pressure calibration for hydrogen

gauge used for these measurements consists of two complementary gauges, each one for different pressure range. The first gauge measures a pressure domain of 1000 mbar to 5x10^{-2} mbar. The second one measures pressure between 5x10^{-2} mbar to 10^{-8} mbar. This arrangement explains the small discontinuity around the 5x10^{-2} mbar of the pressure inside the discharge volume. At this point, if the gas flow increases, the gauge mounted on the diagnostic port will switch to the higher pressure range. The gauge measuring the pressure in the outside volume will continue to use the low pressure gauge, leading to a discontinuity of the calibration curve. This will also lead to a shift of the X-intercept. The calibration curve is expected to intercept the X-axis in the origin due to the fact that the gauges are identical. Figure 2.2 shows that a value of 2.89x10^{-4} mbar in the outside measured pressure will lead to 0 mbar inside the quartz tube. Another limitation of the method is caused by the fact that the deviation from linearity increases on the upper part of the pressure range.

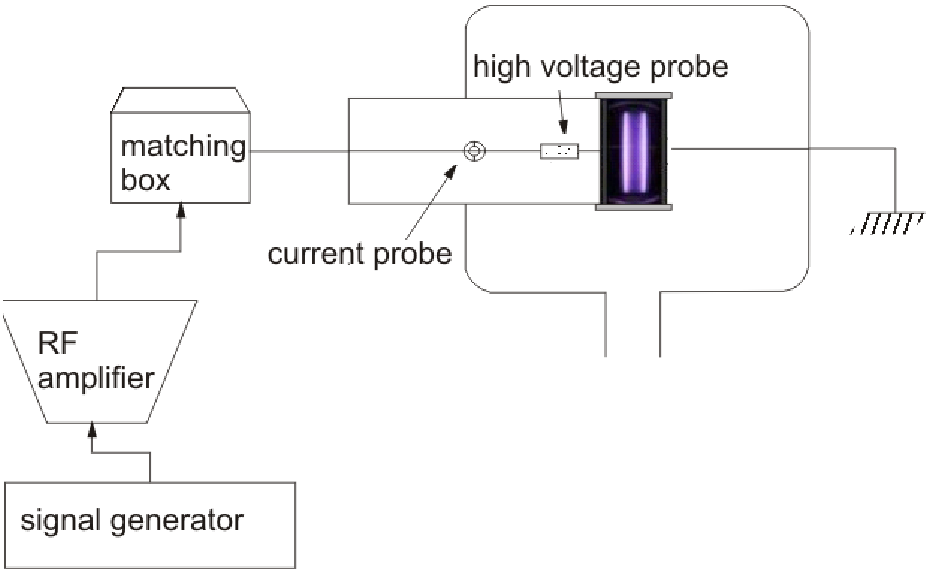

Figure 2.3: The electric diagram of CIRIS

2.1.3 Electrical circuit

CIRIS is electrically driven using an RF generator and an RF amplifier, as schematically shown in Figure 2.3. For a efficient power transfer from the 50 Ω output RF amplifier to the plasma, a Π-type matching unit is mounted close to the powered electrode. Forward and reflected powers are measured using a power meter.

The voltage on the electrode is measured using a Tektronix P6015A high voltage probe. The current is determined using a Pearson 6656 current monitor probe mounted between the matching unit and the powered electrode, as shown in Figure 2.3. Both current/voltage waveforms are captured and digitized using a Tektronix TDS oscilloscope and transferred to a PC for further analysis.

For experiments using a pulsed RF voltage a Stanford Research DG535 delay generator is used to trigger the RF amplifier. Figure 2.4 presents two typical waveforms for the continuous wave case (2.4a) and the pulsed case (2.4b).

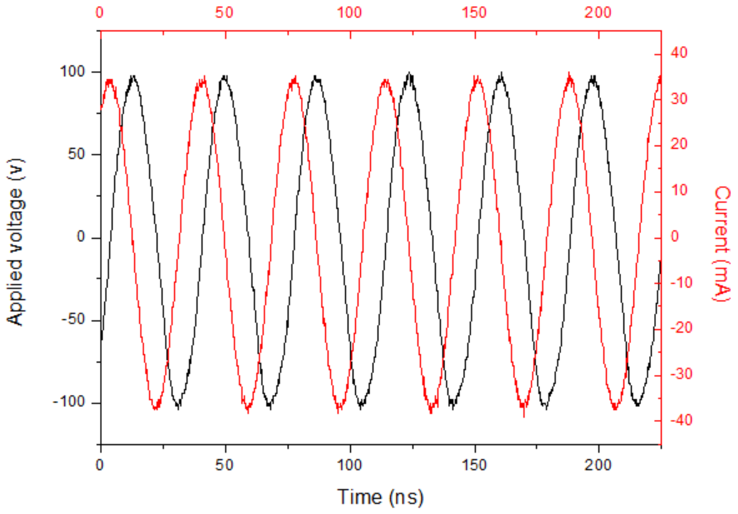

(a) The voltage (black) and current (red) waveforms in case of steady state discharge

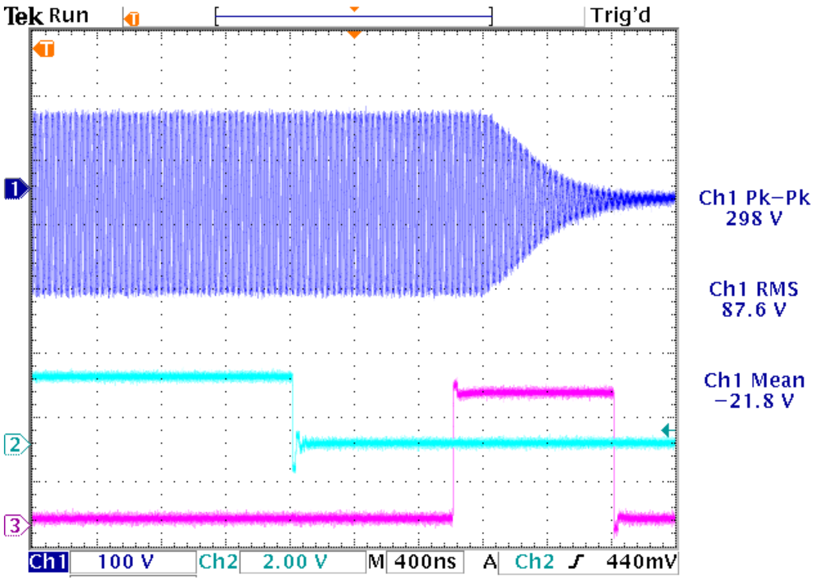

(b) The voltage waveform (1 blue), and the pulsing signal (2 light blue) in case of pulsed plasma. (3 purple) represents the gating signal applied to the mass-spectrometer detector

Figure 2.4: CW and pulsed waveforms

2.2 Mass Spectrometric measurements

Mass spectrometry is an important plasma diagnostic technique for many research and industrial applications. These include leak detection, partial pressure measurements in high vacuum systems, monitoring of the gas composition in vacuum coating processes, end point determination in plasma etching, mass-resolved determination of neutral particles and ion energy in plasma processes, determining gas specific desorption and adsorption rates of materials for vacuum system components. In spite of the considerable differences between the methods, they all have a common feature. The species being measured are required to transit large distances ($\approx$ 100 cm) without collisions, thus they need a high vacuum. One of the most common types of mass spectrometers is the quadrupole mass filter, whose qualities are: the simplicity of scanning a large mass range, high sensitivity, high measuring and repetition rate, along with compatibility with the general requirements of vacuum technology as relatively small dimensions, arbitrary mounting positions together with low out-gassing rates.

A quadrupole mass spectrometer is in principle an ionization vacuum gauge equipped with a quadrupole rods system. It separates the types of ions produced in the ionization processes according to their mass/charge ratio (m/Z), before measuring them with an ion detector. The ions are separated in a high frequency quadrupole electric field between four rod electrodes. The voltage between these electrodes consists of a high frequency alternating voltage $V \cos \omega t$ and a superimposed direct voltage U. When ions are trapped in the direction of the field axis, perpendicular to the plane of the quadrupole, they perform oscillations perpendicular to the field axis under the influence of the high frequency field. For certain combinations of U, V, and for a given ω and rod radius, only ions with a particular ratio m/Z can pass through the separating field and reach the ion detector. Ions which have a different mass to charge ratio are rejected by the quadrupole field and therefore cannot reach the detector. The m/Z ratio scanning can be achieved by varying the frequency ($m/Z \approx 1/\omega^2$). It is also possible to adjust the resolution capabilities ($\Delta m/m$) of a quadrupole mass spectrometer. This can be done by varying the ratio of the magnitude U of the direct voltage component to the amplitude V of the high frequency component. It must be

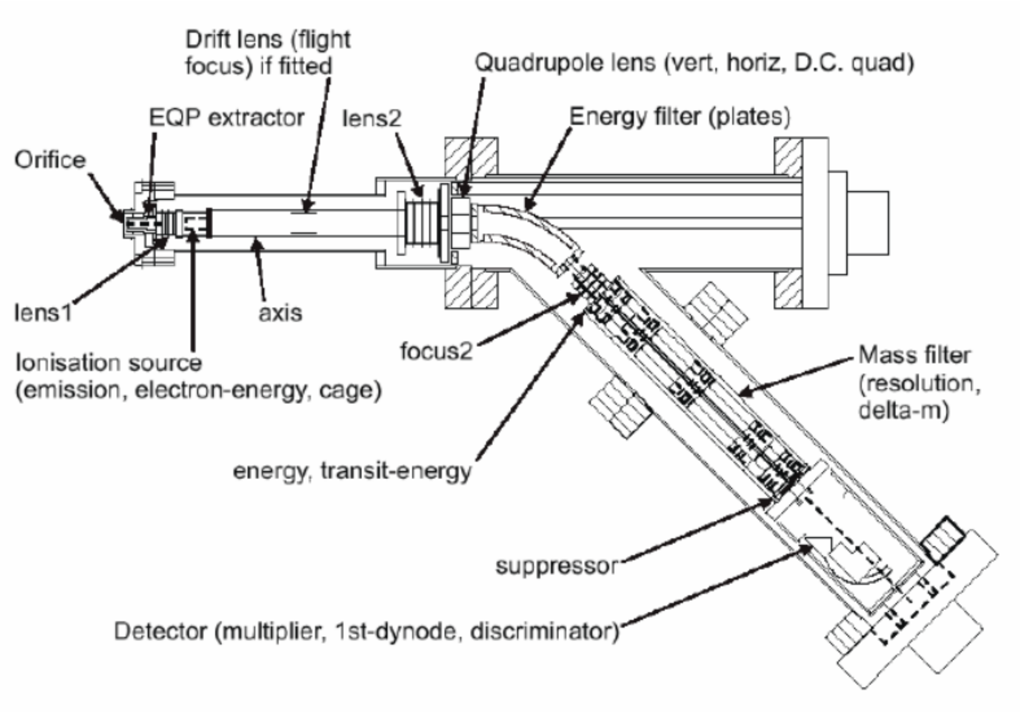

Figure 2.5: Hiden EQP diagram [35]

noted that, in practice, it is always necessary to find a compromise between best possible mass resolution and the signal magnitude.

2.2.1 The Hiden EQP energy resolved mass-spectrometer

The Hiden electrostatic quadrupole plasma (EQP) analyzer is a high-transmission 45° sector field ion energy analyzer and quadrupole mass spectrometer. It is designed as a diagnostic tool for energy resolved ion mass spectrometry analysis. It analyse the energy and mass to charge ratio distributions of ions, neutral and radicals generated in a plasma source. Moreover, it can be used in studies of transients and afterglows. Figure 2.5 presents the diagram of the Hiden EQP probe. The system includes: the EQP probe body, electrostatic analyzer (ESA) head, RF amplifier head, and mass spectrometer interface unit (MSIU) (Figure 2.6) The EQP probe comprises of the following:

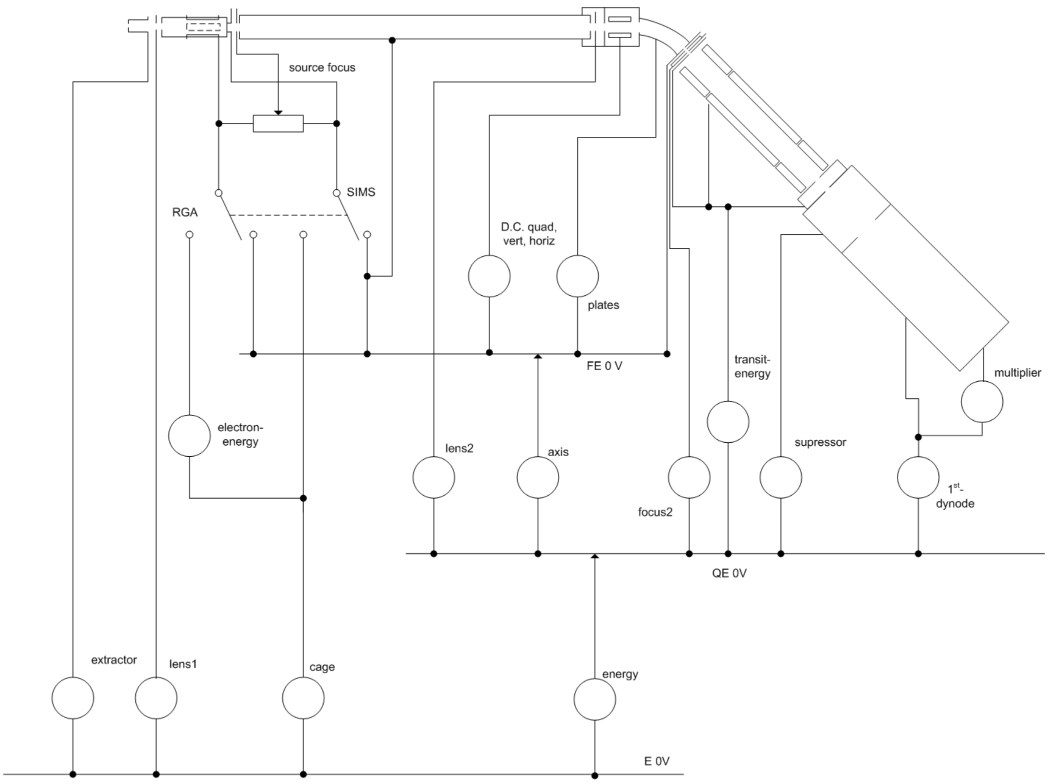

Figure 2.6: Hiden EQP mass-spectrometer electrical lenses configuration

1. an ion extraction system;
2. a filament which represents the electron-impact ion source for residual gas analyzers (RGA);
3. an electrostatic field energy analyser;
4. a triple section quadrupole for mass to charge ratio measurements;
5. an ion detector.

The ion extraction system consists of two elements. The first one is the sampling orifice. This provides a pathway for neutral species and ions within the plasma volume to enter the mass spectrometer. It is mounted on the front end and, depending on the application, the orifice can be changed in order to limit the number of particles entering the spectrometer volume. In this case, the orifice used, has 10.0 μm diameter in a 0.5 mm thick aluminum plate. The small diameter in combination with the high pump speed in the mass spectrometer results in the formation of a supersonic beam. This beam transits the extraction chamber and enters the ionization chamber. The second element of the ion extraction is an electrostatic lens - transfer lens - mounted immediately after the sampling orifice. This serves to focus the ion beam from the sampling orifice onto the exit aperture of the electron-impact source.

The ionization chamber consists of a grounded box with two filaments. When measuring the ions' spectra these filaments are turned OFF, resulting in a field free particles drift though the ionization chamber. In order to measure the spectra of neutral species, the filaments are heated to emission and biased to -70 V resulting in an energetic beam of electrons intersecting the neutral beam from the sampling chamber. This electron beam ionizes a fraction of the neutral beam. These ions are further analyzed by the mass spectrometer. It is worth noting that the time of flight within this volume depends on the initial energy of the sampled particles.

The next section of the mass-spectrometer is the drift tube, which collects the ions from the ionization chamber. It also focuses them, forming an ion beam, and transports this beam to the rest of the system. The drift tube is biased to a settable DC voltage ($AXIS$), establishing a non-ground reference voltage for the remaining components in the mass spectrometer. An ion entering the mass-spectrometer with an incident energy E_i will be accelerated to have an energy in this section given by the sum $E_i + AXIS - ENERGY$ (Figure 2.6), where $ENERGY$ is the scan energy value.

After the ions pass through the drift region, they enter the 45 degree sector field analyzer. This sector is formed by five electrodes: plates, vert, horiz, D.C. quad, and axis (Figure 2.6). Plates are the main electrodes of the energy filter, one being biased positive and the other one negative in respect to the axis. Vert, horiz, and D.C. quad are electrostatic lenses whose role is to align and focus the ion beam. The axis sets the energy of the ions which will pass the energy filter. The manufacturer recommends having this set to 40 eV for optimum operational results.

The ions which exit the 45 degree energy filter will encounter the 'focus 2' electrostatic lens which focuses and decelerates the beam to the desired energy for analysis by the quadrapole mass spectrometer. The energy within the mass filter is 3 eV and is set by the transit energy lens (see Figure 2.6). The mass filter is a quadrupole type, which comprises of a main filter driven by RF and dc, with pre- and post- filters driven solely by RF. The mass resolution is controlled by a set of lenses called delta-m and resolution. After passing through the mass filter without deflection, the remaining ion beam that has the required energy and mass to charge ratio will reach the detector. In this case, the detector is a secondary emission multiplier called *SEM*. This operates in pulse mode and its operation is controlled by three parameters: "1st-dynode" which sets the voltage on the front of the detector; "multiplier", which sets the voltage across the detector; and "discriminator" which sets the threshold of the counting pulse output from the detector. The EQP system has a second detector device that is a Faraday cup and it is recommended for lower sensitivity measurements or for the case when the secondary emission detector reaches its detection limit. The SEM detector has a limited lifetime which depends on the settings used, especially on the "multiplier" voltage. All these parameters can be controlled from the acquisition and control software produced by Hiden Analytical, on the Environmental Editor page.

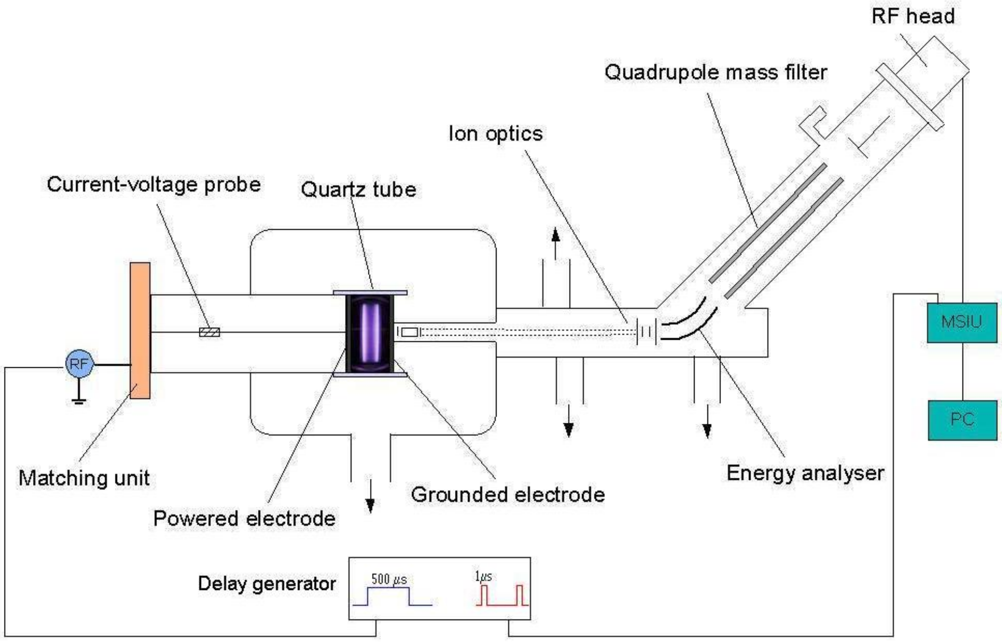

Figure 2.7: CIRIS assembly for pulse discharges

2.2.2 Use of the mass-spectrometer for afterglow studies

In order to study the afterglow process in the hydrogen CCP discharge, the experimental setup was modified as shown in Figure 2.7.

A Stanford Research delay generator is used to pulse the RF power delivered to the plasma. The pulsing frequency is 1 KHz and has a duty cycle of 50%. The SEM detector in the EQP system is also gated using the same TTL generator. The pulse is high for only $1\mu s$, and low for the rest of the 1 ms interval. In this way, the detector will only count for the $1\mu s$ time interval. If the pulse applied to the SEM detector is synchronized with the RF pulse, it can measure the ions which reach the end point only in the desired time interval. For accurate measurements, the time of flight from the moment the ions enter the sampling space to the moment they reach the SEM detector should be taken into account. After one energy scan is completed, the delay between the RF pulse and the gate window is increased by a microsecond and the process is repeated.

Collecting data in pulsed mode requires dramatically longer collecting times. In the case of continuous plasma, the total time of a scan is given by two parameters: the dwell time τ_D, which is a characteristic of the instrument, and the number of scans (n) which are required in order to provide a reliable measurement. For this experiment, the values are $\tau_D = 10^{-2}$ s and $n = 2000$ scans which leads to a total time for a single scan of $T = 20s$. In case of pulse measurements in the scan time calculation another two parameters are added. The first is the plasma power pulse period (τ_p); and the second is the gate pulse period (τ_g). If the external gating is used, one point is not completed until the sum of gating pulses equals the dwell time. In order to achieve an equivalent measurement with the continuous case, the number of measurements needs to be increased by n_d times, where n_d is given by the ration $n_d = \tau_D/\tau_g$. Subsequently the measurement time for just a single point of the scan is given by$\tau_1 = \frac{\tau_D}{\tau_g}\tau_p$, and for the total scan $T = n\tau_1$ which in this case is equal to $2 \cdot 10^4$ s. The last result shows an increase of the measurement time by three orders of magnitude. Hence it is required to determine the optimal setting for the mass-spectrometer in order to get the best and most accurate signal but also to minimize the time required for a measurement.

2.3 The Hairpin probe

The use of classical electrical probes, such as Langmuir probes, for measuring the plasma parameters in a symmetric parallel plate CCP discharge can be challenging due to the large plasma potential oscillations [36]. These oscillations can lead to an underestimation of the plasma density and an overestimation of the electron temperature. Different techniques have been implemented in order to filter [37, 38] or to compensate [38, 39] these erroneous results. In the present work is used a microwave resonator probe, called the Hairpin probe. The Hairpin is an open ended, quarter wave transmission line, whose resonance frequency depends on the dielectric of the surrounding medium.

The probe was used for the first time by Stenzel in 1976 [40], but due to its bulky design (Figure 2.8) and difficult acquiring method it was forgotten for almost thirty years. In 2004 Piejak recalled and improved this technique [41]. Also in 2004, following a visit by Piejak, the Plasma Research Laboratory (*PRL*) group in Dublin [42, 43] started to investigate this probe. A new design and also a new method of acquisition were developed. The new design improves the signal to noise ratio by a better coupling of the microwave signal. The new time resolved technique increases data reliability and reduces the measurement time. The main advantage of utilizing this probe in diagnostics of CCP discharges is given by its high impedance to the ground. This allows the probe to follow the plasma potential oscillations. However, the probe has a number of limitations when compared with other similar diagnostic techniques. One important limitation is that this probe only measures the plasma density, whereas the Langmuir probe can also determine other plasma parameters such as the electron temperature or the electron energy distribution. In this section, is presented the basic hairpin theory and construction, along with two experimental benchmarks performed in two different plasma sources.

2.3.1 Hairpin Probe theory

Consider a transmission line - a U-shaped parallel wire, open at one end, immersed in a uniform medium with a homogeneous dielectric constant. The modulus of the wave vector is given by:

$$k = \frac{\omega}{c}\epsilon^{\frac{1}{2}} \tag{2.1}$$

For a quarter-wavelength one open end resonator $kl = \frac{\pi}{2}$, the resonance frequency is given by:

$$\omega_r = \frac{\pi}{2l}c\epsilon^{-1/2} \tag{2.2}$$

where l is the resonator length, c the light of speed in vacuum and ϵ the dielectric constant of the medium. Following the theoretical development proposed by [40], consider the dielectric medium to be a non-magnetized plasma with the dielectric constant:

$$\epsilon = 1 - \frac{\omega_p^2}{\omega^2} \tag{2.3}$$

Substituting (2.3) into (2.2) and rearranging it the following formula is obtained:

$$\omega_r^2 \left(1 - \frac{\omega_p^2}{\omega^2}\right) = \omega_{r0}^2 \tag{2.4}$$

where $\omega_{r0}^2 \equiv \frac{\pi c}{2l}$ is the vacuum resonance. Substituting (2.3) into (2.2) and rearranging it can be written:

$$\omega_r^2 = \omega_{r0}^2 + \omega_p^2 \tag{2.5}$$

where $\omega_p \equiv \sqrt{\frac{n_e e^2}{\epsilon_0 m_e}}$ is the plasma characteristic frequency (equation 1.10). From the relative shift of the resonance frequency in vacuum compared with that in plasma, the electron density can be determined:

$$n_e = \frac{\epsilon_0 m_e}{e^2}\left(\omega_r^2 - \omega_{r0}^2\right) \tag{2.6}$$

Rewriting (2.6) in more practical units, this become:

$$n_e[10^{10}cm^{-3}] = \frac{\nu_r^2 - \nu_{r0}^2[GHz]}{0.81} \tag{2.7}$$

The density determined in (2.6) represents an averaged value of the electron density over the volume penetrated by the probe's electric field. As the geometric configuration of this is given by two parallel lines, the electric field will be concentrated mainly in the space between these lines, while the spatial resolution of the measured density is given by the probe's dimensions. To determine the relation (2.6), the assumption of unmagnetized plasma is made. However, the algorithm

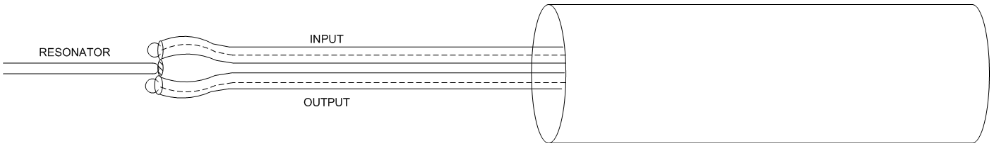

Figure 2.8: The diagram of the first microwave probe, as shown in [40]

is still valid in the case of weakly magnetized plasmas. The plasma dispersion relation can be written as [1]:

$$\epsilon = \left(1 - \frac{\omega_p^2}{\omega^2} \cdot \frac{\omega^2 - \omega_p^2}{\omega^2 - \left(\omega_p^2 + \omega_c^2\right)}\right) \tag{2.8}$$

where ω_c is the electron cyclotron frequency (see Appendix B). In the case of weakly magnetized plasma, the electron cyclotron is much smaller than the plasma frequency $\omega_c << \omega_p$, and the equation (2.8) can be reduced to equation 2.3. In addition another simplification hypothesis was introduced using (2.3), which is true only in case of collisionless plasmas. This hypothesis will limit the working range of our probe. In the collisional case, the dielectric constant will have an additional imaginary term given by the electron-neutral collisions, $\epsilon = 1 - \frac{\omega_p^2}{\omega(\omega - j\nu_n)}$ which will lead to a correction factor for the electron density measurements.

2.3.2 Probe construction

The Stenzel's [40] hairpin probe design (Figure 2.8) was a transmission probe which comprises of an 8.0 mm long resonator. This is mounted between two high temperature coaxial transmission lines on an insulated bridge. The excitation wave is sent to the upper one (*INPUT*), which couples to the resonator. The magnitude of oscillation in the resonator is detected by the other line (*OUTPUT*). The two main advantages of this probe design are: a good coupling of the signal and the high quality factor (Q=150) of the resonator. One of the drawbacks of this probe is the actual size of the probe assembly. While this was not significant in Stenzel's experiment [40] with a large volume (0.6 m^3) and high plasma homogeneity, it might become a problem in systems with a significant

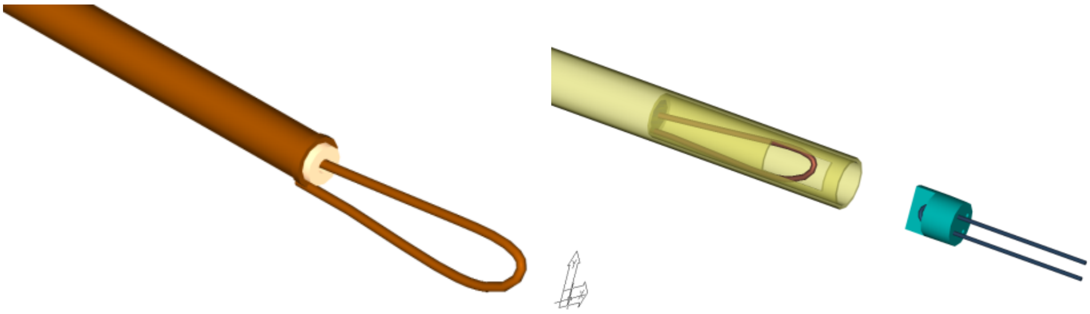

(a) the hairpin coaxial loop antenna **(b)** the hairpin resonator

Figure 2.9: Hairpin probe design

structure in the plasma density profile. Because many plasma systems are much smaller, for example CIRIS which has a volume of only 7.6x10^{-4} m^3, this probe can be perturbative. In addition, the fact that it requires two transmission lines, one for sending the signal to the probe and one for reading the signal back, can be inconvenient and can create many difficulties. Piejak modified this design [41, 44] by directly coupling the resonator to the input loop. In this way, the insulated bridge is eliminated and, as a result, the probe size is reduced. The reduced size leads to a smaller perturbation of the plasma. Furthermore, the signal coupling is improved by this method because of the elimination of the dielectric bridge.

The probe used in here is a reflectance type probe built in-house by the PRL group, [42, 43] and is shown in Figure 2.9. The microwave signal from the HP5086 microwave sweep oscillator is sent to the loop through a broadband directional coupler, as illustrated in Figure 2.10. The resonator is 20.0 mm long, with a separation distance between the prongs of 2.0 mm. The wave propagates along the coaxial cable to the coupling loop, as presented in Figure 2.9a. The coupling loop presents a non-50 Ω termination to the transmission line; This termination results in a substantial reflection. The reflected wave is selected by the directional coupler and converted to a DC voltage using a microwave Zener diode. The frequency of the microwave generator is swept and the corresponding DC voltage voltage is collected as a function of the input frequency. When the drive frequency equals the resonant frequency of the hairpin the circulating current in the hairpin increases, resulting in a power dissipation proportional with I^2R. Hence, the

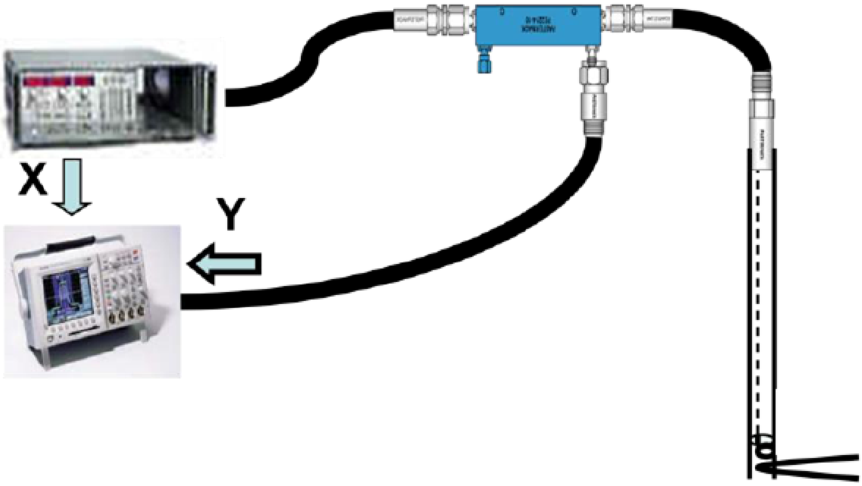

Figure 2.10: Schematic diagram of the electrical circuit of the Hairpin probe

measured reflectance current decreases in magnitude.

Th 20.0 mm long probe will resonate in vacuum at approximately 4.0 GHz and will have a quality factor $Q \approx 100$. Since our microwave oscillator is limited to a maximum frequency of 8.0 GHz, the electron density which can be measured is restricted to a maximum of 7.5x10^{11} cm^{-3}.

Figure 2.11 presents the resonance chart constructed as described above for two situations. The black line is the vacuum resonance curve and the red one represents the case when a polytetrafluoroethylene (PTFE) sheet introduced between the hairpin prongs. Because the dielectric constant of the PTFE sheet is greater than the dielectric constant of vacuum, the resonance frequency shifts to lower frequencies. If the second medium is a plasma, the dielectric constant is smaller than the vacuum dielectric constant, thus the resonance frequency for plasma is greater than in vacuum. Equation (2.7), can be used to determine the electron density from the difference between the two frequencies.

In the case of pulsed plasmas, the electron density varies faster than the sweep period, and a different method is used [42] which is described herein. The experimental setup is the same as for previous case, the only difference is that the oscilloscope is synchronized with the RF pulse. The microwave source is set to

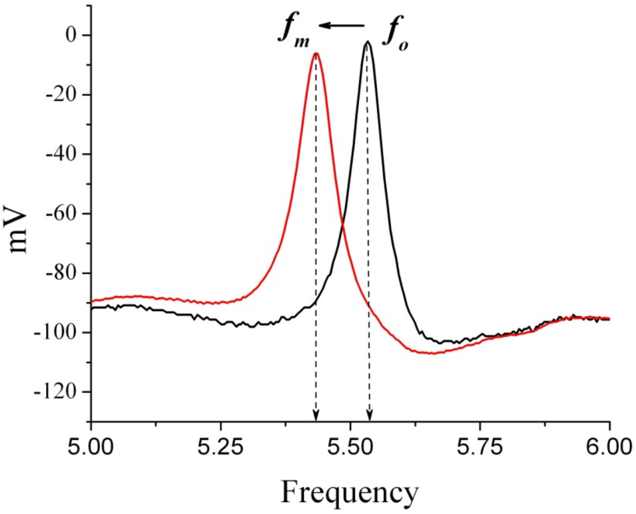

Figure 2.11: The resonance peak shift. f_0 is the vacuum frequency and f_m is the resonance frequency with the hairpin immersed in a dielectric medium, in this case PTFE.

a frequency, and the probe signal (proportional to the power reflected from the probe) is measured versus the period within the pulse. The microwave source is stepped through the desired frequency span in successive pulses. If, during the plasma pulse, the microwave frequency is in resonance with the plasma loaded hairpin, the reflected power from the probe will drop and the probe signal magnitude will get smaller. Variation of the time resolution is achived by selecting the acquisition time base on the oscilloscope. The minimum time interval between two points is given by the oscilloscope acquisition limit. In this experimental setup, the limit is 2.0 ns. However the time resolution of the hairpin is defined by its quality factor Q. For Q values of approximately 100 and a working frequency of 4.0 GHz, the bandwidth of the resonance curve will be 40.0 MHz, which corresponds to a time of 25.0 ns. Being aware of the fact that a shift in the resonance is not detectable if the shift is less then 5% of the semi-bandwidth, a following conclusion is drawn: a plasma density variation produced in less than 2.0 ns cannot be detected. On the other hand, it will take 25.0 ns for the peak to rise to

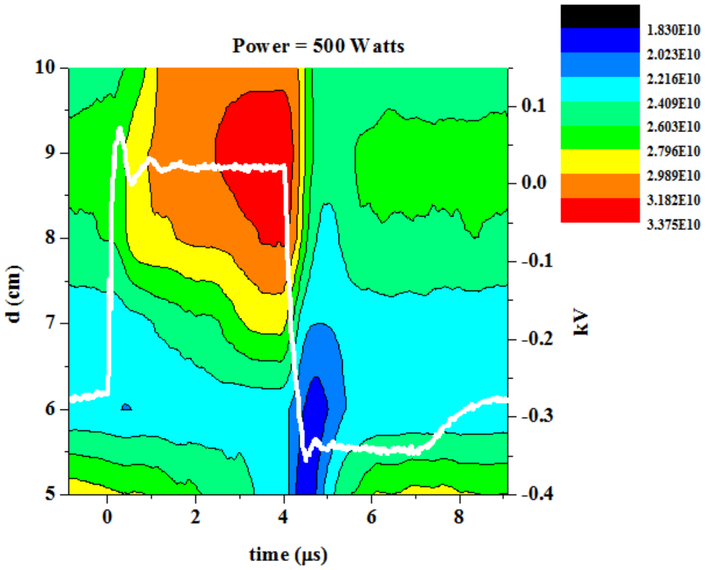

Figure 2.12: The spatial and temporal evolution of electron density

$1/e$ of the height at the non-resonant conditions.

This method has been applied to a pulsed magnetron plasma device which has been described in detail in [45, 46]. Individual data sets are collected for a selection of microwave frequencies whose range typically spans from below to above the hairpin resonance frequency at the lowest plasma density to the highest density. The time evolution of the electron density is determined by applying the normalization procedure of the plasma waveform to the vacuum waveform and detecting the resonance frequency. Figure 2.12 presents the evolution of electron density in time and space in case of a magnetron discharge [43], where the x axis represents the time in microseconds, the left y axis represents the distance from the probe to the magnetron and the electron density is represented by the colors. The white waveform shows the applied voltage evolution, and its amplitude is visible on the right hand side y axis.

2.3.3 Sheath correction theory for a hairpin probe

When a wire such as a hairpin resonator probe is immersed in plasma, a sheath will be formed around the wire, [15] as illustrated in Figure 2.13. The sheath

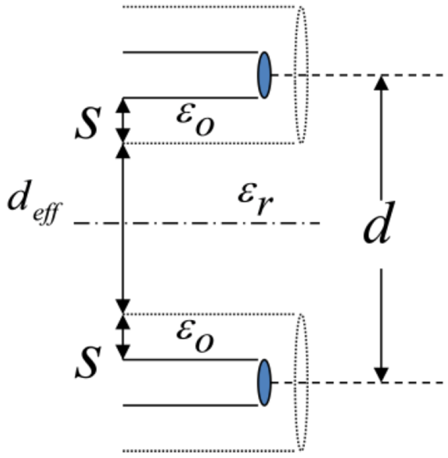

Figure 2.13: The hairpin and the effective distance between the hairpin prongs

contains no electrons, and so its permittivity is equal to the vacuum permittivity. This will lead to a higher measured value of the dielectric constant and therefore to an underestimation of the electron density. In order to take into account such sheaths developed around the hairpin prongs, it is necessary to calculate the sheaths width, and a model [41] is required to determine the complex permittivity of the three media: sheath - plasma - sheath. For calculating the sheath thickness a step-front sheath model is recommended [41] due to the fact that a floating probe is used, and the potential difference between such a probe and the plasma is very small. Use of the Child-Langmuir sheath theory will over-estimate the sheath thickness. A infinitely long hairpin with the radius of the wire a and the separation between the two prongs $2h$ is considered. In the ideal case (no sheath), the capacitance per unit length between one of the prongs and half plane is given by:

$$C_h = \frac{K\epsilon_{eff}}{\ln\left(\frac{2h}{a}\right)} \tag{2.9}$$

where ϵ_{eff} is the effective permittivity and K is a constant which depends on the units desired for C_h units. Taking into account the sheaths formed around the wires, the total capacitance is calculated as two capacitors are connected in series. One is the sheath capacitance with the inner radius a and outer radius b

- the sheath radius. The second capacitor is represented by the plasma and this has the inner radius, the sheath edge b and the outer one the medial plane h:

$$C_{total} = \frac{K\epsilon}{\ln\left(\frac{2h}{b}\right) + \epsilon \ln\left(\frac{b}{a}\right)} \tag{2.10}$$

From this the plasma frequency corrected for the presence of the sheath may be expressed as:

$$\nu_p^2 = \frac{\nu_r^2 - \nu_0^2}{1 - \left(\frac{\nu_0}{\nu_r}\right)^2 \Lambda} \tag{2.11}$$

where $\Lambda = \frac{\ln(b/a)}{\ln(2h/a)}$

The sheath correction is found useful for low electron density plasmas, where the contribution of the sheath capacitance can be comparable as order of magnitude with that from plasma. One method to avoid this problem is to increase the separation between the prongs but this will lead to two side effects. The first one will be an increase of the plasma perturbation and the second one a decrease of the coupling signal.

2.3.4 Comparison with the Langmuir probe

Another benchmark of the hairpin probe has been performed using a standardized diagnostic [47]. This is done by using a Langmuir probe developed by the IPP Augsburg [48]. The probe (APS3), is an RF passive compensated design. The probe results were previously calibrated using a microwave interferometer. The experiments are performed in a cylindrical ICP experimental chamber presented in more detail in [47, 48]. The chamber has four flanges at right angles to each other, and two additional ports at the top and the bottom of the cylindrical chamber (with diameter $\Phi = 15.0cm$). Pumping is done from one of the side ports. Plasma is produced by an inductive coil antenna at the top port, which is insulated by quartz plate and Faraday shield to limit the capacitive RF field penetrating the plasma. The coil is powered by an 27.12 MHz RF generator with a tunable matchbox. The RF power is ramped up to 350 W and the pressure varied in the range of 6.0 - 30.0 Pa. Simultaneous measurements from the two ports were collected. The Langmuir probe is mounted on the bottom port on the

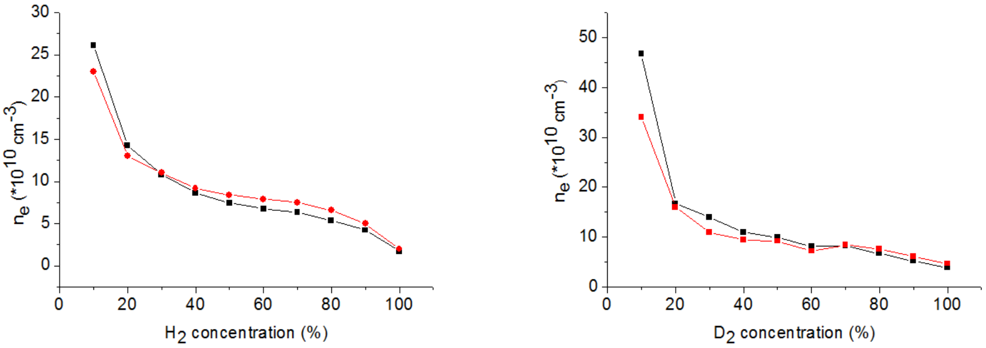

(a) H_2 Ar mixture **(b)** D_2 Ar mixture

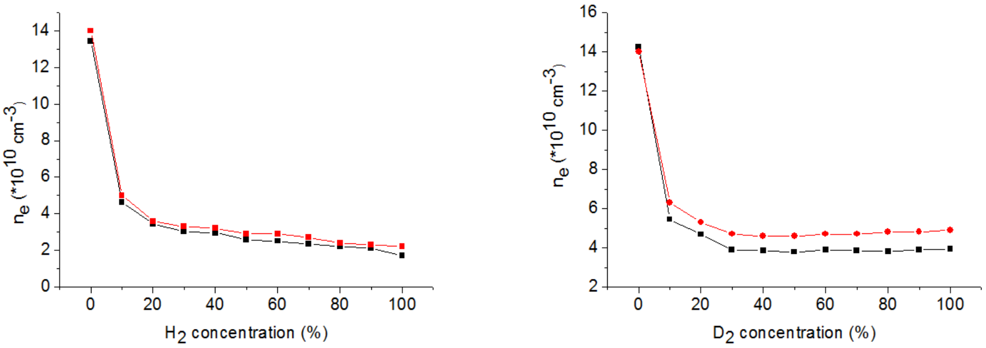

(c) H_2 He mixture **(d)** D_2 He mixture

Figure 2.14: The electron density measured by Hairpin (black) and Langmuir probe (red)

cylinder axis, while the hairpin is mounted on the perpendicular axis at one of the side diagnostic ports. Both probe tips are 1.0 cm away from the center of the plasma chamber. Figure 2.14 presents a comparison of the electron density measurements taken simultaneously with a hairpin - black symbols, and a Langmuir probe - red symbols. The X-axis represents the concentration variation of H_2 (2.14a,2.14c) respectively D_2 (2.14b,2.14d) in mixture with Ar (2.14a, 2.14b) and He (2.14c,2.14d). It can be seen that the results obtained by both probes are in good agreement.

The effect of an external magnetic field on the hairpin probe is studied. A set of permanent magnets is placed at each of the opposing flanges, with the same orientation in such a way that the external magnetic is perpendicular to the symmetry axis of the plasma chamber. The magnetic field at the center of the plasma could be varied from 1.92 mTesla to 8.2 mTesla by varying the number of magnets used. Figure 2.15 shows the measurements of plasma density in the presence (2.15c, 2.15d) and absence (2.15a,2.15b) of the external magnetic field. The gas used is helium at 10.0 and 15.0 Pa and argon at 5.0 and 10.0 Pa. The input power varies from 180 to 250 W for helium and from 30 to 120 W for argon. Again, both probes are in good agreement, except for the case of helium and no magnetic field where the hairpin probe overestimates the electron density for all input power values. Figure 2.15 shows that the hairpin measurements present some scattered deviations from the general trend. These errors are introduced by the signal to noise ratio and the automated resonance peak identification method used.

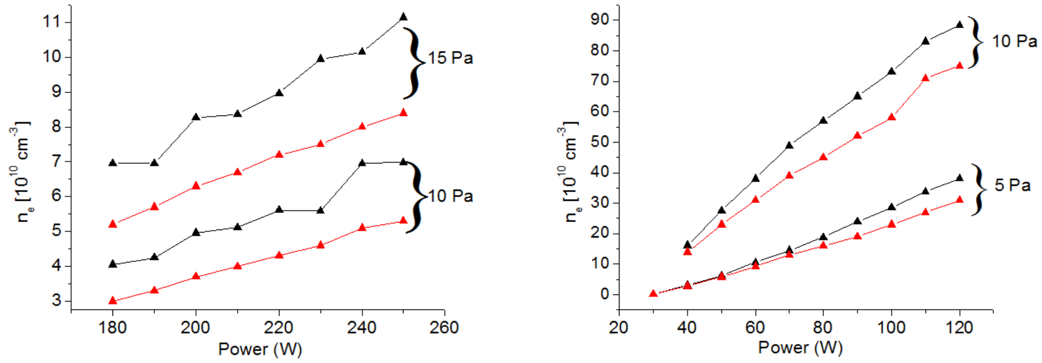

(a) Helium, no magnetic field **(b)** Argon, no magnetic field

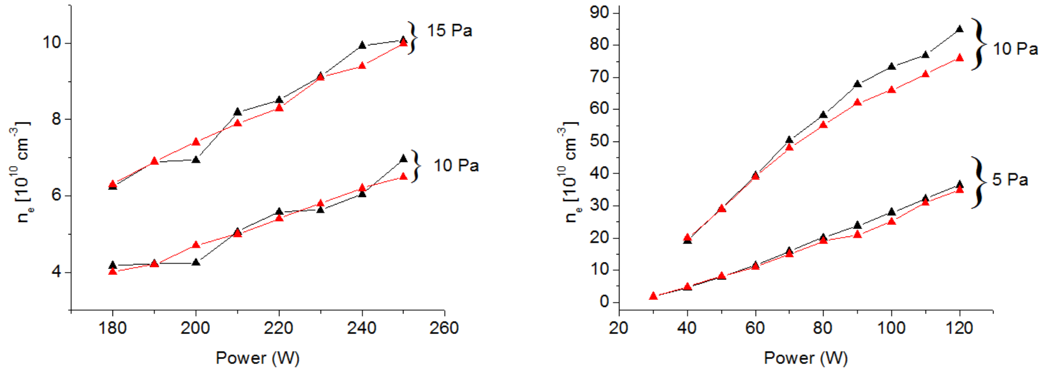

(c) Helium B=1.92 mTesla **(d)** Argon, B=1.92 mTesla

Figure 2.15: Variation of electron density measured by Hairpin (black) and Langmuir probe (red) as function of power, with and without magnetic field for He (left column) and Ar(right column)

2.4 PIC simulation

Particle-In-Cell (PIC) simulations of CCP discharges provide accurate information of plasma properties as particles energy distributions function without requiring assumptions about the electric field or about the velocity distributions of the simulated species.

The plasma volume is divided into discrete positions called cells. The position and velocities of particles are calculated by solving the motion and field equation for a particular moment in time. By repeating the calculation through successive time-steps, the solution “relaxes” to the fully self-consistent solution of particle densities, particle velocities, and fields. In this way the full kinetic behavior of the particles are retained, making PIC simulations particularly useful in obtaining information in the case of non-linear, inhomogeneous or anisotropic plasmas.[49, 50].

In practice PIC codes are classified depending on the number of dimensions, the number of velocity components used to describe the particles, and the field-equations that are solved (e.g. the code solving the entire Maxwell equation set is called electromagnetic code whilst the code solving only the Poisson equation is called electrostatic code.)

The simulation code used in this work is the “en” (written by Prof M.M Turner, [51]). The code is a *1d3v* - one dimensional displacement with three velocity dimensions. It is a modified version of “xes” code written by the Berkeley plasma theory and simulation group [52, 53]. It simulates a one dimensional plasma-sheath-bounded system in a symmetric parallel plate capacitive discharge.

The code uses a “Leap-Frog” technique to interleave the field and motion solvers. An initial condition is assumed, such that the particle positions $\vec{r_i}(t)$ at $t = 0$, and the particle velocities $\vec{v_i}(t)$ at $t = -1/2$ *time-step* are known. From the full set of particle positions at time-step t, the Poisson equation is solved to give the spatial profile of the electric field, $\vec{E}(\vec{r}, t)$ at the grid-points

$$\nabla^2\Phi(t) = \frac{e}{\epsilon_0}\sum(n_i(r(\vec{t})) - n_e(r(\vec{t}))) \tag{2.12}$$

where the summation is over the ion and electron species, n_i and n_e respectively. Updated particle velocities are calculated from the previous known velocities and the electric field

$$\vec{v}_i(t + 1/2) = \vec{v}_i(t - 1/2) + \frac{q}{m}\vec{E}_t(\vec{r_i})\Delta t \tag{2.13}$$

The particle positions for time-step $t + 1$ are calculated using Newtons equation of motion from the positions at t and velocities at $t + 1/2$. External forcing functions, such as the varying electrode voltages are included as boundary conditions (surface charge) when solving the Poisson equation (Equation 2.12). By iteratively progressing the solutions to Equations 2.12,2.13 using the "leap-frog" technique, the spatial profiles of the plasma solution are carried forward in time until the system reaches steady-state.

Plasma simulations are found to converge to a single solution independent of the chosen initial conditions if a set of criterion are met. The first criterion is that the time-step, Δt, must be smaller that the shortest period of interest, which is the plasma period $\frac{2\pi}{\omega_{pe}}$. The second criterion is that the grid-size must be large enough such that individual particles do not transit more than one cell per time-step, $\Delta x \geq v_{fast}/\ \Delta t$ (preventing "action at a distance" phenomena) and small enough to resolve the smallest feature such as the sheath associated with Debye shielding, $\Delta x < \lambda_D$. The third criterion is that the number of particles per cell is sufficiently large that the statistical variation is small, $\frac{n_0}{\Delta x^3}$ is large.

For most low-temperature plasmas, Δt and Δx are the limiting criterion, and the minimum number of particles per cell is far exceeded. In addition, the number of charged particles is very large ($10^{14} - 10^{21}\ m^{-3}$), and it is practically impossible to simulate such a large number of particles do to the computational time required to follow so many particles and to sum each particles contribution when solving Poisson's equation. The solution is to simulate *superparticles* which each represent a large number, N, of physical particles, often 10^3 or more. The *superparticles* are defined as:

$$\begin{array}{l} m^* = \sum_N m_i \\ q^* = \sum_N q_i \end{array} \tag{2.14}$$

where m^* and q^* are the *superparticles* mass and charge, respectively. (Where multiple ion species are followed a *superparticle* for each species is defined, and the multiplier N may be different for each species.) Noting that in the equation of motion particles react to the field dependent on the ratio of charge to mass (q/m_i) the *superparticles* respond in the same way as the constituent particles would, hence the *superparticle* has the same trajectory as the real plasma particle.

Collisions between particles are treated individually and are considered to be instantaneous and discrete in time. They are introduced in the simulation by the Monte Carlo Collision technique (MCC) which determines if and what type of collision occurs. Collision probabilities are based on cross-sections of the individual collisions from experimental and/or theoretical analysis, or by analogy with known cross-sections. The set of collisions and their respective cross-sections are listed in the Appendix A.

The drawback of such simulation technique in comparison with fluid or global models is the computational time. Considering a larger number of particles in the interaction, the computational power demand will increase considerably. Because the collisionless and collisional motions are treated independently it is possible to calculate the positions separately from the velocities computations. Hence if the simulated space presents symmetric proprieties (i.e. cylindric geometry), it is possible to reduce the number of coordinated used for computing the particles positions while allowing the velocities to evolve in full three dimensional space. This technique is used for reducing the computational time

The input files are created in such a way that the model investigates the same experimental conditions as those used in the CIRIS experiment. Hence the pressure varies from 5.0 Pa to 30.0 Pa and the peak-to-peak voltage from 100V to 750V. This helps to make a direct comparison of results for validating the measurements and code. The code can be used to determine characteristics of the plasma that are outside the operating regime of the system and/or to experimental results that are not obtainable by the diagnostic suite on the experimental system.

To simulate the hydrogen plasma chemistry, the analyzed species include two neutral particles: hydrogen atom H, and molecule H_2 ; four charged particles: electrons and the positive hydrogen ions H^+,H_2^+ and H_3^+. Also in the collision chemistry set processes involving the internal energy states of H^*, H_2^* are taken into account. The result is a set of 62 reactions between the above mentioned particles. These reactions are elastic collision, rotational and vibrational excitation, dissociative excitation, ionization, charge exchange collision, dissociative ionization, momentum transfer and electron capture. The chart of the reactions used in the simulation can be found in Appendix A. Diagnostics of plasma parameters are performed at every 2.3x10^{-7} s. The parameters determined are spatial profiles of the electric field, the potential, the displacement current and the flux as well as density of each particle species. The mean energy density, the power deposition within the plasma the thermal energy density and the collisions rates also belong to this group. The last set of diagnostics performed are the drift velocity, Debye length, the energy distribution function within plasma together with the energy distribution of particles arriving at the surface of the electrodes.

3

Characterization of steady state hydrogen CCP discharge

Section 3.1 presents the basic features of the IEDF and their mathematical interpretation. Section 3.2 presents the measured IEDFs versus pressure (5.0 - 30.0 Pa) and applied voltage (100 - 750 V_{pp}). In section 3.3 the PIC simulation results for direct comparison to results from section 3.2, giving insights into the interpretation of the experimental results, in particular to the formation pathways for the different hydrogen ion species are presented. In section 3.4 the experimental measurements of electron density using the floating hairpin probe are presented. Section 3.5 presents a novel technique for determining the electron temperature at the sheath edge, taking into account the ion energy distribution function and the electron density at the sheath edge.

3.1 Energy resolved mass spectrometry

An energy resolved mass spectrometer is mounted onto the grounded electrode to measure the ion and neutral fluxes arriving at this boundary (see Section 2.2.1).

Special caution is taken to preserve the symmetry of the discharge. This reduces the number of phenomena which can occur in the discharge and simplifies the model needed to simulate the system, since both electrodes can be considered

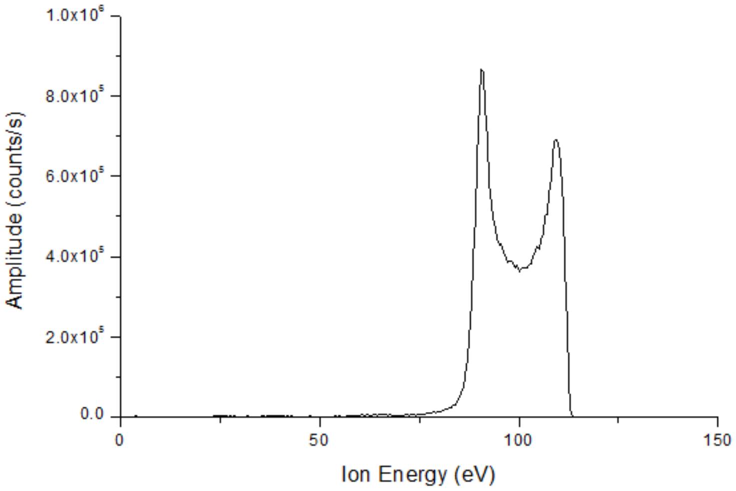

Figure 3.1: Typical IEDF for H_3^+ in CCP discharge

identical from the electrical point of view. However, in the experiment a small negative bias is developed on the powered electrode (approximately 10% of V_{pp}). The presence of the small dc bias leads to the conclusion that the charge collection area is slightly increased at the grounded electrode.

Figure 3.1 illustrates a typical IEDF of H_3^+ obtained in a hydrogen discharge at 27.12 MHz, with the ion energy in electron volts (eV) is on the ordinate, and the number of ions counted at the ion detector is on the abscissa. The number of counted ions is proportional to the flux of ions reaching the electrode. The proportionality factor is a function which depends on the sampling orifice area and the instrument multiplication factor.

Assuming that the sheath in the front of the electrode is collisionless, the potential variation is governed by the Child-Langmuir law, and one can write:

$$V_s(x) = \frac{3}{2}\sqrt[3]{\frac{3M\bar{J}_i^{\,2}}{4e\epsilon_0^2}}\,x^{4/3} \tag{3.1}$$

where $V_s(x)$ is the sheath potential as a function of position, $\bar{J}_i$ is the ion current density measured at x=0 (at the boundary) and M is the ion mass [54]. In the case of an ion transiting from the plasma through the sheath to the boundary the energy balance can be written as:

$$\frac{1}{2}Mv_x^2 = e\left(\bar{V_s} - V(x)\right) \tag{3.2}$$

Writing the energy balance equation, the ion velocity throughout the sheath thickness can be determined [15]. The ion transit time is found by integrating over space and neglecting the initial ion velocity:

$$\tau_{ion} = 3\bar{s}\left(\frac{M}{2e\bar{V_s}}\right)^{1/2} \tag{3.3}$$

where $\bar{s}$ and $\bar{V_s}$ are the averaged sheath thickness and voltage. Normalizing the ion transit time by the RF period τ_{RF} results in:

$$r = \frac{\tau_{ion}}{\tau_{RF}} = \frac{3\bar{s}\omega}{2\pi}\left(\frac{M}{2e\bar{V_s}}\right)^{1/2} \tag{3.4}$$

If $r >> 1$, then the ions will take many RF cycles to cross the sheath region. In this case they will not respond to the instantaneous sheath voltage. Their final energy at the boundary will depend on the averaged sheath voltage and will be independent of the RF phase in which ions enter the sheath.

When r<<1, which is equivalent to $\tau_{ion} << \tau_{RF}$, ions cross the sheath in a small portion of an RF oscillation. Hence the phase of the RF voltage at which they are entering the sheath is very important. As the ions are accelerated/decelerated during a small fraction of the RF period, their kinetic energy will be strongly affected by the instantaneous sheath field. An ion entering the sheath when the sheath voltage is low will gain a small amount of energy from the sheath electric field. Conversely an ion entering the sheath when the sheath voltage is large will gain a large amount of energy from the sheath electric field. Assuming a sinusoidal nature to the sheath potential and time-independent ion flux into the sheath, more ions will enter the sheath during periods of very low and very high voltage than for intermediate values when the sheath voltage is changing most quickly in time. Hence the ion energy will have the shape of a saddle, with the separation between the higher and lower peaks (Figure 3.1) equal to the sheath voltage drop and centered on the mean sheath voltage.

Considering that an IEDF is determined as described for the case r<<1, the averaged sheath voltage can be expressed as $\bar{V_s} = \frac{V_1+V_2}{2}$, where V_1 and V_2 are the minimum and the maximum sheath voltage drops. The energy separation between the peaks, ΔE_i, is expressed as:

$$\Delta E_i = e(V_2 - V_1) \tag{3.5}$$

Calculating the ion energy distribution assuming a collisionless RF sheath, Benoit-Cattin [54] found that the energy peaks separation can be expressed in the following way:

$$\Delta E_i = \frac{4e\bar{V_s}}{\pi}\frac{1}{r} \tag{3.6}$$

Equation (3.6) shows that the broadening of the IEDF is inversely proportional to the ratio of ion transit time to RF period. If the frequency of the applied RF voltage increases, the ions do not respond to the instantaneous voltage, and as result, the broadening of the IEDF reduces. Therefore, taking into account equation (3.3) the broadening of the energy peaks is inversely proportional with the ion mass. Hence for the same experimental condition, the greatest broadening effect is expected to take place in the case of hydrogen discharges. Another conclusion drawn from equation (3.6) is that separation of the peaks is proportional to the RF input power. The last two results are valid only if the model assumptions are met, namely: the sheath is collisionless and the initial velocity of ions entering the sheath is negligible compared with the velocity that they will gain from the sheath electric field. However, the Bohm criterion requires the ions enter the sheath region with at least Bohm speed. This leads to the conclusion that if there are no collisions or if the collisions are only elastic - ion flux conservation - then by measuring the IEDF at the grounded electrode, the plasma properties at the sheath edge can be determined.

The integral of the IEDF from Figure 3.1 for all energy values will be proportional to the total ion flux reaching the electrode, the proportionality factor depending on the sampling orifice area, and the multiplication factor of the detector. If these factors are known or determined by experimental means, measuring the IEDF leads to determination of the ion flux at the sheath edge.

Nevertheless, this theory restricts the number of plasma discharges where it can be applied. One restriction limiting the validity of this theory is the hypothesis that there is only one singly-charged ion species with kinetic energy at the sheath edge which is negligible in respect to the kinetic energy gained in the sheath. In the case of multiple ions plasmas, the contributions of each individual species to the total ion flux need to be determined. Another restriction is the absence of ionization in the sheath region. For capacitive coupled hydrogen discharges, at least three ion species are present in the sheath. Hence it is necessary to characterize the ion energy spectra for each ion species to be certain that the theory for determining the electron temperature at the sheath edge is applicable to this case.

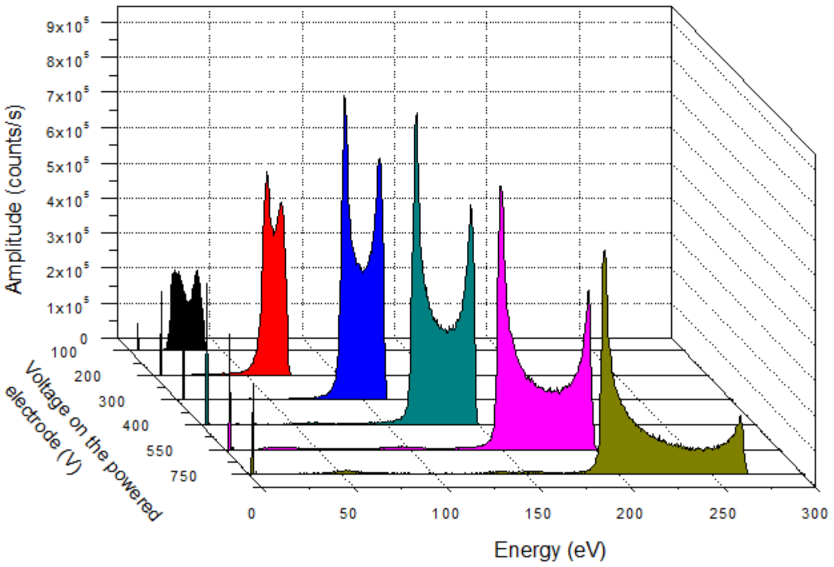

Figure 3.2: Measured IEDFs of H_3^+ for hydrogen pressure of 5.0 Pa and different peak-to-peak RF voltages

3.2 Characterization of hydrogen CCP discharge

The energy resolved mass-spectrometer mounted into the grounded electrode is used to evaluate the energy spectra for all positive ions of the hydrogen discharge for a large number of experimental conditions covering pressure range from 5.0 to 30.0 Pa, and RF voltage from 100 to 750 V peak to peak. In addition, the "en" PIC code is used to simulate the same experimental conditions in order to improve the understanding of the phenomena which occur in the sheaths.

Figure 3.2 shows the IEDF of the H_3^+ ion for six different values of the discharge applied voltage (100 V, 200 V, 300 V, 400 V, 550 V, and 750 V), with 5.0 Pa background gas pressure. As can be seen in Figure 3.2, the IEDFs present a saddle shape in each case, and the central point of the structure shows an increase in energy with increases in the applied voltage. At peak-to-peak voltage $V_{pp} = 750V$ the peak ion energy is 270 V. The lower ion energy is at 180 V. Looking across different voltages the maximum ion energy scales as approximately $0.75 \cdot V_{pp}/2$ and ΔE scales approximately with V_{pp}. One will expect the maxi-

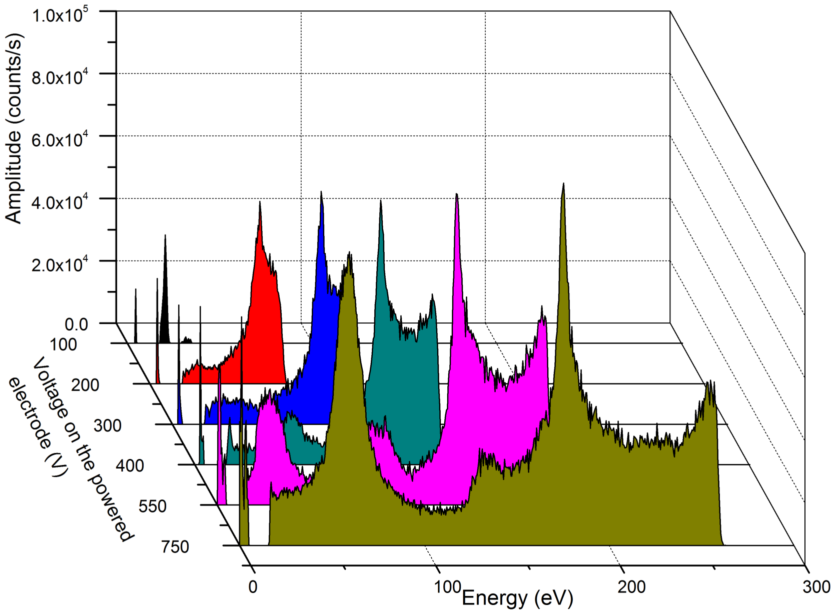

Figure 3.3: Measured IEDFs of H_3^+ for a background pressure of 15.0 Pa and different applied RF voltages

mum energy gained by the ions to be $V_{pp}/2$. The lower energy values measured can be explained taking into account the 10% DC offset in the input voltage RF waveform, presented in subsection 2.1.3. In addition the method used for measuring the applied voltage does not give the actual value on the electrode surface but at 20 cm away from it, due to the inductance of the line from the measurement point to the front of the electrode facing the plasma. Therefore the voltage probe can overestimate the input RF voltage.

Figure 3.3 persents the IEDFs of H_3^+ ion for the same input voltages as those in Figure 3.2 but for the 15.0 Pa case. With the increase in the pressure, the IEDFs below the low energy peak in the saddle structure become more complex. New peaks are seen at low energies, which indicates that a part of the ion flux is formed within the sheath. One explanation of this phenomenon is the decrease of the mean free path with an increase in pressure, thus creating an increase in collisions within the sheath.

Figure 3.4, presents the H_2^+ IEDFs measured at 5.0 Pa. The H_2^+ ions are produced in the bulk plasma by electron impact ionization.

$$e + H_2 = H_2^+ + e + e \tag{3.7}$$

However, as described in section 1.5, the H_2^+ ion is quickly converted into H_3^+. The small but finite ion flux of H_2^+ at the full sheath voltage (270 V for V_{pp} = 750 V) is consistent with this description. H_2^+ can also be formed by energetic ion chemistry in the sheath via:

$$\vec{H_2^+} + H_2 \to H_2^+ + H_2^+ + e \tag{3.8}$$

Similarly:

$$\vec{H_3^+} + H_2 \to H_2^+ + H_2^+ + H + e \tag{3.9}$$

In equations 3.8 and 3.9 the vector symbol represents an energetic ion. The newly formed “cold” H_2^+ ion has a high probability of converting into H_3^+ via a collision with molecular H_2. However, once accelerated by the field, an energetic H_2^+ ion is much less likely to be converted into H_3^+ as this cross-section scales with $1/\nu_{ion}$. Comparing Figures 3.3 at 15.0 Pa and 3.4 at 5.0 Pa, it can be noticed that there is a peak in H_2^+ at 50-70 eV below the primary H_3^+ peak (for example from the saddle structure), and a concurrent secondary H_3^+ peak due to conversion of the H_2^+ “cold” ion into H_3^+. The main source of H_3^+ ions [23] is H_2^+ association (see equation 1.26). This also represents a loss source for H_2^+ ions.

Figure 3.4 illustrates the IEDFs of the H_2^+ ion reaching the grounded plate for the experimental conditions, pressure 5.0 Pa and applied voltage from 100V to 750V. This can be directly compared to H_3^+ data in Figure 3.2 The presence of a small flux of H_2^+ at the same maximum energy as seen in the H_3^+ spectra demonstrates that some of the flux originates in the bulk plasma and experiences the full sheath voltage. However, the majority of the ions in the sheath suffer collisions which will determine changes in the final energy distribution. Figure 3.5 illustrate the IEDFs spectra of H_2^+ for the same voltages as in the previous case and 15.0 Pa pressure. As the pressure increases, the high energy tail is reduced, with most of the existing ions being cooled down by charge exchange collisions with neutrals or new ions are produced as a result of dissociation:

$$H_3^+ + H_2 \to H_2 + H + H_2^+ \tag{3.10}$$

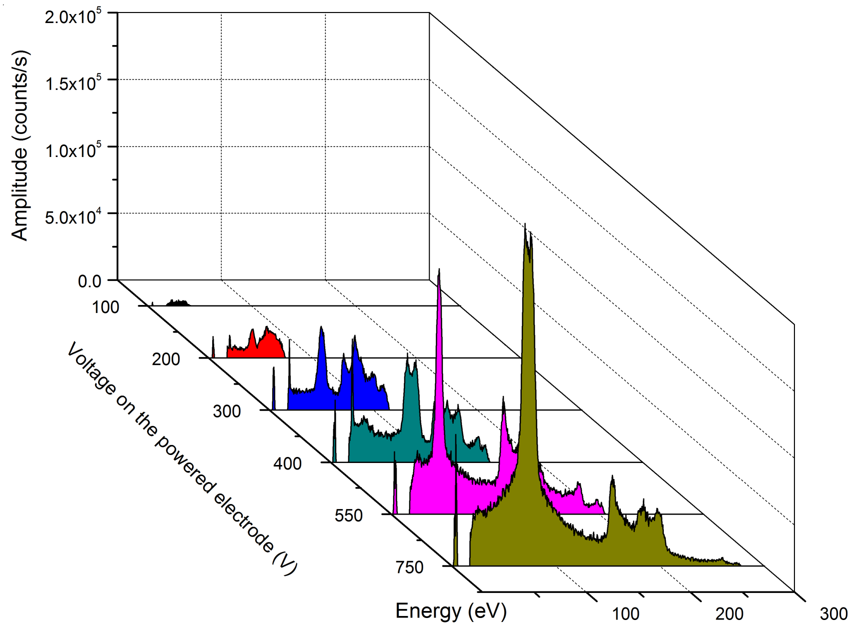

Figure 3.4: Measured IEDFs of H_2^+ for a background pressure of 5.0 Pa and different applied RF voltages

The chemistry of the H^+ ion is even more complex. In Figure 3.6, one can see the energy distribution of H^+ ion in the experimental conditions: pressure 5.0 Pa and RF voltage 100V - 750V. The average energy of H^+ ions is less than the sheath voltage, which shows that they are not accelerated in the full sheath width but formed inside the sheath. The number of peaks that such energy distribution presents corresponds to the number of RF cycles necessary for the ions to cross the sheath and reach the sampling orifice mounted on the electrode surface. In Figure 3.7 it is shown that the population of H^+ is almost non-existent in case of low applied voltages in comparison with the other two species of hydrogen ions. Simulated results which will presented in the next section shows that for H^+ the energetic chemistry is driven in the sheath space.

For a given operation condition (RF voltage and pressure), integrating the IEDFs over energy gives the total ion flux for that species. Summing over the species gives the total ion flux for that operating condition. In Figure 3.8 the relative ion fluxes for 5.0 Pa discharge are plotted as a function of the RF voltage.

In the experimental case

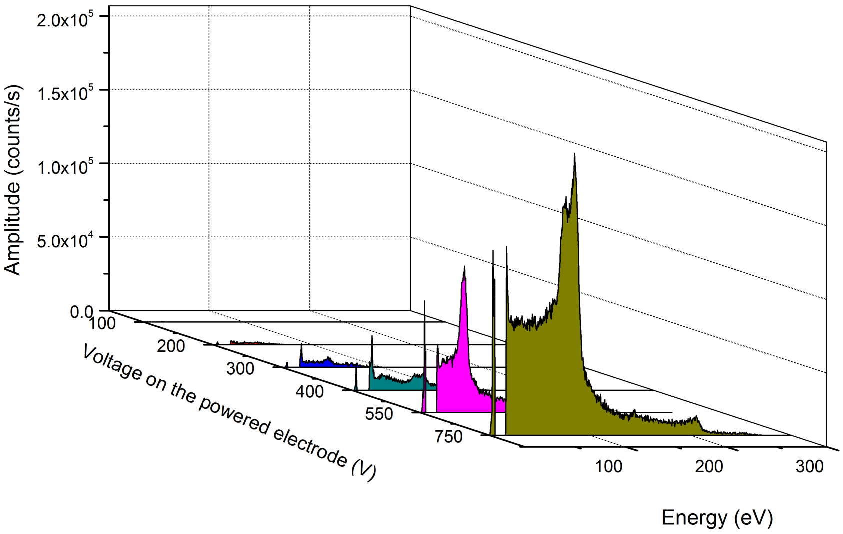

Figure 3.5: Measured IEDFs of H_2^+ for a background pressure of 15 Pa and different applied RF voltages

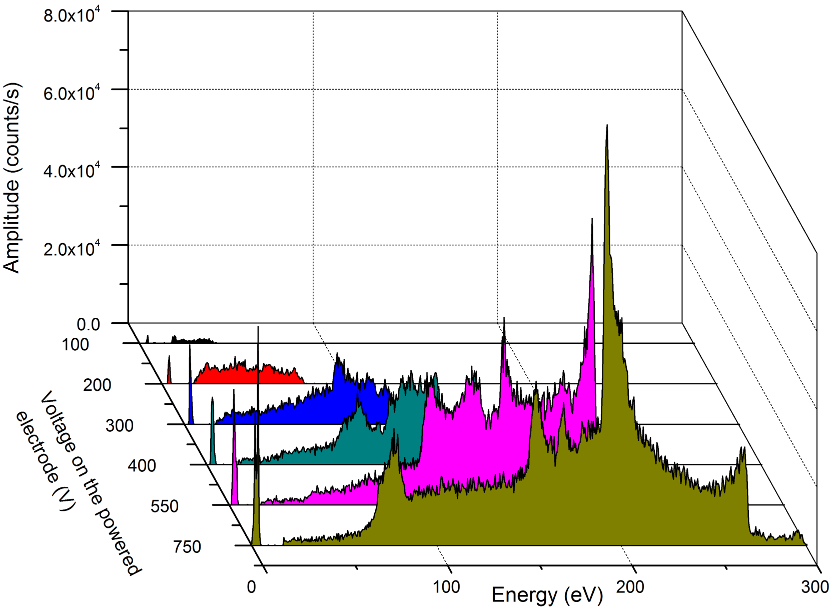

Figure 3.6: Measured IEDFs of H^+ for a background pressure of 5 Pa and different applied RF voltages

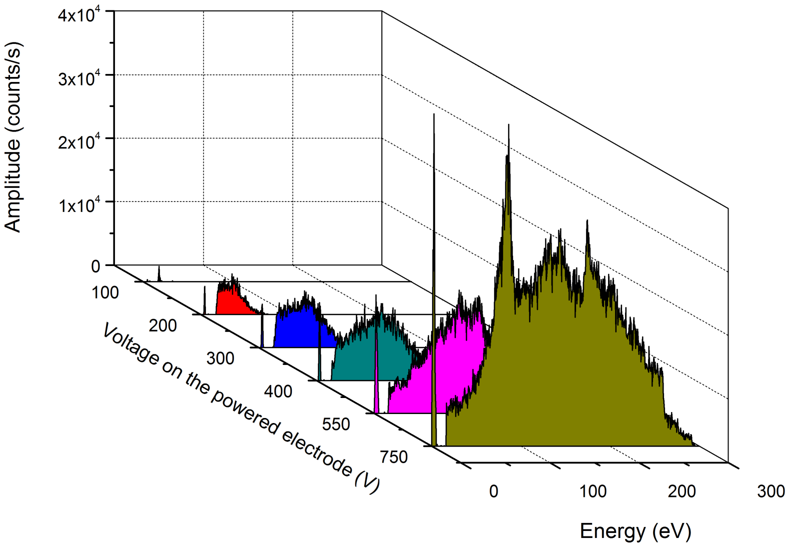

Figure 3.7: Measured IEDFs of H^+ for a background pressure of 15 Pa and different applied RF voltages

One of the first conclusions from this graph is that the H_3^+ is the most dominant ion species for all values of the applied voltage. It can be observed that, with the increase of the input voltage, the number of H_3^+ reaching the electrode is considerably decreasing; in contrast, the H_2^+ and H^+ populations rise and particularly H_2^+ which tends to become the most dominant ion species. This behavior has two possible explanations: the first is a reduction in the probability of H_2^+ association. This means that fewer H_3^+ ions are produced and the loss of H_2^+ is also reduced. This reaction has a cross-section with a maximum for low energies. By increasing the energy of particles, the probability of such reaction occurring reduces. Another reason for decrease in the H_3^+ population is the growth of H_3^+ collisions. This is possible because the sheath width increases with the voltage increase, and thus the probability of a collision with an energetic H_3^+ ion increases. If an H_3^+ ion with the energy greater than 10 eV undergoes a collision, it will dissociate, (3.10), producing a slow H_2^+ ion. This explains why the H_3^+ ion flux reduces whilst the H_2^+ flux increases. The same behavior is observed for higher pressure. In figures 3.9a and 3.9b the relative ion fluxes for all three positive

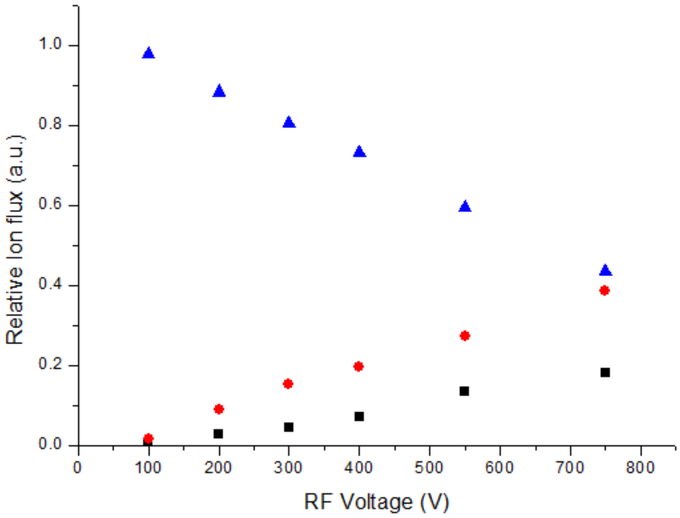

Figure 3.8: The relative ion flux as a function of RF applied voltage and background gas pressure of 5.0 Pa. The black squares represent the H^+ ions, the red discs H_2^+ and the blue triangles H_3^+ ions.

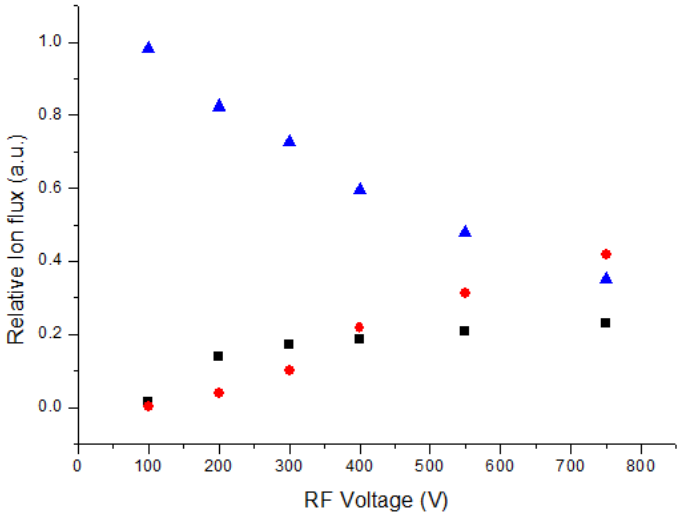

(a) 10 Pa

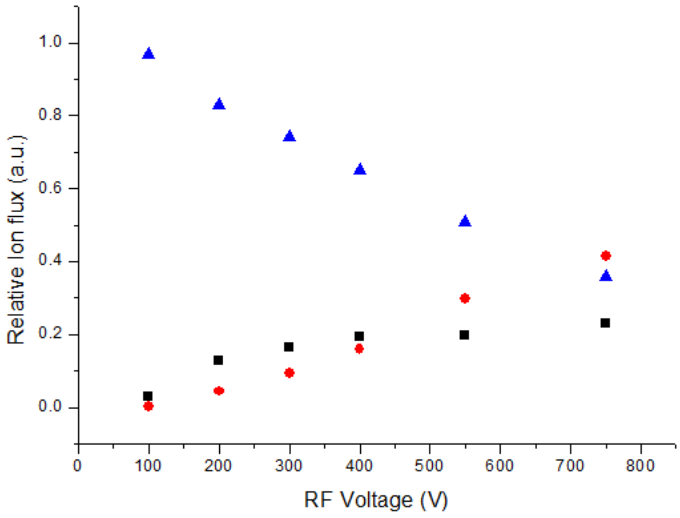

(b) 15 Pa

Figure 3.9: The relative ion flux as a function of RF applied voltage **(a)** 10 Pa and **(b)** 15 Pa. The black squares represent the H^+ ions, the red discs H_2^+ and the blue triangles H_3^+ ions.

hydrogen ions are shown. In comparison with the previous case (5.0 Pa) a more dynamic chemistry can be observed. For low voltage values the H^+ flux is higher than H_2^+ in both cases. Increasing the applied voltage, the H_2^+ flux grows while the H^+ is maintained constant and H_3^+ decreases. At 750V applied voltage, H_2^+ becomes the most dominant ion. The explanation for this is that with pressure increase the mean free path decreases, increasing the collision probability.

Figure 3.10 depicts the flux of ions reaching the electrode as a function of peak-to-peak applied voltages. For 10.0 Pa and 15.0 Pa operational conditions the total ion flux increases linearly with V_{pp}. At 5.0 Pa the curve presents a maximum for 400 V. For values of the applied RF voltage higher than 400V the number of ions reaching the electrode in unit time decreases. This reduction can be observed in Figure 3.2 where for applied voltages of 550V and 750V the height of the high energy peak is disproportionately dropping. The same behavior is observed for the 10.0 and 15.0 Pa cases but apart from the loss of height of high energy peak one can observe the rise of peak for small energy values. (at approximately one third of the peak energy Figure 3.3).

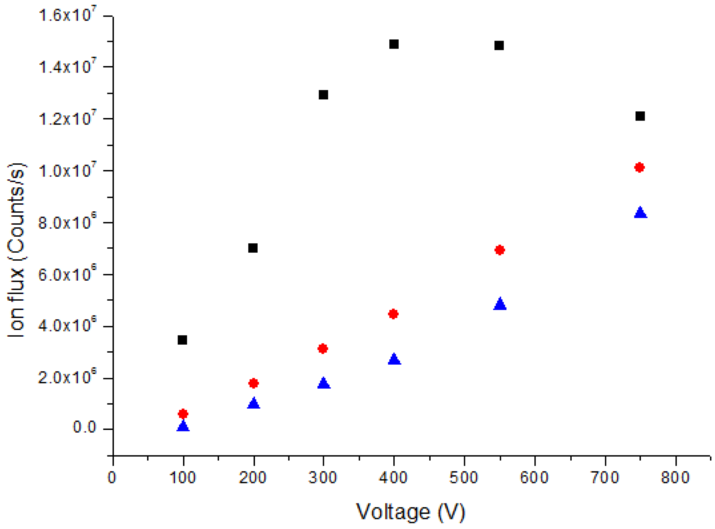

Figure 3.10: Total ion flux as function of the applied RF voltage for three different discharge pressures; (5.0 Pa - black squares, 10.0 Pa - red circles, 15.0 - blue triangles)

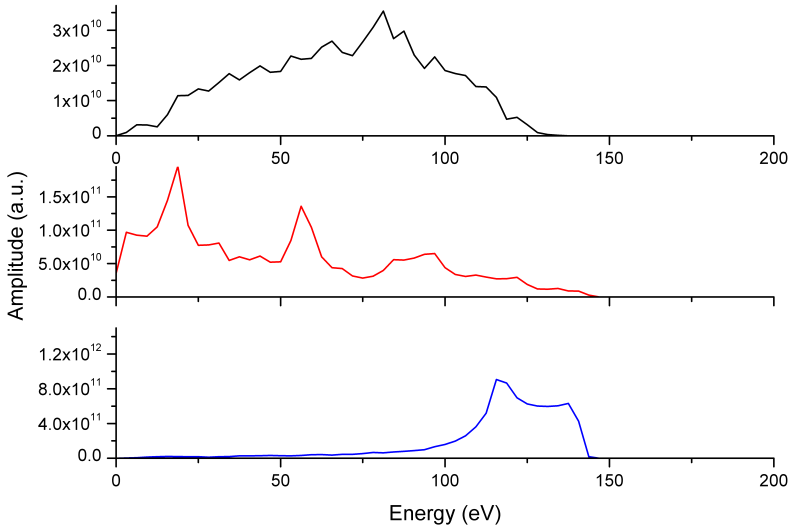

Figure 3.11: Simulated IEDFs for hydrogen ions; the black line represents H^+, the red line H_2^+ and the blue line H_3^+ ions in the experimental conditions of 15.0 Pa background pressure and 300 V input RF voltage

3.3 PIC simulation results for steady state plasma

In running the PIC simulation, the experimental conditions are chosen to be the same as for the experiment in order to directly compare the results and extend the interpretation. In order to achieve this, an extensive set of simulation runs covering all pressure and entire RF voltage space is performed. Figure 3.11 shows the simulated IEDFs for all positive hydrogen ions studied. The simulated results are directly compared with the experimental ones presented in figures 3.3 - 3.7

Figure 3.12 presents a comparison of the measured and simulated H_3^+ IEDFs; The red line shows experimental data, while the black line represents the simulated results for the experimental conditions of 10 Pa and 300 V. The shapes of the IEDFs for H_3^+ are very similar. The relative height of peaks and the energy separation are proportional. However, the peaks energy for the simulated results are higher than for the experimental ones. This can be explained by the nature of the simulation, which is a 1D code, compared with the experiment, in which

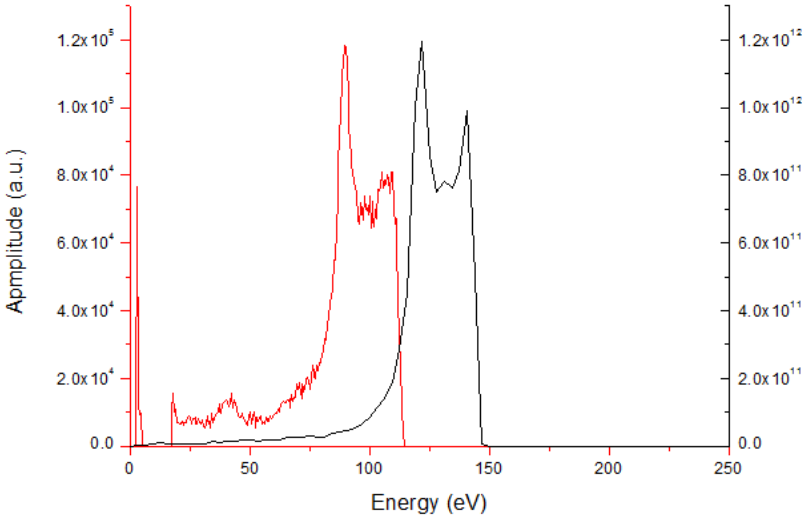

Figure 3.12: Comparison of measured (red) and simulated (black) IEDFs for 10.0 Pa and 300 V

particle losses take place in a 2D space. In addition, in the experiment there is a finite impedance of the plasma to the chamber, which will determine a lower RF voltage sensed by the plasma.

The ion species flux at the grounded electrode (Figure 3.13) exhibits a similar behavior to that observed in the experimental case (Figure 3.9a). At 10 Pa, the H_3^+ flux decreases by 40 % with the increase of the applied RF voltage. However, unlike from the experiment, in the simulation, the H^+ flux does not dominate the H_2^+ flux in any circumstances.

In plotting the flux of ions arriving on the electrode, only ions which strike the electrodes surface perpendicularly are taken into consideration . In the experiment even if the sampling orifice is very small (10 μs) some focal aberrations can occur.

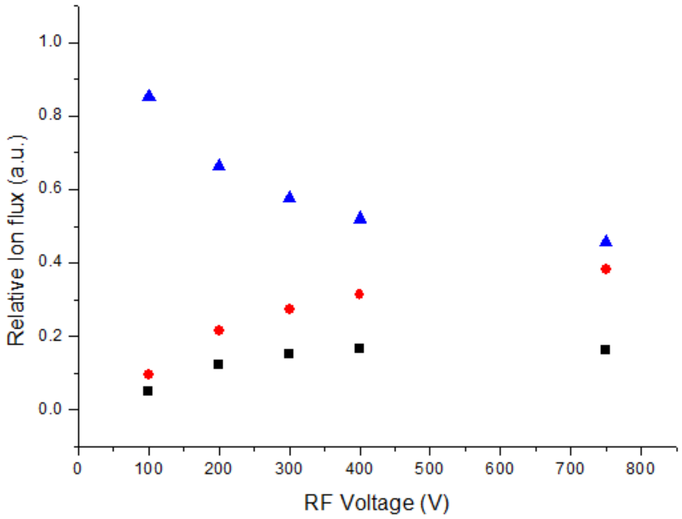

Figure 3.13: Simulated relative ion flux as a function of RF applied voltage for 10 Pa (H^+ - black squares, H_2^+ red circles, H_3^+ blue triangles)

3.3.1 Angular distribution of the IEDFs

Because the PIC simulation includes all three velocity components, is capable of investigating the variation in IEDFs for different incident angles onto the electrode. However, the angular resolution impacts the total simulation run time. For a realistic comparison with the experiment the resolution of the experimental device is roughly estimated. In the experiment, the ions are sampled by the sampling orifice of the mass-spectrometer. Considering this to be as schematically shown in Figure 3.14, for a particle to pass through the system, its incident angle should not be greater than φ_{max} which is given by:$\tan\varphi_{max} = \frac{L}{d}$ where L is the thickness of the orifice and d represents its diameter. In the experimental case these values are $L = 25\mu m$ and $d = 10\mu m$ which gives a value for φ_{max} of 21.81°. If an ion enters the orifice space with an angle greater than φ_{max}, it will strike the orifice walls and will not be detected.

In the simulation, the angular resolution has been chosen to be $\Delta\phi = 3.6°$. Plotting the IEDFs for different incident angles, it is noticeable that the ion density decreases dramatically with increasing angle, as is shown in the Figure 3.15.

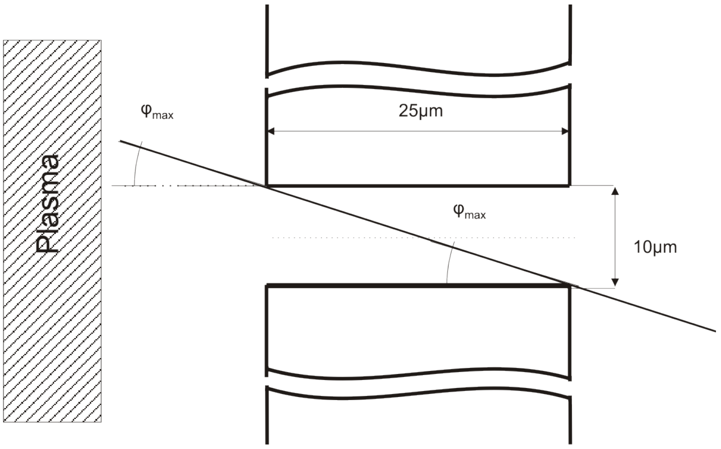

Figure 3.14: Sketch of sampling orifice and incident angles

Therefore, the contribution of ions that are not perpendicular to the electrode to the total ion flux at the electrode surface is negligible.

3.3.2 Charged particles density profiles

The PIC simulation diagnostics can determine the density profile for each charged species. This subsection presents a correlation of the results from the simulation with the results from the mass-spectrometer.

Figure 3.16 plots the results of the simulated spatial density profile for each charged particle species. The density axis is logarithmic in order to better discriminate the density variation in the sheath. Figure 3.16 shows that, as in the experimental case, the dominant ion species is H_3^+. They are found in relatively large proportions in the bulk plasma and also in the sheaths. Another interesting feature of the discharge that is revealed by the simulation is that the H^+ forms mainly in the sheath space, close to the electrodes. Looking into the hydrogen chemistry set, the reactions from equation 1.27 are found to be the dominant mechanisms for the production of H^+. The fact that H^+ forms mainly within the sheath, closer to the electrode boundary, indicates that the precursor particles are highly energetic. From the set of reactions responsible for H^+ production, the greatest cross-section for high energies is the dissociation of H_3^+. This reaction occurs without any energy transfer to the target molecule. Hence the newly

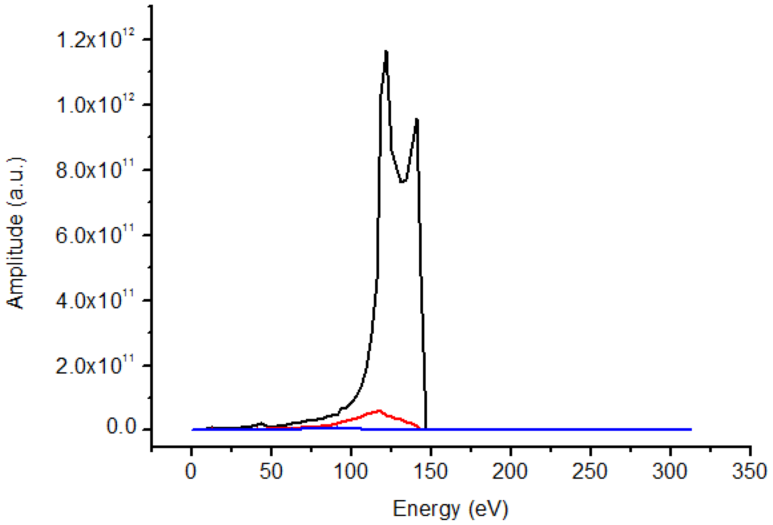

Figure 3.15: Simulated IEDFs of H_3^+ for 10.0 Pa and 300 V RF input voltage for three different incident angles; (black line $\pi/2$, red line $\pi/2 + \Delta\phi$, and blue line $\pi/2 + 2\Delta\phi$) where $\Delta\phi = 3.6°$

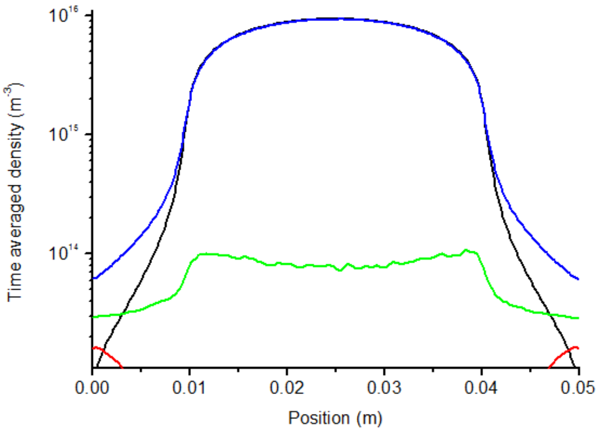

Figure 3.16: Simulated density profiles for electrons and positive hydrogen ions for 20.0 Pa and 300 V input RF voltage. The black line represents the electron density, red represents H^+, green H_2^+ and blue represents H_3^+.

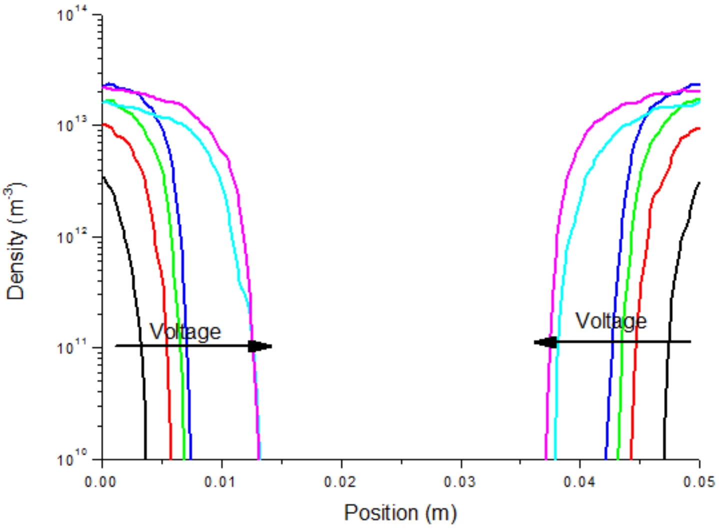

Figure 3.17: Density profile of H^+ for 10.0 Pa and variation of RF applied voltage

formed H^+ inherits the energy state of the H_3^+. In agreement with this result, Figure 3.17 shows the density profile of H^+ for different applied voltages. If the voltage increases, the H_3^+ ion will gain the necessary energy much faster. Hence the reaction will take place closer to the sheath edge for higher voltages.

The H_2^+ density profile (Figure 3.18) presents an interesting feature with a dip in the middle of the bulk plasma and a rise around the pre-sheath region. Plotting the density profile for the same applied voltage but for different pressure values (Figure 3.18), the density dip in the middle of discharge scales with pressure. The total number of H_2^+ decreases with the growth of the pressure, however, the flux of H_2^+ reaching the electrodes raises monotonically. The result in Figure 3.18 agrees with the hypothesis of H_3^+ forming within bulk plasma and is the result of H_2^+ association (1.26). Approaching the sheath boundary, another process becomes dominant. In this region, the electrons gain enough energy to ionize the background gas through impact collisions, forming H_2^+. The H_2^+ association takes place throughout the entire discharge volume, but the formation of H_2^+ by impact ionization is greater at the sheath edges. This explains the dip in the center of the discharge in the density profile.

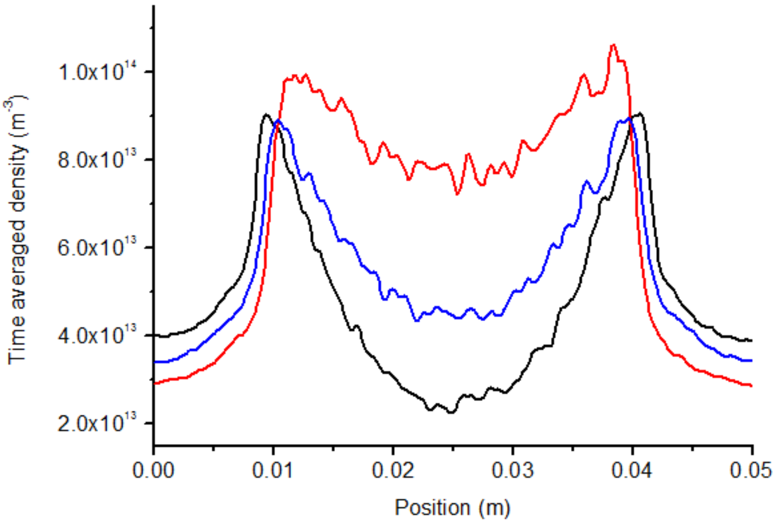

Figure 3.18: Averaged density profile of H_2^+ for 300 V applied voltage and pressure variation: 10.0 Pa red, 15.0 Pa - blue, 20.0 Pa black

3.4 Hairpin measurements

The hairpin probe, which is described in section 2.3, is used to measure the electron density spatial profiles for a direct comparison with those determined by the simulation. For this experimental setup, the prongs of the probe are bent in an L-shape and they are parallel to the electrodes.This provides a better spatial resolution for this particular plasma source design without affecting the probe performance. Using this arrangement, the spatial profile of the electron density is determined. The probe is mounted on the grounded electrode port and a scan versus the position between the electrodes is performed with a resolution of 2.0 mm. In the case of hydrogen discharges, the total plasma density is relatively low compared with argon or helium plasmas. In the sheath space, the electron density is even lower and in some cases this drops under the minimum density value that can be measured using the hairpin probe. Figure 3.19 illustrates the electron density profile comparison between the PIC simulation and hairpin measurements for 15.0 Pa gas pressure and 400 V peak-to-peak applied RF voltage.

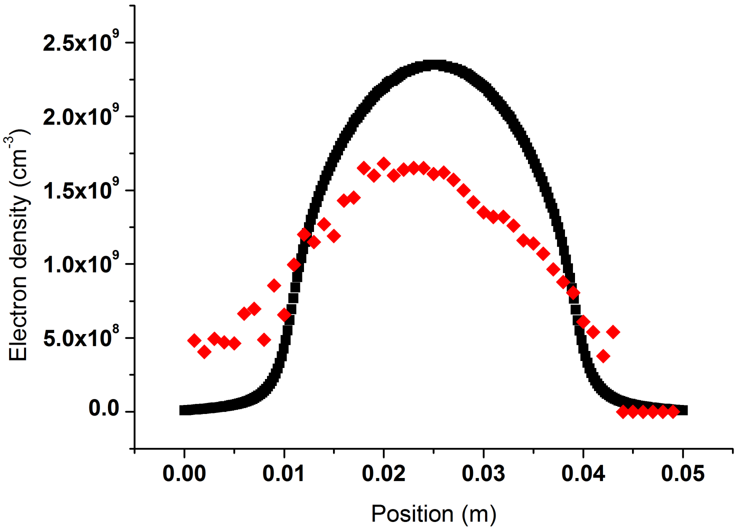

Figure 3.19: Comparison of measured electron density profile for 15.0 Pa gas pressure and 400 V; (red diamonds) with simulated one (black squares)

In figure 3.19 one can observe that the simulation overestimates the plasma density compared with the results obtained by the hairpin probe. This can be a consequence of the fact that the losses in the model are in one dimensional space (only to the electrodes surface) whereas in the experiment they occur in the two dimensions (the quartz confinement tube acts as a recombination surface). However, analyzing the sheath width region, it is noticeable that the ratio between the simulated and measured densities changes. This is actually an error introduced by the hairpin method used. Because the electron density is decreasing towards electrodes, there is a critical point in the discharge space, point where the electron density is below the sensitivity threshold of the hairpin. Around this the errors in measurement become important and affect the reliability of the data. There is also a systematic error introduced by the signal to noise ratio and by the method used to determine the resonance peak, as described in section 2.3.

Figure 3.20 presents the density profiles for 10 Pa background gas pressure and for four different applied voltages. It can be seen in the graph that all data points for the position 22 mm do not match the overall trend. It has been proved

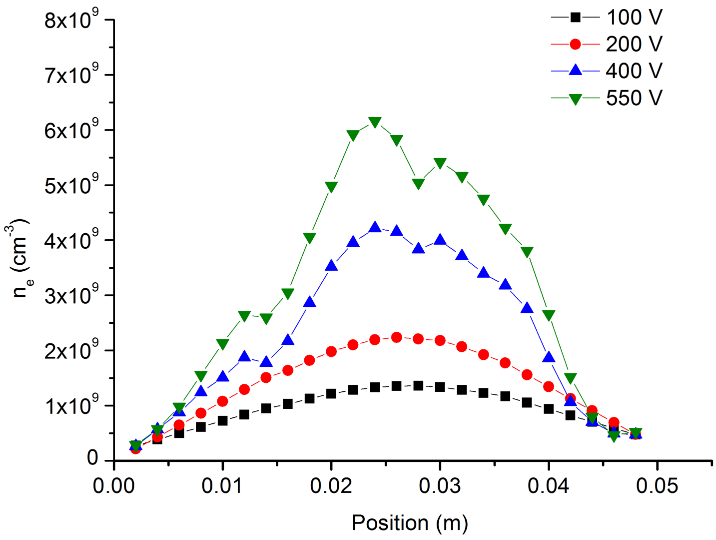

Figure 3.20: Measured electron density profile for different applied voltages and 10 Pa background gas pressure

that this is an artifact of the probe as described in section 2.3.

3.5 Indirect measurements of electron temperature

Previous sections have presented the characterization of the hydrogen CCP plasma using an energy resolved mass-spectrometer and a microwave resonance probe in conjunction with a PIC simulation. With the help of these methods, it is possible to collect the information about the energy distribution of ions striking the electrodes, the ion composition of plasma, and the dynamical chemical processes involved. In addition the electron density is measured across the inter-electrodes distance. For a better description of plasma, it would be advantageous to determine the electron temperature.

Analyzing equations (3.4) and (3.6), one can find that the peaks separation,

ΔE, depends on the sheath potential drop and the mean sheath width:

$$\Delta E_i = \frac{8e\tilde{V}_s}{3\bar{s}\omega}\left(\frac{2e\bar{V}_s}{M}\right)^{1/2} \tag{3.11}$$

where $\bar{s}$ represents the mean sheath width and V_s the instantaneous sheath voltage, which is assumed to be sinusoidal given by: $V_s(t) = \bar{V}_s + \tilde{V}_s \sin\omega t$. Substituting the sheath thickness in (3.11) results in:

$$\Delta E_i = \frac{8e\tilde{V}_s}{\omega}\left(\frac{2e\bar{V}_s}{M}\right)^{1/2}\frac{1}{\sqrt{2}\lambda_D}\left(\frac{kT_e}{2e\bar{V}_s}\right)^{3/4} \tag{3.12}$$

Substituting for the Debye length and solving the equation 3.12 for the electron temperature yields:

$$kT_e = \frac{\omega^4 e\bar{V}_s}{512\left(e\tilde{V}_s\right)^4}\left(\frac{\epsilon_0 M}{n}\right)^2\left(\frac{\Delta E_i}{e}\right)^4 \tag{3.13}$$

Measuring the electron density at the sheath edge and in the assumption of the ion flux conservation it can be written that:

$$\Gamma(x=0) = \Gamma(x=\bar{s}) \tag{3.14}$$

which is equivalent with:

$$\Gamma(0) = n_e v_B = \Gamma_0 \tag{3.15}$$

where n_e is the electron density at the sheath edge and v_B is the Bohm velocity [15] which is introduced by equation (1.16). Because the quasineutrality condition is still true at the sheath edge, $n = n_e = n_i$, measuring the electron density at the sheath edge and the energy spread of the IEDF, the plasma electron temperature at the sheath edge can be determined.

Figure 3.21 shows the ion energy spread of the saddle-structure, the sheath voltage, the measured sheath-edge density, and the resultant electron temperature from Equation 3.13 for discharge pressure of 5 Pa - black squares, 10 Pa - red dots and 15 Pa - blue triangles. For constant values of the pressure, an increase of the electron temperature with the rise of the input voltage can be observed. A sensitive point of this theory is the determination of the sheath edge position. Although the sheath edge was introduced from the early times of the plasma

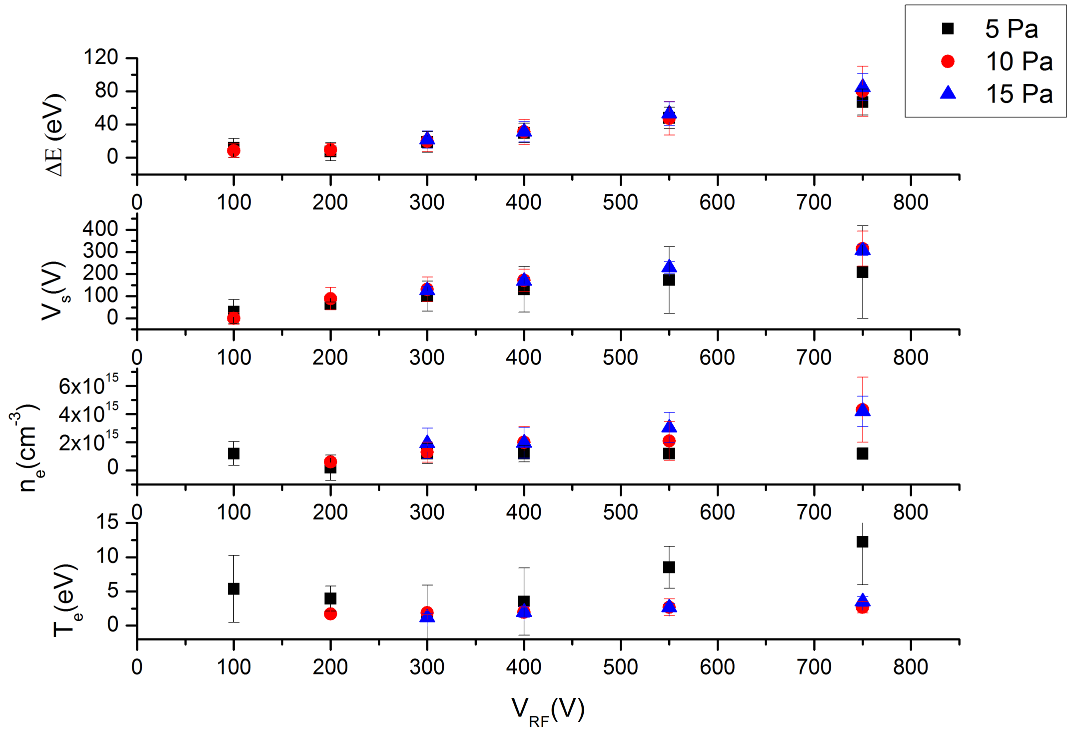

Figure 3.21: Plot of energy broadening, averaged sheath potential, electron density at the sheath edge and calculated electron temperature as a function of the input voltage for three values of the gas pressure (black squares 5.0 Pa, red circles 10.0 Pa, blue triangles 15.0 Pa)

theory [55], the scientific community does not entirely agree on how the sheath edge is defined [56, 57, 58, 59].

The model predicts the electron temperature with large errors especially for the low pressure case. This is due to the electron density square dependency of the plasma temperature in 3.13. For the low density case the hairpin approaches its lower sensitivity limit and its results are affected by the sheaths forming around hairpins prongs. The result depicted in Figure 3.21 contradicts with the global models [15], which predict an insensitiveness of the electron temperature with plasma density and furthermore with input power. The results of the present model show an increasing tendency of electron temperature to the input power. This can be determined by the electron density measurements, which does not scale with the power as predicted by the global models.

4

Study of the afterglow phenomena in a hydrogen CCP discharge

Pulsed plasmas have been successfully used in material processing applications, such as reactive ion etching [60], plasma immersion ion implantation [61], pulsed magnetron sputtering [43], plasma polymerization [62] and for producing energetic electron beams such as pseudospark discharges [63, 64]. The advantages of operating the discharge in pulsed mode vary with the type of application. For example, by operating a magnetron sputtering target in pulsed mode, better quality coatings are deposited on a substrate when compared to dc-magnetron sputtering. This is related to enhancement in plasma density, electron temperature and ion energy distribution [60].

The present investigation entails experimental measurement of the ion energy distribution and electron density during the transition from the on-phase (active plasma) to the off-phase (afterglow plasma) of a pulsed H_2 discharge, in a confined symmetric electrode system powered by applying a 27.12 MHz radio-frequency voltage with a 50.0% duty-cycle and 1.0 ms period. The IEDFs in the afterglow are measured using the Hiden energy resolved mass-spectrometer. The electron density decay is measured using the floating hairpin resonance probe.

The experimental methods used for time resolved measurements are described in section 2.1.

In order to collect the ion energy distribution function, the collector is gated for 1.0 μs collection period at a fixed time in the pulse period. The data is collected over multiple pulses, assuming the pulses are equivalent. After collating the energy spectra at the given time delay, the time delay is incremented. In this way, complete time resolved energy spectra are obtained. In oder to measure the electron density, the microwave source is set to a frequency and the probe signal is collected over the full pulse cycle. The probe signal peaks when and if the probe and the plasma system are in resonance. At subsequent pluses, the frequency is incremented and the time of the new resonance is recorded, yielding density versus time in the pulse.

Similar to the steady state case, the *en* PIC code is used to simulate the pulsed discharge. The code is run with the input file describing the desired experimental conditions to reach steady-state. After simulating $\approx 50.0\mu$s, steady state is achieved and the simulation run is stopped. The input file is modified with the voltage on the powered electrode set to zero volts. The simulation is restarted using the particle positions and fields of the steady-state solution. The plasma parameters are tracked as the plasma relaxes under the conditions of no driven RF voltage. In this way is created the modulation of the input RF voltage comparable with the experiment.

4.1 Evolution of IEDFs in the afterglow

The transitory phenomena are known to have a great impact in many physical systems, and studies of these have been a great challenge for physicists even from the beginning of the previous century. They recognized the importance of the transitory phenomena which occur in different systems. The time resolved measurements have become popular in the recent years due to increased development of fast acquisition techniques. In this work, the energy resolved mass-spectrometer is used to determine the evolution of the ion energy distribution in the afterglow. With the setup shown in Figure 2.7, the discharge is pulsed

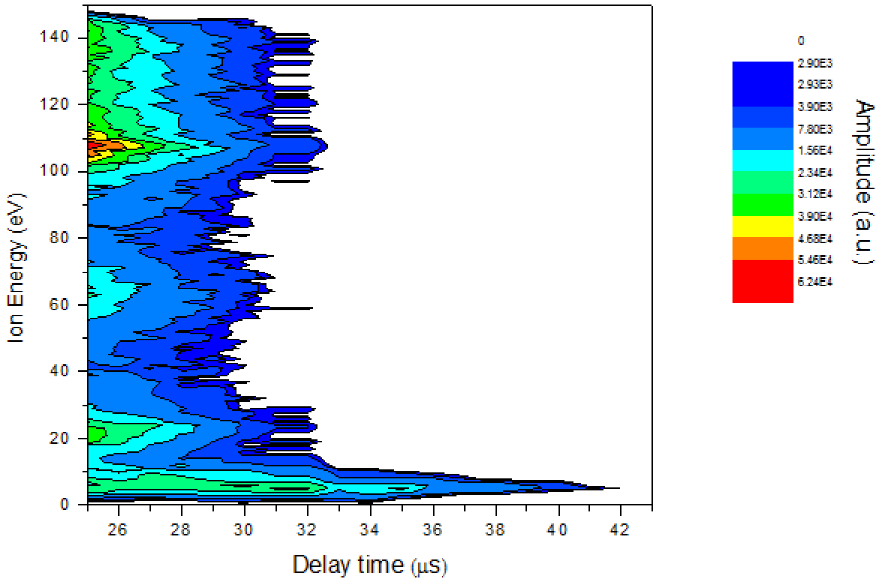

Figure 4.1: The temporal evolution of the H_3^+ into the afterglow for 15.0 Pa and 300 V (in the ON phase)

with a duty cycle of 50.0% at a frequency of 1.0 KHz. The plasma pulse and the mass-spectrometer detector are synchronized. The detector is enabled for a 1.0 μs period in the afterglow. The experimental conditions cover the same operational space as for the steady state case (peak to peak voltage 100V - 750V, pressure range 5.0 to 30.0 Pa). The IEDFs are determined using the procedure described in section 2.2.2. The resolution of the mass-spectrometer is one microsecond. The H_3^+ ion decay is chosen for study because it is the dominant ion species for this discharge, as shown in section 3.2. It has also been shown that the H^+ ion is produced within the sheath space. The H_2^+ is mostly produced localized at the sheath boundary. Thus the IEDFs of H^+ and H_2^+ do not contain the same amount of information as the IEDFs of H_3^+, which are produced within the plasma bulk. The data for H_3^+ ions is represented in Figure 4.1 where the X axis is the time in the afterglow, the Y-axis is the ion energy and the colors represent the ion counts in unit time.

In figure 4.1 the X axis starts from 25 μ because there is a delay of approximately 25 μs between the RF-OFF trigger and the beginning of the decay in the mass-spectrometer signal. The first 1 μs is due to an internal delay in the RF generator; this can be seen in Figure 2.4b. The remaining delay is due to the ion transit through the mass-spectrometer. The pass-energy of the mass-spectrometer is set at 40 eV. In section 2.1 the mass-spectrometer is described. The ion beam travels through the mass-spectrometer body at a constant speed, except for two sections. The first one, the sampling section, is the section where the ions are sampled, focused, and accelerated to the 40eV energy. This section is much smaller than the constant energy part. The second section is the detection section, where ions are decelerated to a constant energy ($\approx 2eV$)in order to be easily detectable by the detector. The space extent of this section is very limited. For the H_3^+ ion, the time of flight in the mass-spectrometer body is calculated to be approximately 22-23 μs.

The false color chart represents the measured amplitudes, with red for the highest and blue for the minimum. In Figure 4.1, the high energy peaks (for example, the peak at 108 eV) decay quickly (in about 5.0 μs), while the low energy peak (below 10 eV) persists into the afterglow for an additional 12 μs. This behavior seems rather unusual, since one would expect to observe a cooling down of the high energy states. Instead, a coexistence of high and low energy peaks for about 5 μs is observed.

Repeating the same experiment with the simulation code a fast decay of the H_3^+ energy is obtained. In this case, the number of ions in high energy state decreases to zero in less than one microsecond. The fast decay seen in the simulation data explains the total disappearance of the high energy population in the measurements performed with the Hiden system. Because these measurements have a minimum time resolution of 1 μs, a resolution limited by the detector construction, the instrument is not sensitive to resolve the faster, smooth decay of the ion energy seen in the simulation. However, it is notable that the long persistence (approximately 10 μs) of the low energy ion population exists in both experiment and simulation. The Hiden system detects a persistence of 3 eV ion population in the afterglow for 10 μs after the high energy ion population disappears. A similar behavior was reported by [65] for a hydrogen inductive coupled

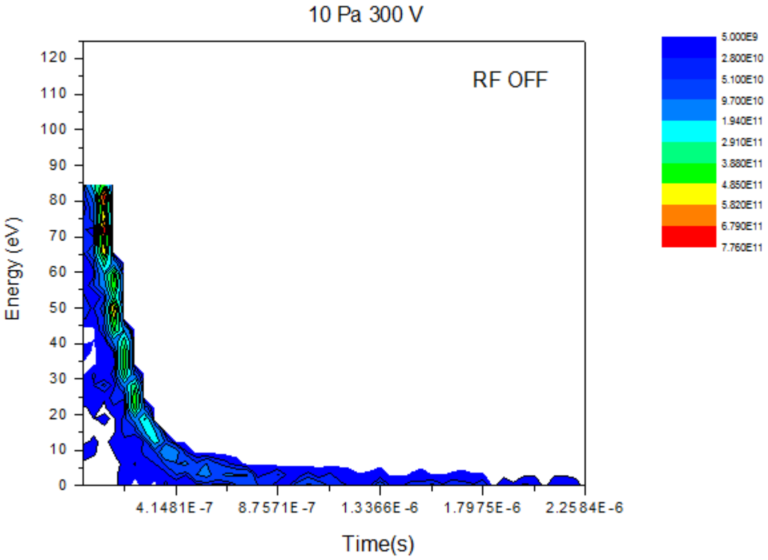

Figure 4.2: Simulated temporal evolution of the H_3^+ into the afterglow for 10.0 Pa at 300 V

discharge (ICP), where a peak in the H_3^+ energy distribution remained constant at a value of 2.0eV for approximately 500 μs. The 3eV energy peak of ions reaching the electrode corresponds to a sheath sustained by an electron population with temperature of 0.75 V. This result is surprising as one would expect the electron temperature to drop monotonically, with a constant rate to zero. The long persistence of the electron population into the afterglow could be the result of super-elastic collisions between electrons and vibrationally excited molecules. Vibrationally excited molecules are created during the "ON" phase of the pulse cycle and they persist further into the afterglow because of a relatively longer lifetime. The super-elastic collision is described the equation 4.1 where $\vec{e}$ represents the electron which gained energy equal to the energy lost by the hydrogen molecule due to transition from the excited state $\nu = x + 1$ to the lower energetic state $\nu = x$.

$$e + H_{2(\nu=x+1)} \rightarrow \vec{e} + H_{2(\nu=x)} \tag{4.1}$$

Super elastic collisions (SEC) for hydrogen have been reported [66, 67]. It is theoretically predicted that the cross sections of SEC increase with a decrease in the electron energy.

4.2 Electron density decay in the afterglow

The temporal evolution of the electron density is measured using the hairpin probe setup, as described in section 2.3. The experimental conditions are the same as for the previous experiment (the peak to peak RF voltage in a range of 100V to 750V at 27.12 MHz and background gas pressure varying from 5.0 Pa to 30.0 Pa in 5 Pa steps). Simulation of the temporal decay of the electron density is performed using the same values for the gas pressure and applied voltage as in the experiment.

4.2.1 Time resolved measurements of the electron density using the hairpin probe

Figure 4.3 presents the electron density measurements are performed in the center of the discharge. It can be observed that for the "ON" phase with constant applied RF voltage, an increase in the gas pressure results in increase of the measured electron density. This is expected, because, increasing the pressure, leads to a decrease in the mean free path, hence increasing the collision probability. As a result, the ionization rate rises and the measured electron density should therefore increase.

Figure 4.4 plots the curves of electron density versus time into the afterglow. Also shown is the measured RF voltage waveform at the electrode. It is worth noting that the RF voltage oscillation reduces to practically zero within 3 RF periods (0.1 μs). For time intervals greater than 25 μs into the afterglow, the electron density shows a monotonic decay for all gas pressures. The high-frequency oscillations seen in the electron density are thought to be anomalous and caused by pulse-to-pulse variations, although the 40 MHz bandwidth of the hairpin technique used here would be sensitive to electron oscillations in an ion-acoustic timeframe, but not at the electron plasma frequency. The most surprising result occurs during the initial 25 μs of the OFF phase. During this

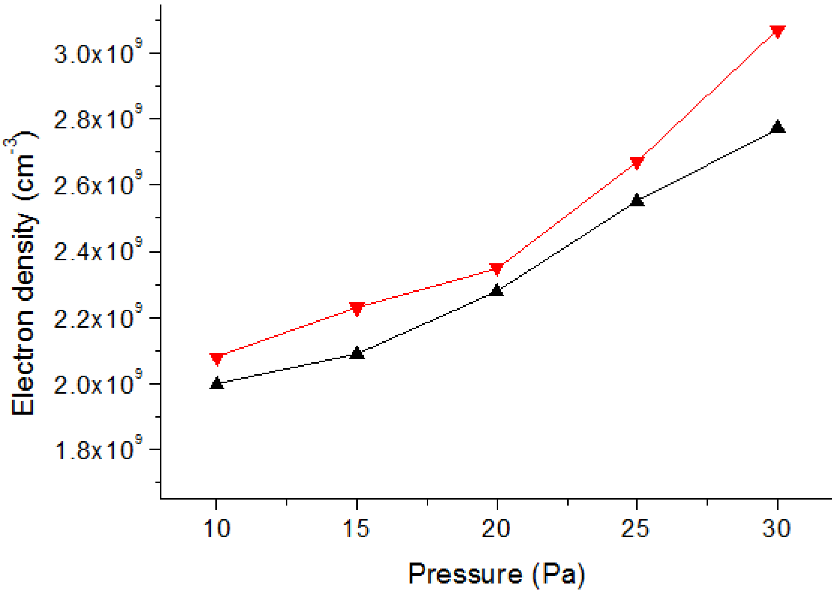

Figure 4.3: The electron density in the ON phase of the discharge as function of the hydrogen pressure for 500V (red) and 400V (black) applied voltage, in the middle of discharge (d = 25.0 mm)

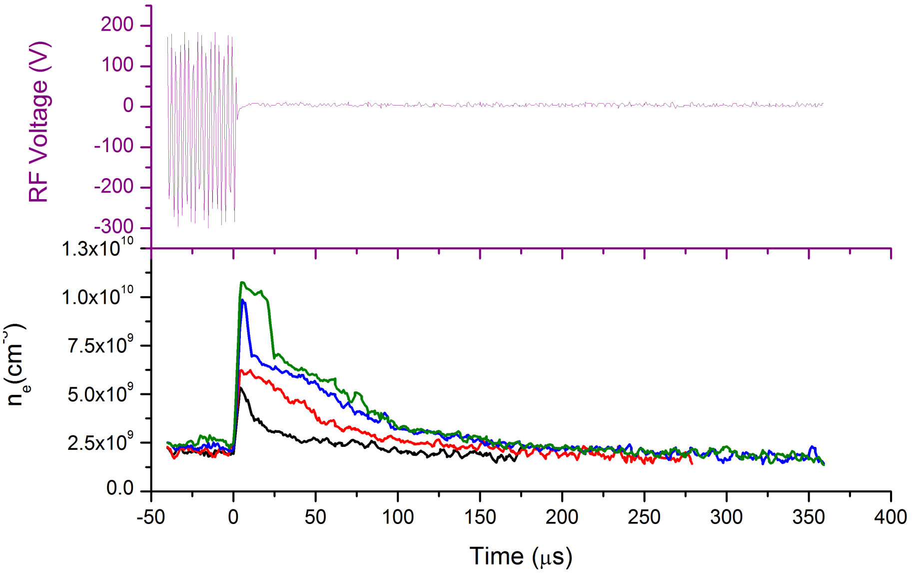

Figure 4.4: The electron density decay in the afterglow for 15 Pa (black), 20 Pa (red), 25 Pa (blue) and 30 Pa (green) and discharge RF voltage 500 V. The purple line represents the voltage waveform.

small time window, the electron density suddenly increases, followed by a monotonical decrease until the density drops below the instrument sensitivity. This anomalous density rise is seen for all pressures and RF voltage combinations.

In seeking an explanation of the anomalous density increase, in the first instance it is necessary to determine whether this behavior can be explained by experimental errors in the RF power or plasma density diagnostic system. In the literature, such jumps of the plasma parameters have been reported and attributed to an overshoot of the RF power supply. Figure 2.4b illustrates that, in the CIRIS experimental setup, the electrode voltage does not exhibit any overshoots. The next step is to question the diagnostic method. It is important to determine whether the measured values are "true" results, and not a false measurement due to sheath formation. In order to answer this question, it is necessary to return to the hairpin theory. Recall that, the hairpin probe measures the dielectric constant of the medium between the hairpin prongs. As described in section 2.3.3, if a sheath forms around these prongs the electron density will be underestimated.

Figure 2.13 illustrates the hairpin prongs and considering that a sheath forms around each of these prongs. Because there are no electrons in the sheath regions, the dielectric constant is equal to the vacuum dielectric constant ϵ_0. In this case, the hairpin will underestimate the electron density with a factor which depends proportionally on the sheath thickness in relation to the space between the hairpin prongs. Increasing the gas pressure and keeping the RF voltage constant, the plasma density increases monotonically (Figure 4.3). From the sheath thickness relation:

$$s = \frac{\sqrt{2}}{3}\lambda_{De}\left(\frac{2eV}{kT_e}\right)^{3/4} \tag{4.2}$$

recalling the Debye length as defined in 1.6, by introducing it in the sheath width relation 4.2, it is found that the sheath width depends inverse proportionally on the square root of the plasma density. Hence an increase in the plasma density will lead to a decrease in the sheath thickness. Returning to the assumption about sheath formation around the hairpin prongs, an increase in electron density leads to a decrease in the electron density underestimation due to the sheath effect reduction. From Figure 4.3, it can be noted that the plasma density is greater at high pressures. From equation (4.2), the sheath thickness, and thus the density error, decreases with growing plasma density. However, the experimental data shows that the difference between the "on-state" density and the peak in the anomalous "off-phase" density is greatest at the high density case. Thus any error caused by the floating hairpin that completely follow the plasma potential oscillation would further increase the observed plasma density rise during the first 25 microseconds of the afterglow.

In order to test this hypothesis, it is supposed that the overshoot effect is due to the sheath formation around the hairpin prongs during the ON phase. The sheath around the prongs is giving a falsely anomalously low density during the on-time. In the afterglow, when the RF voltage is switched OFF, the sheath collapses. For an increase in the background pressure, the sheath thickness decreases. This implies that the underestimation effect should become smaller with

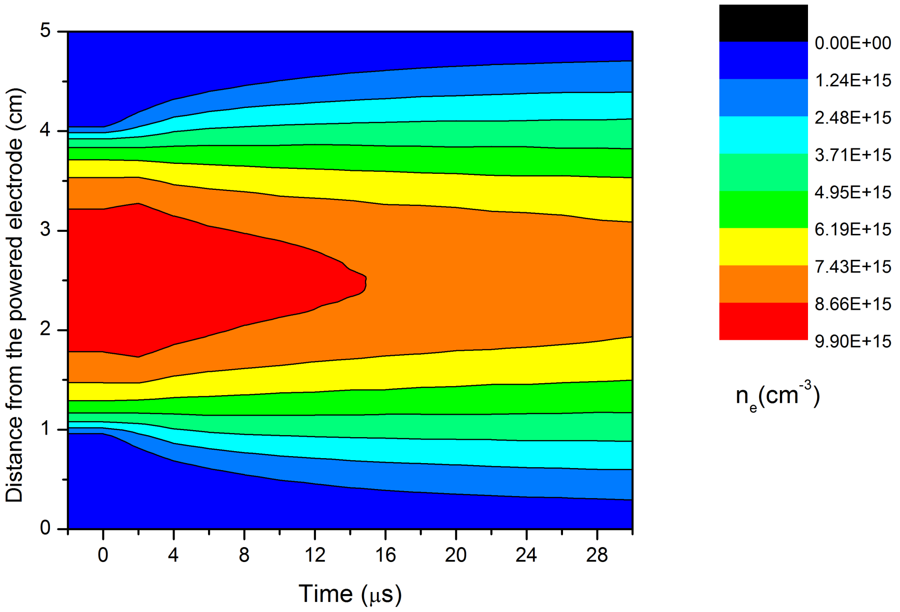

Figure 4.5: Simulated electron density decay for 15.0 Pa and 400 V

pressure increase. However, the data shows that the overshoot substantially rises with pressure, which is in contradiction with the above model. The sheath effect on the hairpin probe will be more visible for low values of plasma density and will have less effect on the results for higher density values. Thus, an explanation of the density rise based on the formation of an RF sheath around the hairpin resulting in an underestimation of n_e is false.

It should be noted that, from its design, the hairpin is a floating metal probe in contact with plasma and with high RF impedance to the ground. The intent of this design is to prevent the formation of RF sheaths around the prongs, allowing for an accurate measurement of the electron density.

4.2.2 Time resolved simulation results

Figure 4.5 shows the evolution of the simulated electron density in the afterglow. The x-axis represents the time in microseconds, and zero is the moment when the RF power is switched OFF. The y-axis represents the position between the

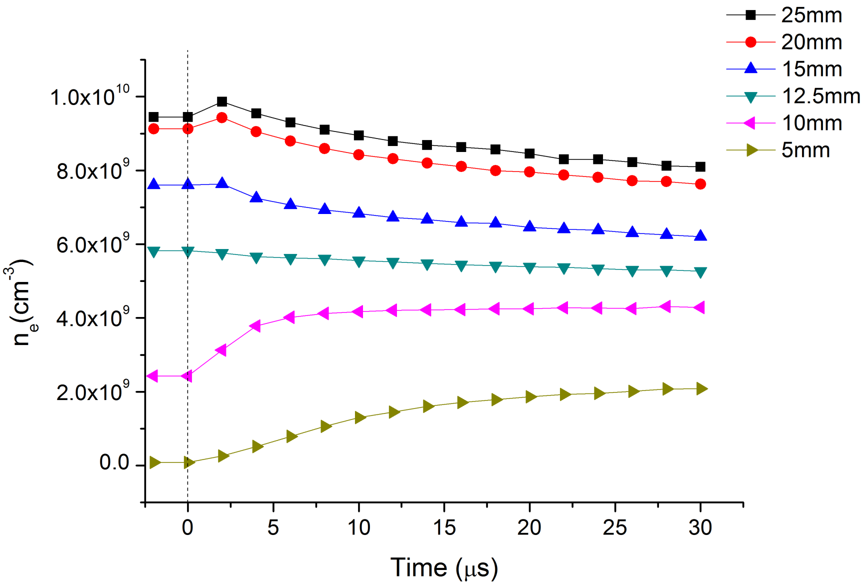

Figure 4.6: The electron density from the PIC simulation in the afterglow for 15 Pa and 400V for different spatial positions in the discharge.

electrodes. Density is depicted using the false-color scale, from blue at the lowest to red at the highest, overlayed with equally spaced contour lines. The decay of the electron density can be seen. In addition, the collapse of the RF-sheath is illustrated by the increase in the electrons penetrating the space near the electrodes.

Because the color representation in Figure 4.5 is not sensitive enough to observe fine variation in the density, a few spatial points are chosen and the same data is plotted in a two-dimensional manner in Figure 4.6. Here, the vertical dashed line refers to the moment when the power is switched off. In this representation, there is a small increase in the plasma density for positions close to the center of the discharge (25 mm, 20mm) immediately after the RF voltage is switched off. For probe positions of 5 and respectively 10 mm the increase is extended in time. The latter increases can be explained by the collapse in the electron temperature and therefore the collapse in the RF sheath and the associated pre-sheath. When the sheath potential collapses, the electrons penetrate the space closer to the electrodes. In the experimental case, the electron

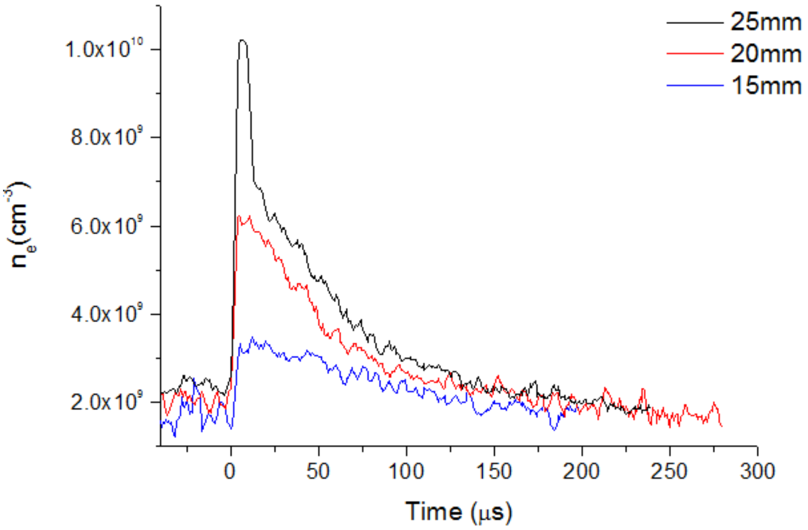

Figure 4.7: The experimental electron density evolution in the afterglow for three different positions measured in respect to the powered electrode. The black line represents the center of discharge (25.0 mm), the red line represents 20.0 mm and the blue one represents 15.0 mm in front of the powered electrode.

density within the sheaths cannot be measured due to the low electron density, which is lower than the values which a hairpin can measure. These results are shown in Figure 4.7. The peak ratio decreases from the middle of discharge to the electrodes.

4.2.3 Discussion of the time resolved results

Casting the phenomenon in terms of particles balance, the possible explanation for this distinct rise in electron density could be attributed to the following mechanisms: (i) additional ionization or sustainment of ionization in the decay phase; (ii) reduced losses to the boundaries. A combination of these effects could lead to enhancement in plasma density.

In a symmetric CCP-discharge, the displacement current through the high voltage sheath at each electrodes are conserved by oscillatory fast electrons in the bulk plasma. Therefore bulk plasma is comprised of plasma electrons n_{pe} and ions n_i, a fraction of hot plasma electrons n_{he}, and a component of fast oscillatory electrons n_{fe}. The contribution of the fast oscillatory electrons will monotonically decrease with time after $t \approx 2\mu s$. However, the plasma electrons and most of the hot electrons are still confined in the discharge due to significant negative potential on the electrode until the external blocking capacitor is fully discharged. Fast residual electrons from the post active-discharge could contribute to ionization process as these electrons are rapidly cooled through successive collisions with neutrals while their energy approaches close to the ionization threshold. If the loss mechanisms do not change significantly from that in the active phase, then this would increase the density as observed in the present investigation.

With this increase in overall electron density, the ion density must also increase in order to maintain the quasineutrality of the plasma, $n_i \approx n_{pe} + n_{fe}$. This happens self-consistently since the losses to the walls via ambipolar diffusion are significantly reduced due to decrease in T_e, as a result of electron cooling in the afterglow.

The second hypothesis is sustained by the "field reversal" phenomenon [68, 69]. The phenomenon appears in the hydrogen discharges due to relatively high mobility of the hydrogen ions During the field reversal period, results a strong electronic current. Once the applied voltage is turned off, the field reversal is no longer present. This implies that, immediately after switching off the power, the net electron collection decreases. It should be noted that during the ON phase, a negative DC bias is developed. Figure 4.8 presents the voltage at the powered electrode at the end of the ON phase. One can see that the powered electrode voltage extinguishes through a DC bias which will decay to zero in approximately 2 μs. This decay time is determined by the quality factor of the tuning element. During this time, the slow electrons are repelled by the powered electrode, which is negatively biased. Hence, during this transient, the recombination boundary of electrons reduces in comparison with the recombination boundary during the ON phase. A combination of these two effects could lead to an enhancement in plasma density.

A further effect which will lead to an increase in the ion density is the ion neutral collisions in the sheath. The collisions in the sheath will reduce the ion

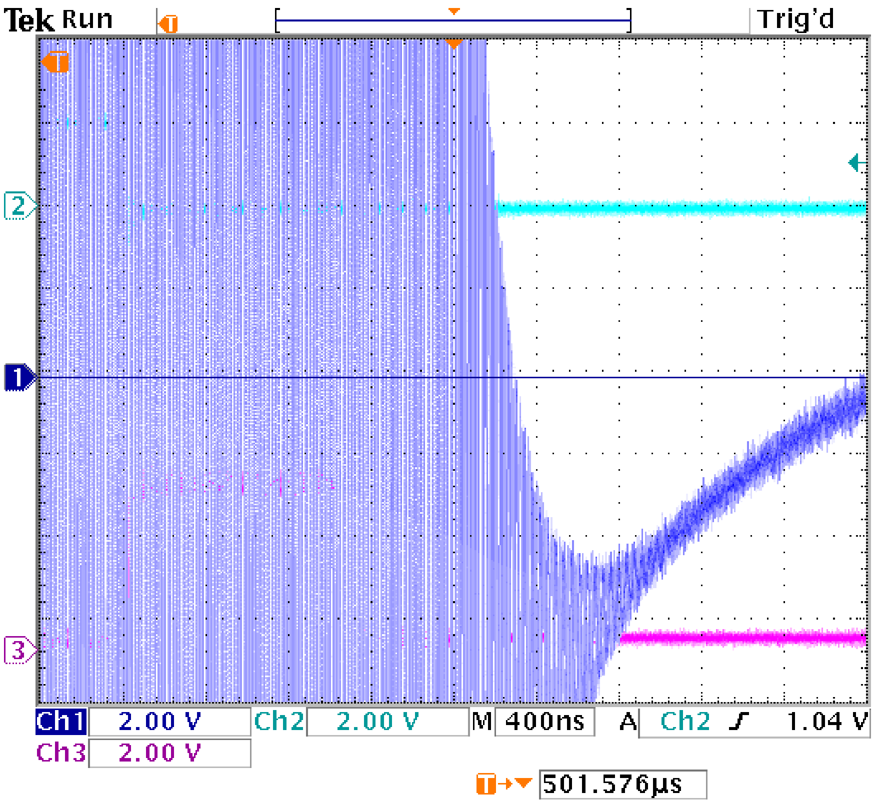

Figure 4.8: The voltage waveform of the powered electrode at the end of the ON phase.

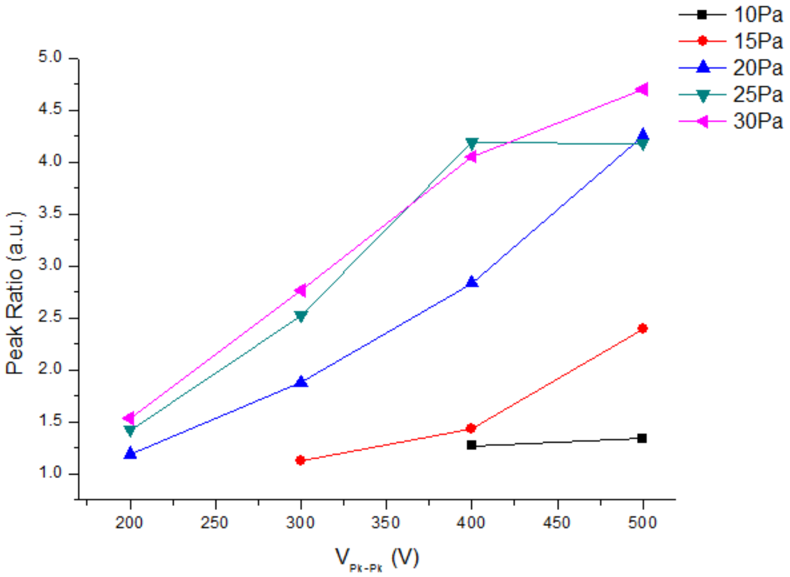

Figure 4.9: The ratio of the peak density in the afterglow to the density in the ON phase vs. the peak to peak voltage for different values of the gas pressure. The position of the probe is in the center of the discharge with the plane of the hairpin parallel to the electrode surface.

mobility, hence the ion loss to the walls and will further enhance the plasma density in the afterglow. This is consistent with the data shown in Figure 4.9, which shows that the normalized peak density with the density during the active phase, rises with increase of the gas pressure.

4.3 Determination of the electron temperature

The earlier results [70] relate the Debye length to the discharge chamber ratio with the diffusion process. Hence, if the Debye length is much smaller than the discharge characteristic length, the diffusion processes are governed by ambipolar diffusion. This is the case for the early afterglow, when the plasma density is large. After the plasma density decays and the Debye length becomes larger than the characteristic length of the system, the diffusion becomes a free fall diffusion.

In this case the loss rate can be written as:

$$\frac{\partial n_e}{\partial t} = -\nu_{diff} n_e - \alpha n_e^2 + \beta n_i^2 \tag{4.3}$$

where ν_{diff} represents the diffusion rate and is given by $\nu_{diff} = \frac{D}{\Lambda_c^2}$, with D the diffusion coefficient and Λ_c the characteristic length of the discharge; α and β refer to the losses and production due to the recombination of electrons with hydrogen ions.

Assuming, in first instance, that the decay of electrons is governed only by the diffusion processes, and neglecting the recombination processes for the early stages of the afterglow, introducing in equation (4.3) the diffusion coefficient:

$$D = \mu_{ion} \frac{kT_e}{e} \tag{4.4}$$

which is proportional with the electron temperature, (4.3) becomes:

$$\frac{\partial n_e}{\partial t} = -\frac{\mu_{ion}}{\Lambda_c^2} \frac{kT_e}{e} n_e \tag{4.5}$$

In [71] a separation of variables for the early stages of the afterglow is proposed. Hence the electron density evolution can be written as:

$$n_e = n_{e0} e^{-t/\tau} \tag{4.6}$$

where $\tau = \frac{\Lambda_c^2}{\mu_i} \frac{e}{kT_e}$. Using equation 4.6, one can determine the electron temperature at the e-folding time into the afterglow to be 0.35 eV. Rewriting equation 4.5 to express the electron temperature function of the density variation the following equation is obtained:

$$\frac{kT_e}{e} = -\frac{\Lambda_c^2}{\mu_{ion}} \left(\frac{1}{n_e} \frac{\partial n_e}{\partial t} \right) \tag{4.7}$$

The electron density is numerically differentiated, and equation 4.7 can be used to determine the electron temperature as a function of time in the afterglow. In the above theory, the unexpected rise in the density is neglected and the afterglow is considered to start once the electron density is falling.

Figure 4.10 plots the time evolution in the afterglow of the measured electron density (red line) in the center of discharge and the estimated electron temperature (black line). As expected, the electron temperature decay is slightly faster

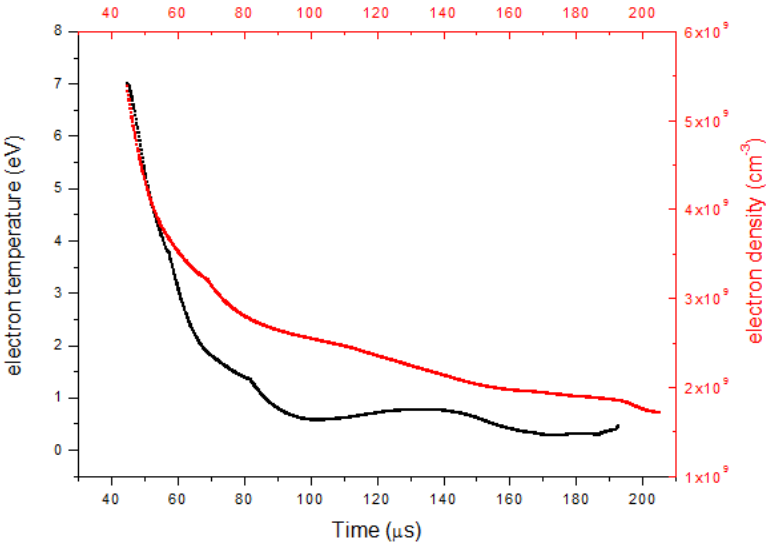

Figure 4.10: Evolution of measured electron density (red) and electron temperature (black) in the afterglow

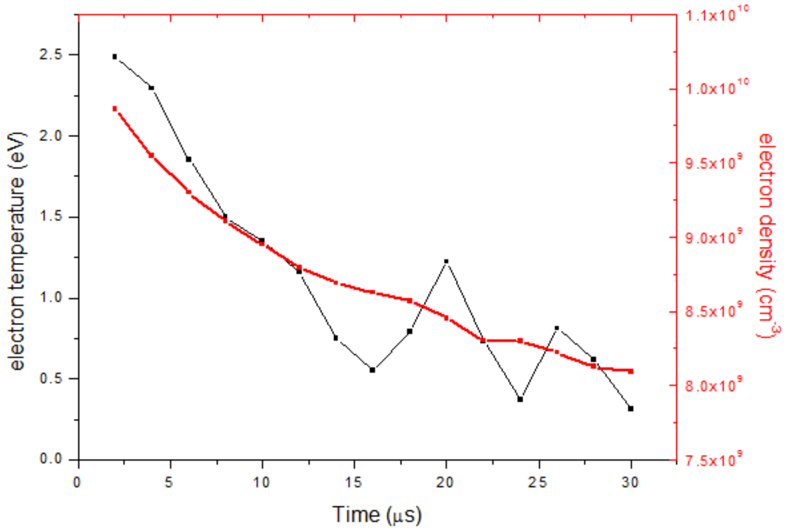

Figure 4.11: Evolution of simulated electron density (red) and electron temperature (black) in the afterglow

than the density decay. The results are consistent with the results presented in section 4.1, which predicts an electron temperature of 0.75 eV into the long afterglow.

Plotting the PIC simulation results in the same manner (Figure 4.11), it can be observed that the decay rate in the simulation case in greater than in the experiment. At the same time, the electron temperature in the ON phase is smaller. The electrons kinetics in an afterglow hydrogen CCP discharge is very complex. This model approach is a very simplistic, but it can help in estimating the electron temperature in the ON phase without solving complicated time and space dependent kinetic equations.

5

Conclusion

In this work, experiments performed in a modified GEC cell, capacitive coupled plasma source operating in hydrogen have been presented. The first set of experiments is the study of the continuous wave discharge where the plasma was produced for different combinations of background pressure and 27 MHz RF voltages. In the second set the RF voltage was pulsed with a 1 kHz, 50% duty cycle square function. In this latter experiment, the post discharge phenomena were studied.

The main diagnostics used in both configurations are the Hiden EQP energy resolved ion mass-spectrometer and the hairpin probe for measuring the electron density. PIC simulations are obtained in the same conditions as for the experiment. The experiments were performed for a pressure range of 5 to 30 Pa and the applied radio frequency voltage varied from 100 V to 700 V. Measurements of IEDFs and plasma density profiles from the experiment and simulation are directly compared.

The first results consist in a characterization of the steady-state hydrogen discharge with the help of the above mentioned diagnostics. Thus the IEDFs of the hydrogen positive ions and the relative composition of the ion flux striking the grounded electrode are determined. The H_3^+ IEDFs show peak splitting in energy, in agreement with the theory based on the finite transit time of ions through the sheath in comparison with the RF cycle. The H_2^+ IEDFs arriving at the grounded electrode are found to be a combination of H_2^+ ion flux from the bulk plasma and ions formed through collisions of background gas with the energetic H_3^+ and H_2^+ ions in the RF sheath. The H^+ ions present much lower energy peaks in comparison with the other species. The relative composition of positive hydrogen ions shows that the H_3^+ is the dominant ion species. The relative ion flux of H_3^+ reaching the grounded electrode decreases with power increase in favor of H_2^+ for all values of the pressure.

The above experimental findings are compared with the PIC simulated results. Using the PIC simulation code, the analysis is extended to the sheath edge of the plasma. A theoretical model is developed based on the separation of the peaks in the bimodal structure and the measured electron density at the sheath edge. In the assumption of a collisionless plasma the model can evaluate the electron temperature at the sheath edge. However, the model is limited by the discharge configuration and its macroscopic parameters (gas pressure, RF power). In addition, the model cannot be applied in the case of ions formed within the sheath, but applies only to those species formed in the bulk plasma.

In the second set of experiments the plasma source operates in pulsed mode. The ion energy analyzer results show H_3^+ ions persisting longer into the afterglow, with their energy sustained at approximately 3 eV. This phenomenon is explained in the hypothesis of super elastic collision, in which a vibrationally excited molecule, de-excited through collision with an electron, transfers the energy to the electron. Measuring the temporal evolution of the electron density in the center of the discharge, shows that immediately after the plasma is switched OFF, the electron density rises, with the rise being proportional to the applied voltage and the gas pressure. This result is unexpected and difficult to explain.

One of the indirect conclusions from this work is the validation of the hairpin probe as a plasma diagnostic technique. It has been proven to be valid for usage in plasmas where Langmuir probes can be troublesome, as in the proximity of magnetic fields or devices with large plasma potential oscillations. It is also shown that, once set, it requires no effort in measuring the electron density, quality desired for a plasma sensor, which can be incorporated into an industrial plasma tool. Having said this, the hairpin resonator as a plasma diagnostic technique is far from being completely understood. A more rigorous model regarding sheath formation around the hairpin prongs and the corresponding correction is required.

Appendix A

Hydrogen reactions chart

In this appendix is presented the hydrogen collision set used by the particle-in-cell simulation code. The cross-section values used by the simlation code are compiled from the comprehensive set recommended by Phelps [23, 72] and from T Simko [24].

1.	Effective momentum transfer for $E < 10V$ *Elastic*	$e + H_2 \rightarrow e + H_2$
2.	Rotational excitation $J = 0 \rightarrow 2$	$e + H_2 \rightarrow e + H_2^*(J = 2)$
3.	Rotational excitation $J = 1 \rightarrow 3$	$e + H_2 \rightarrow e + H_2^*(J = 3)$
4.	Vibrational excitation $v = 0 \rightarrow 1$	$e + H_2 \rightarrow e + H_2^*(v = 1)$
5.	Vibrational excitation $v = 0 \rightarrow 2$	$e + H_2 \rightarrow e + H_2^*(v = 2)$
6.	Sum of triplets: $a\,({}^3\Sigma_g{}^+)\,,b\,({}^3\Sigma_u{}^+)\,,c\,({}^3\Pi_u)$	$e + H_2 \rightarrow e + H_2^*$
7.	Sum of singlet $B\,({}^1\Sigma_u{}^+)\,,C\,({}^1\Pi_u)\,,D\,({}^3\Pi_u)$ and Rydberg states cross sections	$e + H_2 \rightarrow e + H_2^*$
8.	Dissociative excitation (sum of $n = 0 \rightarrow 2$ and $n = 0 \rightarrow 3$)	$e + H_2 \rightarrow e + H^* + H + e$

9.	Ionization	$e + H_2 \rightarrow e + H_2^+ + e$
10.	Rotational excitation for $J = 0 \rightarrow 2$ by H^+	$H^+ + H_2 \rightarrow H^+ + H_2^*(J = 2)$
11.	Rotational excitation for $J = 1 \rightarrow 3$ by H^+	$H^+ + H_2 \rightarrow H^+ + H_2^*(J = 3)$
12.	Rotational excitation for $J = 2 \rightarrow 4$ by H^+	$H^+ + H_2^*(J = 2) \rightarrow H^+ + H_2^*(J = 4)$
13.	Rotational excitation for $J = 3 \rightarrow 5$ by H^+	$H^+ + H_2^*(J = 3) \rightarrow H^+ + H_2^*(J = 5)$
14.	Vibrational excitation for $v = 0 \rightarrow 1$ by H^+	$H^+ + H_2 \rightarrow H^+ + H_2^*(v = 1)$
15.	Vibrational excitation $v = 0 \rightarrow 2$ by H^+	$H^+ + H_2 \rightarrow H^+ + H_2^*(v = 2)$
16.	Vibrational excitation $v = 0 \rightarrow 3$ by H^+	$H^+ + H_2 \rightarrow H^+ + H_2^*(v = 3)$
17.	H^+ charge exchange	$H^+ + H_2 \rightarrow H + H_2^+$
18.	Lyman alpha dissociation and excitation by H^+	$H^+ + H_2 \rightarrow H^+ + H^* + H$
19.	Balmer alpha dissociation and excitation by H^+	$H^+ + H_2 \rightarrow H^+ + H^* + H$
20.	H_2 ionization by H^+	$H^+ + H_2 \rightarrow H^+ + H_2^+ + e$
21.	H_2 dissociative ionization by H^+	$H^+ + H_2 \rightarrow H^+ + H^+ + H + e$
22.	H_2 charge exchange (*Elastic*)	$H_2^+ + H_2 \rightarrow H_2^+ + H_2$
23.	H_2^+ association	$H_2^+ + H_2 \rightarrow H_3^+ + H$
24.	Vibrational excitation by H_2^+	$H_2^+ + H_2 \rightarrow H_2^+ + H_2^*$
25.	Dissociation of H_2^+	$H_2^+ + H_2 \rightarrow H^+ + H + H_2$
26.	Lyman alpha dissociation and excitation by H_2^+	$H_2^+ + H_2 \rightarrow H_2^+ + H^* + H$
27.	Balmer alpha dissociation and excitation by H_2^+	$H_2^+ + H_2 \rightarrow H_2^+ + H^* + H$
28.	90% of ionization is assumed to produce H_2^+	$H_2^+ + H_2 \rightarrow H_2^+ + H_2^+ + e$
29.	10% of ionization is assumed to produce H_2^+	$H_2^+ + H_2 \rightarrow H_2^+ + H^+ + H + e$
30.	Momentum transfer (*Elastic*)	$H_3^+ + H_2 \rightarrow H_3^+ + H_2$
31.	Production of slow H_2^+	$H_3^+ + H_2 \rightarrow H_2^+ + H_3^+$
32.	Production of slow H^+	$H_3^+ + H_2 \rightarrow H^+ + H_2 + H_2$
33.	Production of fast H_2^+	$H_3^+ + H_2 \rightarrow H_2^+ + H_3$
34.	Production of fast H^+	$H_3^+ + H_2 \rightarrow H^+ + H_2 + H_2$
35.	Lyman alpha dissociation and excitation by H_3^+	$H_3^+ + H_2 \rightarrow H_3^+ + H^* + H$
36.	Balmer alpha dissociation and excitation by H_3^+	$H_3^+ + H_2 \rightarrow H_3^+ + H^* + H$

37.	Ionization by H_2^+	$H_3^+ + H_2 \rightarrow H_3^+ + H_2^+ + e$
38.	Ionization by H^+	$H_3^+ + H_2 \rightarrow H_3^+ + H^+ + H + e$
39.	H collision ($elastic$)	$H + H_2 \rightarrow H + H_2$
40.	Rotational excitation by H for $J = 0 \rightarrow 2$	$H + H_2 \rightarrow H + H_2^*(J = 2)$
41.	Rotational excitation by H for $J = 0 \rightarrow 3$	$H + H_2 \rightarrow H + H_2^*(J = 3)$
42.	Vibrational excitation by H for $v = 0 \rightarrow 1$	$H + H_2 \rightarrow H + H_2^*(v = 1)$
43.	Lyman alpha dissociation and excitation by H	$H + H_2 \rightarrow H + H^* + H$
44.	Balmer alpha dissociation and excitation by H	$H + H_2 \rightarrow H + H^* + H$
45.	Balmer beta dissociation and excitation by H	$H + H_2 \rightarrow H + H^* + H$
46.	Ionization by H	$H + H_2 \rightarrow H + H_2^+ + e$
47.	Dissociative ionization	$H + H_2 \rightarrow H + H^+ + H + e$
48.	Production of fast H^-	$H + H_2 \rightarrow H^- + H_2^+$
49.	H_2 Rotational excitation for $J_{1,2} = 0, 0 \rightarrow 0, 2$	$H_2 + H_2 \rightarrow H_2 + H_2^*(J = 2)$
50.	H_2 Rotational excitation for $J_{1,2} = 0, 0 \rightarrow 2, 2$	$H_2 + H_2 \rightarrow H_2^*(J = 2) + H_2^*(J = 2)$
51.	H_2 Rotational excitation for $J_{1,2} = 0, 0 \rightarrow 0, 4$	$H_2 + H_2 \rightarrow H_2 + H_2^*(J = 4)$
52.	H_2 Vibrational excitation for $v_{1,2} = 0, 0 \rightarrow 0, 1$	$H_2 + H_2 \rightarrow H_2 + H_2^*(v = 1)$
53.	Balmer alpha dissociation and excitation by H_2	$H_2 + H_2 \rightarrow H_2 + H^* + H$
54.	H_2 dissociation	$H_2 + H_2 \rightarrow H + H + H_2$
55.	H_2 ionization	$H_2 + H_2 \rightarrow H_2^+ + e + H_2$
56.	H_2 dissociative ionization	$H_2 + H_2 \rightarrow H^+ + H + e + H_2$
57.	H_2 dissociative ionization	$H_2 + H_2 \rightarrow H^+ + H^+ + e + e + H_2$
58.	H^- momentum transfer ($Elastic$)	$H^- + H_2 \rightarrow H^- + H_2$
59.	H^- detachment	$H^- + H_2 \rightarrow H + e + H_2$
60.	Ionization by H^-	$H^- + H_2 \rightarrow H_2^+ + e + H^-$
61.	Dissociative ionization by H^-	$H^- + H_2 \rightarrow H^+ + e + H + H^-$

Appendix B

Plasma permitivity

Considering a uniform infinite collisionless plasma in the presence of constant magnetic field $\vec{B} = B_0\hat{z}$, one can write the motion equation for a charged particle:

$$m \cdot \frac{d\vec{v}}{dt} = q \cdot \left(\vec{E} + \vec{v} \times \vec{B}\right) \tag{B.1}$$

and solving this using the small perturbation method, where:

$$\begin{cases} \vec{v} = \vec{v_0}e^{-i\omega t} \\ \vec{E} = \vec{E_0}e^{-i\omega t} \end{cases} \tag{B.2}$$

and considering only the first order solution, the equation B.1 in cartesian coordinates becomes:

$$\begin{cases} -im\omega v_x = qE_x + qB_0v_y \\ -im\omega v_y = qE_y - qB_0cv_x \\ -im\omega v_z = qE_z \end{cases} \tag{B.3}$$

noting the gyroscopic frequency $\omega_c = \frac{qB_0}{m}$ is obtained:

$$\begin{cases} (\omega + \omega_c)(v_x - iv_y) = \frac{iq}{m}(E_x - iE_y) \\ (\omega - \omega_c)(v_x + iv_y) = \frac{iq}{m}(E_x + iE_y) \\ v_z = \frac{iq}{m\omega}E_z \end{cases} \tag{B.4}$$

Expressing $\vec{v}$ and $\vec{E}$ in relation to the magnetic field orientation we have $\vec{v} = \vec{v_\perp} + \vec{v_\parallel}$, where $\vec{v_\perp} = v_x\hat{x} + v_y\hat{y}$ and $\vec{v_\parallel} = v_z\hat{z}$ and respectively $\vec{E} = \vec{E_\perp} + \vec{E_\parallel}$, with $\vec{E_\perp} = E_x\hat{x} + v_y\hat{y}$ and $\vec{E_\parallel} = E_z\hat{z}$. From the above definitions and knowing that

$v_\perp^2 = v_x^2 + v_y^2$ and $v^2 = v \cdot v^*$ it is obtained:

$$\begin{cases} v_{\perp_{1,2}} = \frac{1}{2}(v_x \mp v_y) \\ E_{\perp_{1,2}} = \frac{1}{2}(Ev_x \mp E_y) \\ v_\parallel = v_z, \; E_\parallel = E_z \end{cases} \tag{B.5}$$

introducing B.5 in B.4 becomes:

$$\begin{cases} v_{\perp_{1,2}} = \frac{iq}{m}\frac{E_{\perp_{1,2}}}{\omega \pm \omega_c} \\ v_\parallel = \frac{iq}{m}\frac{E_\parallel}{\omega} \end{cases} \tag{B.6}$$

The current density can be written as:

$$\vec{J} = nq\vec{v} = \frac{\partial \vec{P}}{\partial t} \tag{B.7}$$

where $\vec{P}$ is the polarization and can be expressed as

$$\vec{P} = \epsilon_o \chi \vec{E} \tag{B.8}$$

with χ the medium susceptibility. Solving B.8 using the small perturbation method it is obtained:

$$\frac{\partial \vec{P}}{\partial t} = \epsilon_o \chi \frac{\partial \vec{P}}{\partial t} = -i\omega\epsilon_o \chi \vec{E} \tag{B.9}$$

From B.6, B.7 and B.9 one can write:

$$\chi_{\perp_{1,2}} = \frac{nq^2}{\epsilon_0 m}\frac{1}{\omega(\omega \mp \omega_c)} = \frac{\omega_p^2}{\omega(\omega \mp \omega_c)} \tag{B.10}$$

and

$$\chi_\parallel = -\frac{nq^2}{\epsilon_0 m}\frac{1}{\omega^2} = -\frac{\omega_p^2}{\omega^2} \tag{B.11}$$

where it is noted $\omega_p = \frac{nq^2}{\epsilon_0 m}$ (as defined in 1.10). Translating back to the cartesian x, y, z coordinates one needs to solve the system:

$$-\frac{inq}{\epsilon_0 \omega}\begin{pmatrix} v_x \\ v_y \\ v_z \end{pmatrix} = \begin{pmatrix} \chi_{x,x} & \chi_{x,y} & \chi_{x,z} \\ \chi_{y,x} & \chi_{y,y} & \chi_{y,z} \\ \chi_{z,x} & \chi_{z,y} & \chi_{z,z} \end{pmatrix}\begin{pmatrix} E_x \\ E_y \\ E_z \end{pmatrix} \tag{B.12}$$

Equation B.12 can be solved in the assumption that $\omega \neq 0$ and $\omega \pm \omega_c \neq 0$. Hence the χ_{ij} components can be determined:

$$\chi_{x,z} = \chi_{y,z} = \chi_{z,x} = \chi_{z,y} = 0 \tag{B.13}$$

$$\chi_{x,y} = -\chi_{y,x} = \frac{i\left(\chi_{\perp_2} - \chi_{\perp_1}\right)}{2} = i\frac{\omega_p^2\omega_c}{\omega\left(\omega^2 - \omega_c^2\right)} \tag{B.14}$$

$$\chi_{x,x} = \chi_{y,y} = \frac{\chi_{\perp_2} + \chi_{\perp_1}}{2} = -\frac{\omega_p^2}{\left(\omega^2 - \omega_c^2\right)} \tag{B.15}$$

and

$$\chi_{z,z} = \chi_{\parallel} = -\frac{\omega_p^2}{\omega^2} \tag{B.16}$$

Knowing the relation:

$$\vec{D} = \boldsymbol{\epsilon} \cdot \vec{E} = \epsilon_0 (\mathbf{1} + \boldsymbol{\chi}) \cdot \vec{E} \tag{B.17}$$

one can determine the dielectric tensor $\boldsymbol{\epsilon}$:

$$\boldsymbol{\epsilon} = \epsilon_0 \begin{pmatrix} 1 - \frac{\omega_p^2}{(\omega^2 - \omega_c^2)} & 1 + i\frac{\omega_p^2\omega_c}{\omega(\omega^2 - \omega_c^2)} & 0 \\ 1 - i\frac{\omega_p^2\omega_c}{\omega(\omega^2 - \omega_c^2)} & 1 - \frac{\omega_p^2}{(\omega^2 - \omega_c^2)} & 0 \\ 0 & 0 & 1 - \frac{\omega_p^2}{\omega^2} \end{pmatrix} \tag{B.18}$$

Using the form of the dielectric tensor from B.18 it can be determined the influence of the magnetic field on the hairpin probe. It's easily to observe that if the magnetic field is zero the relation (B.18) becomes equivalent with (2.3).

Bibliography

[1] F. F. Chen and J. P. Chang, *Lecture notes on principles of plasma processing.* University of California, Los Angeles, 2002. 3, 10, 13, 30

[2] W. Holber and J. Forster, "Ion energetics in electron-cyclotron resonance discharges," *JOURNAL OF VACUUM SCIENCE & TECHNOLOGY A-VACUUM SURFACES AND FILMS*, vol. 8, pp. 3720–3725, SEP-OCT 1990. 4

[3] J. Coburn and E. Kay, "Positive-ion bombardment of substrates in rf diode glow-discharge sputtering," *JOURNAL OF APPLIED PHYSICS*, vol. 43, no. 12, pp. 4965–4971, 1972. 4

[4] K. Kohler, D. Horne, and J. Coburn, "Frequency-dependence of ion-bombardment of grounded surfaces in rf argon glow-discharges in a planar system," *JOURNAL OF APPLIED PHYSICS*, vol. 58, no. 9, pp. 3350–3355, 1985. 4

[5] A. Kuypers and H. Hopman, "Ion energy measurement at the powered electrode in an rf discharge," *JOURNAL OF APPLIED PHYSICS*, vol. 63, pp. 1894–1898, MAR 15 1988. 4

[6] U. Flender and K. Wiesemann, "Ion distribution-functions behind an rf sheath (vol 27, pg 509, 1992)," *JOURNAL OF PHYSICS D-APPLIED PHYSICS*, vol. 27, p. 1579, JUL 14 1994. 4

[7] C. Wild and P. Koidl, "Structured ion energy-distribution in radio-frequency glow-discharge systems," *APPLIED PHYSICS LETTERS*, vol. 54, pp. 505–507, FEB 6 1989. 4

[8] J. Olthoff, R. Vanbrunt, and S. Radovanov, “Ion kinetic-energy distributions in argon rf glow-discharges,” *JOURNAL OF APPLIED PHYSICS*, vol. 72, pp. 4566–4574, NOV 15 1992. 4

[9] J. K. Olthoff, J. V. Brunt, and R. J. A. e. a. S B Radovanov, “Kinetic-energy distributions of ions sampled from argon plasmas in a parallel-plate, radio-frequency reference cell,” *JOURNAL OF APPLIED PHYSICS*, vol. 75, p. 115, 1994. 4

[10] J. Olthoff, R. Vanbrunt, and S. Radovanov, “Studies of ion kinetic-energy distributions in the gaseous electronics conference rf reference cell,” *JOURNAL OF RESEARCH OF THE NATIONAL INSTITUTE OF STANDARDS AND TECHNOLOGY*, vol. 100, pp. 383–400, JUL-AUG 1995. 47th Annual Gaseous Electronics Conference of the American-Physical-Society, GAITHERSBURG, MD, OCT 18-21, 1994. 4

[11] P. Hargis, K. Greenberg, P. Miller, J. Gerardo, J. Torczynski, M. Riley, G. Hebner, J. Roberts, J. Olthoff, J. Whetstone, R. Vanbrunt, M. Sobolewski, H. Anderson, M. Splichal, J. Mock, P. Bletzinger, A. Garscadden, R. Gottscho, G. Selwyn, M. Dalvie, J. Heidenreich, J. Butterbaugh, M. Brake, M. Passow, J. Pender, A. Lujan, M. Elta, D. Graves, H. Sawin, M. Kushner, J. Verdeyen, R. Horwath, and T. Turner, “The gaseous electronics conference radiofrequency reference cell - a defined parallel-plate radiofrequency system for experimental and theoretical-studies of plasma-processing discharges,” *REVIEW OF SCIENTIFIC INSTRUMENTS*, vol. 65, pp. 140–154, JAN 1994. 4, 15

[12] F. Chen, “Industrial applications of low-temperature plasma physics,” *PHYSICS OF PLASMAS*, vol. 2, pp. 2164–2175, JUN 1995. 36th Annual Meeting of the Division-of-Plasma-Physics of the American-Physical-Society, MINNEAPOLIS, MN, NOV 07-11, 1994. 5

[13] M. Sugawara and B. Stansfield, *Plasma etching : fundamentals and applications.* Oxford University, 1998. 5

[14] V. A. Godyak, *Soviet radio frequency discharge research.* 1986. 8

[15] M. A. Lieberman and A. J. Lichtenberg, *Principles of plasma discharges and materials processing.* 2nd ed., 2005. 8, 9, 10, 13, 34, 46, 68, 70

[16] J. Lawrence and J. Varnerin, “Electron recombination and cross-section measurements in decaying hydrogen plasma,” *PHYSICAL REVIEW*, vol. 82, p. 568, 1951. 10

[17] D. Rose and S. Brown, “High-frequency gas discharge plasma in hydrogen,” *PHYSICAL REVIEW*, vol. 98, no. 2, pp. 310–316, 1955. 10

[18] J. Amorim, J. Loureiro, G. Baravian, and M. Touzeau, “Experimental and theoretical study of dissociation in the positive column of a hydrogen glow discharge,” *Journal Of Applied Physics*, vol. 82, pp. 2795–2804, Sep 15 1997. 10

[19] S. Longo, M. Capitelli, and K. Hassouni, “The coupling of pic/mcc models of discharge plasmas with vibrational and electronic kinetics,” *JOURNAL DE PHYSIQUE IV*, vol. 7, pp. 271–281, OCT 1997. XXIIIrd International Conference on Phenomena in Ionized Gases, TOULOUSE, FRANCE, JUL 17-22, 1997. 10

[20] T. Novikova, B. Kalache, P. Bulkin, K. Hassouni, W. Morscheidt, and P. Cabarrocas, “Numerical modeling of capacitively coupled hydrogen plasmas: Effects of frequency and pressure,” *JOURNAL OF APPLIED PHYSICS*, vol. 93, pp. 3198–3206, MAR 15 2003. 10

[21] S. Longo, K. Hassouni, D. Iasillo, and M. Capitelli, “Coupled electron and molecular vibrational kinetics in a 1d particle-in-cell model of a low pressure, high frequency electric discharge in nitrogen,” *JOURNAL DE PHYSIQUE III*, vol. 7, pp. 707–718, MAR 1997. 10

[22] A. Salabas, L. Marques, J. Jolly, G. Gousset, and L. Alves, “Systematic characterization of low-pressure capacitively coupled hydrogen discharges,” *JOURNAL OF APPLIED PHYSICS*, vol. 95, pp. 4605–4620, MAY 1 2004. 10

[23] A. Phelps, “Cross-sections and swarm soefficients for $H^+, H_2^+ +, H_3^+, H, H_2^-$ AND H^- IN H_2 for energies from 0.1 eV to 10 KEV,” *Journal Of Physical And Chemical Reference Data*, vol. 19, no. 3, pp. 653–675, 1990. 11, 12, 51, 91

[24] T. Simko, V. Martisovits, J. Bretagne, and G. Gousset, “Computer simulations of H^+ and H_3^+ transport parameters in hydrogen drift tubes,” *PHYSICAL REVIEW E*, vol. 56, pp. 5908–5919, NOV 1997. 11, 91

[25] S. Datz, G. Sundstroem, and et al, “Branching Processes in the Dissociative Recombination of H_3^+,” *Phys. Rev. Lett.*, vol. 74, no. 896-899, 1995. 11

[26] A. Schaeffer and S. Thompson, “The exchange of hydrogen and deuterium in the presence of electrons and ultraviolet radiation,” *RADIATION RESEARCH*, vol. 10, no. 6, pp. 671–679, 1959. 12

[27] M. Larsson, “Experimental studies of the dissociative recombination of H_3^+,” *PHILOSOPHICAL TRANSACTIONS OF THE ROYAL SOCIETY OF LONDON SERIES A-MATHEMATICAL PHYSICAL AND ENGINEERING SCIENCES*, vol. 358, pp. 2433–2443, SEP 15 2000. Discussion Meeting on Astronomy, Physics and Chemistry H_3^+, LONDON, ENGLAND, FEB 09-10, 2000. 12

[28] E. A. Bogdanov, C. A. DeJoseph, Jr., V. I. Demidov, and A. A. Kudryavtsev, “Effect of electron detachment on the wall potential and plasma evolution in the afterglow stage,” *APPLIED PHYSICS LETTERS*, vol. 89, JUL 10 2006. 12, 13

[29] V. Demidov, C. DeJoseph, Jr., and A. Kudryavtsev, “Nonlocal effects in a bounded afterglow plasma with fast electrons,” *IEEE TRANSACTIONS ON PLASMA SCIENCE*, vol. 34, pp. 825–833, JUN 2006. Workshop on Nonlocal, Collisionless Electron Transport in Plasmas, Princeton, NJ, 2005. 12

[30] V. Demidov, C. DeJoseph, and A. Kudryavtsev, “Anomalously high near-wall sheath potential drop in a plasma with nonlocal fast electrons,” *PHYSICAL REVIEW LETTERS*, vol. 95, NOV 18 2005. 12

[31] V. Demidov, C. DeJoseph, and A. Kudryavtsev, “Effect of metastable atoms on near-wall voltage drop in the afterglow of a noble-gas radio-frequency inductive coupled plasma,” *PHYSICS OF PLASMAS*, vol. 11, pp. 5350–5353, NOV 2004. 12, 13

[32] J. Berndt, E. Kovacevic, V. Selenin, I. Stefanovic, and J. Winter, “Anomalous behaviour of the electron density in a pulsed complex plasma,” *PLASMA SOURCES SCIENCE & TECHNOLOGY*, vol. 15, pp. 18–22, FEB 2006. 13

[33] R. J. Goldston and P. Rutherford, *Introduction to plasma physics.* Philadelphia, PA : Institute of Physics Pub, 1995. 13

[34] I. Hutchinson, *Principles of plasma diagnostics.* Cambridge University Press, 1987. 13

[35] H. Analytical, *Hiden EQP User manual and applciation notes.* 22

[36] A. Garscadden and K. Emeleus, “Notes on effect of noise on langmuir probe characteristics,” *PROCEEDINGS OF THE PHYSICAL SOCIETY OF LONDON*, vol. 79, no. 509, p. 535, 1962. 28

[37] R. Gagne and A. Cantin, “Investigation of an rf plasma with symmetrical and asymmetrical electrostatic probes,” *JOURNAL OF APPLIED PHYSICS*, vol. 43, no. 6, pp. 2639–&, 1972. 28

[38] B. Annaratone and N. Braithwaite, “A comparison of a passive (filtered) and an active (driven) probe for rf plasma diagnostics,” *Measurement Science & Technology*, vol. 2, pp. 795–800, Aug 1991. 28

[39] N. Braithwaite, N. Benjamin, and J. Allen, “An electrostatic-probe technique for rf plasma,” *JOURNAL OF PHYSICS E-SCIENTIFIC INSTRUMENTS*, vol. 20, pp. 1046–1049, AUG 1987. 28

[40] R. Stenzel, “Microwave resonator probe for localized density-measurements in weakly magnetized plasmas,” *REVIEW OF SCIENTIFIC INSTRUMENTS*, vol. 47, no. 5, pp. 603–607, 1976. 28, 29, 30

[41] R. Piejak, V. Godyak, R. Garner, B. Alexandrovich, and N. Sternberg, "The hairpin resonator: A plasma density measuring technique revisited," *JOURNAL OF APPLIED PHYSICS*, vol. 95, pp. 3785–3791, APR 1 2004. 28, 31, 35

[42] S. K. Karkari, C. Gaman, A. R. Ellingboe, I. Swindells, and J. W. Bradley, "A floating hairpin resonance probe technique for measuring time-resolved electron density in pulse discharge," *MEASUREMENT SCIENCE & TECHNOLOGY*, vol. 18, pp. 2649–2656, AUG 2007. 28, 31, 32

[43] S. K. Karkari, A. R. Ellingboe, C. Gaman, I. Swindells, and J. W. Bradley, "Electron density modulation in an asymmetric bipolar pulsed dc magnetron discharge," *JOURNAL OF APPLIED PHYSICS*, vol. 102, SEP 15 2007. 28, 31, 34, 71

[44] R. Piejak, J. Al-Kuzee, and N. Braithwaite, "Hairpin resonator probe measurements in rf plasmas," *Plasma Sources Science & Technology*, vol. 14, pp. 734–743, NOV 2005. 31

[45] J. W. Bradley and T. Welzel, "Physics and phenomena in pulsed magnetrons: an overview," *JOURNAL OF PHYSICS D-APPLIED PHYSICS*, vol. 42, MAY 7 2009. 34

[46] J. Bradley, S. Karkari, and A. Vetushka, "A study of the transient plasma potential in a pulsed bi-polar dc magnetron discharge," *PLASMA SOURCES SCIENCE & TECHNOLOGY*, vol. 13, pp. 189–198, MAY 2004. 34

[47] P. Starke, S. Christ-Koch, S. Karkari, C. Gaman, U. Fantz, and A. Ellingboe, "Performance of a langmuir probe and a hairpin resonance probe in inductively coupled low pressure plasmas," in *XXVIII International Conference on Phenomena in Ionized Gases*, (Prague, Czech Republic), 2007. 36

[48] P. Scheubert, U. Fantz, P. Awakowicz, and H. Paulin, "Experimental and theoretical characterization of an inductively coupled plasma source," *JOURNAL OF APPLIED PHYSICS*, vol. 90, pp. 587–598, JUL 15 2001. 36

[49] V. Vahedi, G. DiPeso, C. K. Birdsali, M. A. Lieberman, and T. D. RognlienS, “Capacitive rf discharges modelled by particle-in-cell monte carlo simulation. i: analysis of numerical techniques,” *Plasma Sources Sci. Technol*, vol. 4, pp. 261–272, 1993. 40

[50] V. Vahedi, C. K. Birdsall, M. A. Lieberman, G. DiPeso, and T. D. Rognlien, “Capacitive rf discharges modelled by particle-in-cell monte carlo simulation. ii: comparisons with laboratory measurements of electron i energy dktribution functions,” *Plasma Sources Sci. Technol*, vol. 4, pp. 273–278, 1993. 40

[51] M. Turner, “Pressure heating of electrons in capacitively coupled rf discharges,” *PHYSICAL REVIEW LETTERS*, vol. 75, pp. 1312–1315, AUG 14 1995. 40

[52] C. Birdsall, “Particle-in-cell charged-particle simulations, plus monte-carlo collisions with neutral atoms, pic-mcc,” *IEEE TRANSACTIONS ON PLASMA SCIENCE*, vol. 19, pp. 65–85, APR 1991. 40

[53] C. K. Birdsall, A. Langdon, B. Verboncoeur, and V. Vehedi, *Plasma physics via computer simulation.* Bristol, Eng : Adam Hilger, 1991. 40

[54] E. Kawamura, V. Vahedi, M. Lieberman, and C. Birdsall, “Ion energy distributions in rf sheaths; review, analysis and simulation,” *PLASMA SOURCES SCIENCE & TECHNOLOGY*, vol. 8, pp. R45–R64, AUG 1999. 45, 47

[55] L. Tonks and I. Langmuir, “A general theory of the plasma of an arc,” *Phys. Rev.*, vol. 34, pp. 876–922, Sep 1929. 70

[56] N. Sternberg and V. Godyak, “On asymptotic matching and the sheath edge,” *IEEE TRANSACTIONS ON PLASMA SCIENCE*, vol. 31, pp. 665–677, AUG 2003. 70

[57] K. Riemann, “Comments on “on asymptotic matching and the sheath edge”,” *IEEE TRANSACTIONS ON PLASMA SCIENCE*, vol. 32, pp. 2265–2270, DEC 2004. 70

[58] N. Sternberg and V. Godyak, “Comments on “on asymptotic matching and the sheath edge” - reply,” *IEEE TRANSACTIONS ON PLASMA SCIENCE*, vol. 32, pp. 2271–2276, DEC 2004. 70

[59] R. Franklin, “Where is the ‘sheath edge’?,” *JOURNAL OF PHYSICS D-APPLIED PHYSICS*, vol. 37, pp. 1342–1345, MAY 7 2004. 70

[60] S. Samukawa, H. Ohtake, and T. Mieno, “Pulse-time-modulated electron cyclotron resonance plasma discharge for highly selective, highly anisotropic, and charge-free etching,” *JOURNAL OF VACUUM SCIENCE & TECHNOLOGY A-VACUUM SURFACES AND FILMS*, vol. 14, pp. 3049–3058, NOV-DEC 1996. 71

[61] A. Anders, *Handbook of Plasma Immersion Ion Implantation and Deposition.* Wiley-Interscience, 2000. 71

[62] C. Rinsch, X. Chen, V. Panchalingam, R. Eberhart, J. Wang, and R. Timmons, “Pulsed radio frequency plasma polymerization of allyl alcohol: Controlled deposition of surface hydroxyl groups,” *LANGMUIR*, vol. 12, pp. 2995–3002, JUN 12 1996. 71

[63] P. Kelly, O. AbuZeid, R. Arnell, and J. Tong, “The deposition of aluminium oxide coatings by reactive unbalanced magnetron sputtering,” *SURFACE & COATINGS TECHNOLOGY*, vol. 86, pp. 28–32, DEC 1 1996. 23rd International Conference on Metallurgical Coatings and Thin Films, SAN DIEGO, CA, APR 22-26, 1996. 71

[64] R. Stark, J. Christiansen, K. Frank, F. Mucke, and M. Stetter, “Pseudospark produced pulsed electron-beam for material processing,” *IEEE TRANSACTIONS ON PLASMA SCIENCE*, vol. 23, pp. 258–264, JUN 1995. 71

[65] M. Osiac, T. Schwarz-Selinger, D. O’Connell, B. Heil, Z. L. Petrovic, M. M. Turner, T. Gans, and U. Czarnetzki, “Plasma boundary sheath in the afterglow of a pulsed inductively coupled rf plasma,” *PLASMA SOURCES SCIENCE & TECHNOLOGY*, vol. 16, pp. 355–363, MAY 2007. 74

[66] F. A. Herrero and J. P. Doering, “Superelastic Collisions of Vibrationally Excited H_2^+ with Atoms and Molecules,” *Phys. Rev. Lett.*, vol. 29, pp. 609–611, Sep 1972. 75

[67] W. vanderZande, J. Semaniak, V. Zengin, G. Sundstrom, S. Rosen, C. Stromholm, S. Datz, H. Danared, and M. Larsson, “Dissociative recombination of H_2^+: Product state information and very large cross sections of vibrationally excited H_2^+,” *PHYSICAL REVIEW A*, vol. 54, pp. 5010–5018, DEC 1996. 75

[68] D. H. Czarnetzki U, Luggenholscher D, “Space and time resolved electric field measurements in helium and hydrogen rf-discharges,” *PLASMA SOURCES SCIENCE & TECHNOLOGY*, vol. 8, pp. 230–248, 1999. 83

[69] T. Gans, C. Lin, V. S. von der Gathen, and D. Fobele, “Phase-resolved emission spectroscopy of a hydrogen rf discharge for the determination of quenching coefficients,” *PHYSICAL REVIEW A*, vol. 67, p. 012707, 2003. 83

[70] R. Freiberg and L. Weaver, “Microwave investigation of transition from ambipolar to free diffusion in afterglow plasmas,” *PHYSICAL REVIEW*, vol. 170, no. 1, pp. 336–&, 1968. 85

[71] N. S. Siefert, B. N. Ganguly, B. L. Sands, and G. A. Hebner, “Decay of the electron number density in the nitrogen afterglow using a hairpin resonator probe,” *JOURNAL OF APPLIED PHYSICS*, vol. 100, AUG 15 2006. 86

[72] S. Buckman and A. Phelps, “Jila information center report no. 27 avalable at http://jilawww.colorado.edu/ avp/,” 1985. 91